Final Technical Report

High Temperature, Low NOx Combustor Concept Development

Submitted: 12/29/19

WORK PERFORMED UNDER AGREEMENT

DE-FE0025344
Project Period: 10/01/15 – 09/30/19

SUBMITTED BY

Georgia Tech Research Corporation
505 Tenth St. NW
Atlanta, GA – 30332-0420
DUNs #: 09-739-4084

PRINCIPAL INVESTIGATOR

Principal Investigator: Timothy C. Lieuwen
P: 404.894.3041
F: 404.894.2760
tim.lieuwen@aerospace.gatech.edu

SUBMITTED TO

U. S. Department of Energy
National Energy Technology Laboratory

Mark Freeman
Mark.Freeman@netl.doe.gov

ABSTRACT

This technical report describes the investigation of key research questions associated with axially staged combustion, a concept for reducing undesirable NOx emissions at high flame temperatures (>1900K). Enabling gas turbine operation at such high temperatures is essential in achieving further progress in combined cycle thermal efficiency, and NOx emissions remains a key obstacle. The investigation presented in this report utilized three avenues of investigation in tandem. The first investigative tool is a chemical reactor network model in a design optimization framework. This tool was used to assess the minimum theoretical NOx emissions achievable by axial staged configurations. In addition, the reactor network was used to assess the sensitivity of the NOx floor to real world parameters such as finite entrainment and mixing rates. The sensitivity analysis indicates that rapid entrainment of crossflow into the secondary combustion zone has the highest impact on NOx reduction in the axial staged configuration. The second avenue of investigation was the experimental characterization of NOx emissions from a reacting jet in a vitiation crossflow (RJICF). The RJICF is a natural choice for the implementation of axial staging and more detailed understanding of its emissions behavior is critical to its implementation. Jets spanning a wide range of parameters were tested and great efforts were made to isolate the coupled effects of parameters such as bulk averaged temperature rise as a result of the RJICF (ΔT), jet stoichiometry (ϕ_{jet}), and momentum flux ratio (J). The experimental results confirm that NOx emissions increase monotonically with ΔT, but also indicate that lifting of the flame significantly impacts NOx production. The third research methodology is large eddy

simulation (LES) of reacting jets of various parameters. The results of the LES strongly support the importance of crossflow entrainment and flame lifting that was observed in the reactor modeling and experimental investigations.

TABLE OF CONTENTS

LIST OF TABLES

LIST OF FIGURES

LIST OF SYMBOLS AND ABBREVIATIONS

A	Empirical constant for jet trajectory
A_i	Area of investigation
A_{rea}	Area
AFS	Axially fuel staged
AMR	Adaptive mesh refinement
B	Empirical constant for jet trajectory
C	Local scalar concentration
$\bar{C}$	Spatial average of scalar concentration
C_m	Centerline scalar concentration
C_o	Reference scalar concentration (from jet potential core)
CCL	Computational Combustion Laboratory
CRN	Chemical Reactor Network
CVP	Counter-rotating vortex pair
Da_{ign}	Damkohler number based on ignition delay
d_j	Jet diameter
d_p	Particle diameter
DLN	Dry Low NOx
f	Mixture fraction
FSA	Frequency size analyzer
h	Channel height
J	Jet momentum flux ratio
JICF	Jet in crossflow

Ka_{mix}	Karlovitz number based on flow mixture
L	Simulation domain length
L_p	Length of pipe included in simulation domain
LDV	Laser Doppler velocimetry
LES	Large eddy simulation
LESLIE	Large eddy simulation code with linear eddy model
LHV	Lower heating value
$LHV_{C_2H_6}$	Lower heating value of ethane
LHV_{CH_4}	Lower heating value of methane
LO	Lift-off distance
LO_H	Lift-off height
LPM	Lean Pre-Mixed
ℓ_{core}	Mixing length scale associated with scalar jet potential core
ℓ_{decay}	Mixing length scale associated with scalar centerline decay post jet core
ℓ_{ent}	Entrainment length scale
$\ell_{ent,main}$	Main zone entrainment length scale
$\ell_{ent,sec}$	Secondary zone entrainment length scale
ℓ_m	Mixing length scale
$\dot{m}$	Mass flowrate
$\dot{m}_{C_2H_6}$	Mass flowrate of ethane in jet
$\dot{m}_{CH_4}$	Mass flowrate of methane in jet
$\dot{m}_{ef}$	Effective mass flowrate of fuel in jet
M_i	Mass of CRN region
m_j	Mass of jet fluid

m_{tot}	Total mass
$\overline{MW}$	Molecular weight of local mixture
MW_j	Molecular weight of jet fluid
MW_{XF}	Molecular weight of crossflow
N_j	Number of moles of jet fluid
N_{tot}	Total number of moles
NOx	Nitrogen oxides
p	Empirical constant for centerline scalar decay
PIV	Particle image velocimetry
PLIF	Planar laser induced fluorescence
PDM	Photodetector module
Re	Reynolds number
Re_p	Particle Reynolds number
RJICF	Reacting jet in crossflow
r	Spatial coordinate
r_τ	Ratio of CRN model entrainment times
s_c	Distance along scalar concentration centerline
SLV	Shear layer vortices
Stk	Stokes number
$\mathrm{Stk_j}$	Small scale Stokes number
Stk_∞	Large scale Stokes number
T	Temperature
T_i	Temperature of CRN region
T_{Flame}	Flame temperature
T_j	Jet fluid temperature

T_{XF} Crossflow temperature

t Time

t_0 Initial time

t_{inj} Injection time

t_j Small jet flow time scale

t_p Particle response time

t_∞ Large jet flow time scale

U Unmixedness

u_j Bulk jet velocity

u_p Velocity of flow relative to seed particle

u_∞ Bulk crossflow velocity

w Channel width

x Streamwise coordinate jet trajectory

z Height coordinate of jet trajectory

ΔNOx Rise in flow NOx concentration due to jet injection

ΔT Rise in bulk flow temperature due to jet injection

$\Delta\phi$ Rise in equivalence ratio due to jet injection

Θ Normalized illuminated area

λ Wavelength of incident light

μ_g Dynamic viscosity of gas

ν_g Kinematic viscosity of gas

ρ_j Jet density

ρ_p Particle density

ρ_∞ Crossflow density

$\tau_{ent,i}$ Entrainment time of CRN region

τ_{res}	Residence time
τ_{global}	Global residence time
τ_{main}	Main burner residence time
$\tau_{pre\text{-}flame}$	Time scale for pre-flame mixing duration
τ_{sec}	Secondary stage residence time
ϕ	Equivalence ratio
ϕ_{ent}	Entrainment region equivalence ratio
ϕ_{Flame}	Equivalence ratio of combustion
ϕ_{Global}	System equivalence ratio
ϕ_{jet}	Jet equivalence ratio
ϕ_{main}	Main burner equivalence ratio
ϕ_{sec}	Secondary injection equivalence ratio
ϕ_{XF}	Crossflow equivalence ratio
χ_i	Composition of CRN region
$[N_2]$	Nitrogen concentration
[NO]	Nitric oxide concentration
[O]	Atomic oxygen concentration
$[O_2]$	Oxygen concentraion

EXECUTIVE SUMMARY

This work described in this report is motivated by interest in axial staging of combustion as a means of reducing NOx emissions from gas turbine combustors operating at high flame temperatures (>1900K). At these temperatures, thermal NOx production rates are high, and conventional lean-premixed combustor architectures are unable to simultaneously deliver low NOx and part-load operability. In an axially staged combustor, the majority of the fuel is burned in a conventional lean-premixed flame, but additional fuel is injected from the combustor walls into the vitiated flow further downstream. A fuller understanding of the governing processes and parameters regarding pollutant formation within such a combustor architecture as well as any associated flow fields is critical to the next generation of gas turbine technology advancement.

The work described herein involves three parallel but complimentary avenues of investigation. The first is the use of a chemical reactor network model to establish a fundamental minimum to NOx production in an axially staged combustor. The model is also used to assess the sensitivity of this minimum to real world physical limitations such as finite entrainment rates. The second avenue of research is the experimental investigation of nitrogen oxide (NOx) emissions from a reacting jet in a vitiated crossflow (RJICF). A RJICF is a natural implementation of axially staged combustion and therefore the characterization of this flow field is central to evaluating the efficacy of stage combustion. The final investigatory technique is the simulation of a RJICF flow field using Large Eddy Simulation (LES) numerical methods. The LES tools are leveraged to provide detailed local and instantaneous information on heat release and NO formation withing the RJICF.

The combined efforts of this project produced a number of key findings that will be summarized here. The first of these findings is that the fundamental minimum for NOx emission in an staged combustor operating at a pressure of 25atm, an exit temperature of 1975K, and a 20ms residence time is on the order of 1ppm. This finding demonstrates the significant potential that stage combustion has to enable future gas turbine combustor technologies. In order to achieve levels near this theoretical minimum it was determined that substantial entrainment of the primary combustion products into the secondary combustion zone is essential for NOx reduction. The entrainment of the main flow prior to combustion controls the stoichiometry of the secondary combustion zone which in turn controls the temperature of the combustion products, and thereby the rate of thermal NO production. Entrainment of main flow post combustion controls the time interval that elevated temperatures from secondary combustion exist, potentially reducing the time available for elevated NOx production.

It is apparent that the findings indicate that utilization of a single pure fuel reacting jet does meet the necessary conditions to generate NOx reduction. However, the findings from this work indicate that NOx produced from a reacting jet can vary greatly even when delivering constant temperature rise to the main flow. NOx production withing a RJICF is primarily controlled by the initial composition of the jet (equivalence ratio) and the lift-off of the flame from the jet exit. Flame lifting enables the previously described main flow entrainment to occur. The physics that control flame-lift off are complex and multi-factorial but it is clear that flame liftoff is strongly connected to vortical structure withing the jet such as the shear layers and counter rotating vortex pair.

The presented work reveals pathways to ensuring minimal NOx production in a high temperature gas combustor. Within the framework of a reacting jet the key is to promote flame liftoff and enhance shear layer vortex growth rates. Flame liftoff is a complex multi-faceted problem whose governing physics are not directly addressed in this work. Similarly, the controlling sensitivities of the post-flame mixing efficacy, via strength and structure of the CVP, are most likely diverse in nature and are not addressed herein. Both of these areas require further work to deepen understanding of the relevant phenomena.

CHAPTER 1. BACKGROUND AND MOTIVATION

The generation of electricity from the consumption of natural gas is a major world energy source, accounting for 35% of electricity in the US for 2018 [1]. The plurality of natural gas as an energy source is projected to continue to grow as it supplants petroleum and coal due to environmental and economic concerns. The vast majority of the energy produced by natural gas fired systems is from gas turbines, either as standalone combustion turbines or in tandem with a steam turbines as part of combined-cycle power plants. Due to the critical position they possess in the world energy market, it is critical to continue to stimulate the development of these systems in order to increase their efficiency and mitigate their environmental impact.

Over the past several decades, the gas turbine industry has experienced significant increases in combined cycle efficiency, while simultaneous reducing undesirable emissions such as nitrogen oxides (NOx). Improvements in turbine materials and cooling methods have enabled ever higher turbine inlet temperatures. Higher turbine inlet temperatures lead to higher work/thrust in simple cycle systems and higher thermal efficiencies in combined cycle systems. In parallel, advances in fuel injector and post-flame mixing technologies have reduced NOx emissions through the elimination of locally high-temperature regions of the lean, premixed combustion. These advances have led to the current state of the art in gas turbine Dry Low NOx (DLN) combustor architectures [2]. In order to achieve further improvements in combined cycle efficiency, however, higher turbine inlet temperatures

are required. Figure 1 plots the flame temperature and NO emissions of several historical classes of gas turbines as well as several regulatory standards with regards to NOx emissions. Figure 1 clearly indicates that DLN combustors will be unable to meet current emission regulations while simultaneously delivering the necessary elevated combustor exit temperatures required for further increases in cycle efficiency due to the nature of NO production.

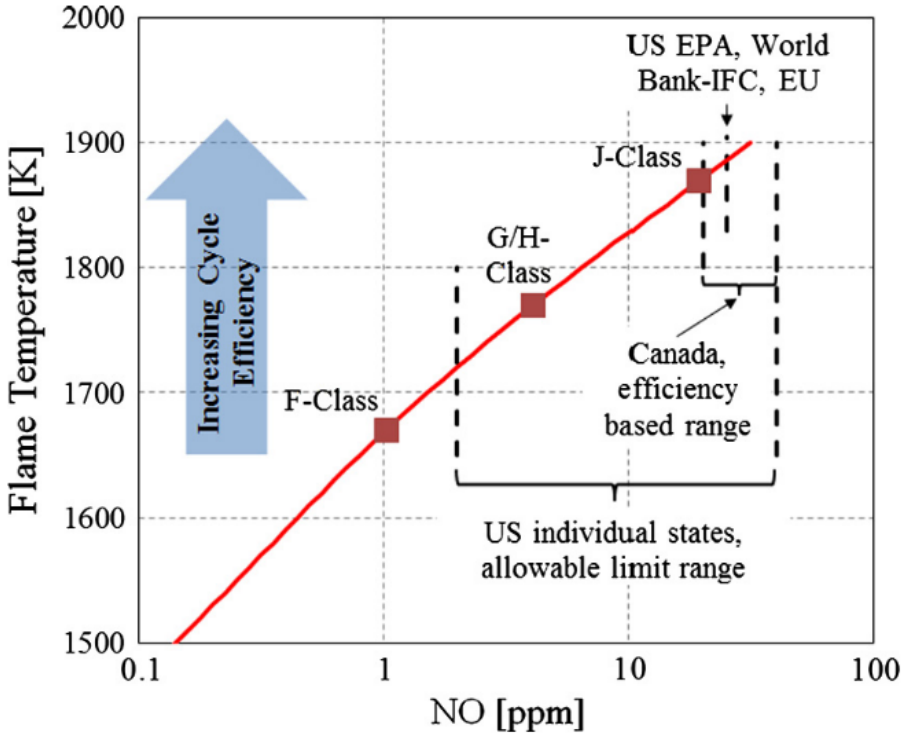

Figure 1 – Plot of flame temperature and emissions of current gas turbine technologies as well as standard emissions regulations reproduced from Klein [3].

1.1 Nitrogen Oxide Production in Gas Turbines

The historical approach of reducing NOx emissions from gas turbines by focusing on rapid fuel/air mixing works best in cases where the perfectly mixed flame temperature of the combustor is below the threshold where NOx production rates become significant. A general rule of thumb in the gas turbine industry is to restrict flame temperatures to below 1800K (already exceeded in state-of-the-art gas turbines). This is due to the kinetic sensitivities of the major pathways from NOx formation in a DLN gas turbine combustor.

NOx is produced by a number of mechanisms both within the flame (referred to as prompt NO) as well as post-flame [4]. At flame conditions proposed for future gas turbines (lean, temperature > 1975 K), thermal NO formation is the dominant source of NOx [5]. In premixed laminar flames at similar conditions, thermal NO is shown to become the majority source for NOx with as little as 5 ms of residence time (τ_{res}) [2, 6]. Thermal NO formation occurs via the Zeldovich NO mechanism in post-flame regions of the combustor. The Zeldovich mechanism is relatively simple, contained in its entirety by Equations 1 – 3, and well understood, with the rate constants well characterized over a wide range of conditions [7].

$$O + N_2 = NO + N \quad (1)$$

$$N + O_2 = NO + O \quad (2)$$

$$N + OH = NO + H \quad (3)$$

The rate of NO production from the Zeldovich mechanism is linear with both τ_{res} and atomic oxygen concentration, [O], as well as an exponential function of temperature (T) as indicated by Equation 4 derived from Bowman [6] and illustrated by Figure 2. Figure 2 plots calculated NO levels as a function τ_{res} at gas turbine conditions and various flame temperatures. Visible in Figure 2 is the prompt contribution to NO as well as the thermal contribution. At flame temperature as low as 1900K, prompt NO is shown to be rapidly exceeded by thermal NO; reinforcing the dominance of thermal NO at relevant conditions.

$$[NO] \propto [O][N_2]e^{-38{,}379/T}\tau_{res} \tag{4}$$

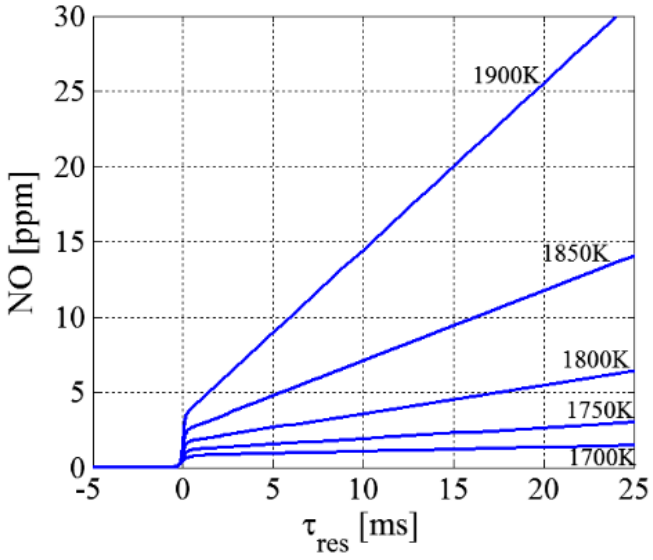

Figure 2 – NO as a function of residence time at different flame temperatures. Based on laminar flame calculations at gas turbine conditions reproduced from Lieuwen *et al* [2].

These sensitives of thermal NO formation have significant consequences on potential approaches for gas turbine combustor emissions mitigation. The linear dependence on τ_{res} immediately suggests that combustors designed with reduced τ_{res} would be successful in reducing NOx. There is, however, a limit to the extent this strategy can be used. It is limited, in practice, by operability needs with regards to turndown. Gas turbine combustors, in the field, need to operate over a range of loads each of which is associated with a different flame temperature. Lower loads, with lower flame temperatures, require longer residence times to enable complete conversion of super-equilibrium CO into CO_2. The dependency of CO on τ_{res} and flame temperature is highlighted in Figure 3, which plots calculated CO levels as a function τ_{res} at gas turbine conditions and various flame temperatures. Therefore, τ_{res}, is generally set by the requirement to achieve low CO emissions at some specified load point. As such, and alternate method to NOx reduction that preserves part load operability is needed.

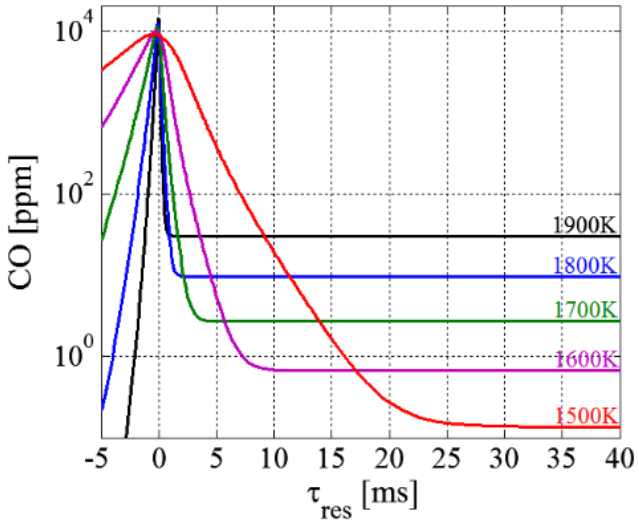

Figure 3 – CO as a function of residence time at different flame temperatures. Based on laminar flame calculations at gas turbine conditions reproduced from Lieuwen *et al* [2].

1.2 Axial Staging

Axial staging has been proposed as a NOx mitigation approach that can address the highlighted thermal NO sensitivities while also allowing for successful operation of the gas turbine at part load [8-10]. Axial staging is accomplished by combusting the majority of the fuel in a manner similar to traditional DLN architectures, i.e. lean and premixed. Subsequent to the primary combustion zone, the remainder of the fuel is injected into the flow in the vicinity of the combustor exit. This downstream injection creates a secondary region of combustion that raises the combustor temperature to its final value. The primary advantage of this approach is that it drastically reduces τ_{res} for the final, high-temperature, portion of the flow, and thereby minimizes the time available for elevated NO production rates. In addition, axial staging also address the [O] dependence of NO formation by placing the secondary combustion region in a reduced oxygen environment, in the form of the high-temperature combustion products of the primary combustion zone. Combustion in such an environment has been demonstrated to significantly reduce NO production [11]. Finally, axial staging also enables load turndown without negative impact on CO emissions as the combustor can simply be operated without the secondary injection when required.

Due to this potential, axial staging concepts have become a focus of research [12, 13]. This collective work supports the potential benefit of axial staging, but has also

stressed how critical the rapid and thorough mixing of the primary combustion products and the secondary fuel injection prior to ignition is to the realization of the NOx benefit. If mixing rates are not sufficiently high, an axially staged combustor could emit significantly higher NOx levels than predicted, and in the worst cases, at levels higher than those of DLN architectures.

1.3 Reacting Jet in Crossflow

A reacting jet in a vitiated crossflow (RJICF) presents a natural means by which to implement axial staging as its utilization does not require the insertion of hardware into the high-temperature crossflow. RJICFs are present in other applications such as in Rich-Quench-Lean combustors [14] and various fuel injection systems. The numerous industrial applications paired with the complex coupling of interesting physics have made the RJICF and the non-reacting jet in crossflow (JICF) topics of extensive research.

As mentioned in Section 1.2, the mixing between the crossflow and the axially staged fuel is crucial to achieving reductions in NOx emissions. Within the context of a RJICF, the relevant mixing can be divided into two regions: pre-flame and post-flame mixing. Pre-flame mixing refers to the mixing of the secondary jet and the crossflow prior to combustion. Since the composition of the jet and crossflow are not equal, pre-flame mixing controls whether reaction occurs in a premixed or non-premixed mode; in the former case, it also determines the stoichiometry of burning. Post-flame mixing refers to mixing of the secondary combustion products with the vitiated crossflow generated by the primary flame.

Post-flame mixing determines the time history of the temperature of the final combustion products, controlling the extent to which elevated flow temperatures, in comparison to the combustor exit temperature, persist.

The reacting flowfield that dictates the mixing behavior of these regions is complex and incorporates flame propagation of inhomogeneous mixtures in highly strained flows, edge flame propagation, flame auto-ignition, and hydrodynamic stability effects. As a pathway to understanding the NOx production of such a complex reacting flow it is necessary to understand the mechanics of flame stabilization as well as the underlying behavior of the non-reacting flowfield. To set this context, the following sections of this chapter discuss RJICF dynamics in more detail.

1.3.1 Non-reacting Jet in Crossflow Behaviour

Due to numerous industrial applications and its importance as a canonical fluid mechanics problem, the JICF has been the subject of extensive research [15]. As a result, the fundamental form of time averaged velocity and scalar fields for subsonic, non-reacting, momentum driven JICF is well established [15], and has been shown to be primarily governed by the jet-to-crossflow momentum flux ratio given by:

$$J = \frac{\rho_j u_j^2}{\rho_\infty u_\infty^2} \tag{5}$$

with ρ and u denoting the density and velocity of the jet and crossflow with subscripts j and ∞ respectively. A common resultant jet trajectory correlation is given by:

$$\frac{z}{d_j\sqrt{J}} = A\left(\frac{x}{d_j\sqrt{J}}\right)^B \tag{6}$$

with x and z corresponding to the trajectory location in the direction of the crossflow and transverse to it, respectively. The jet diameter is denoted by d_j and the coefficients A and B are parameters that account for various effects, such as boundary layer thickness, jet exit velocity profile, and jet trajectory definition (i.e., maximum velocity, scalar concentration, or other important fluid-mechanic features).

The mixing of the jet fluid with the surrounding crossflow is determined by the dynamics of a complex topology of vortical structures [16]. The dominant coherent vortical structures are the horseshoe vortex system, the wake vortices, the shear layer vortices (both leading-edge and lee-side), and the counter-rotating vortex pair. The topology of a JICF with these coherent vortical structures indicated is shown by Figure 4.

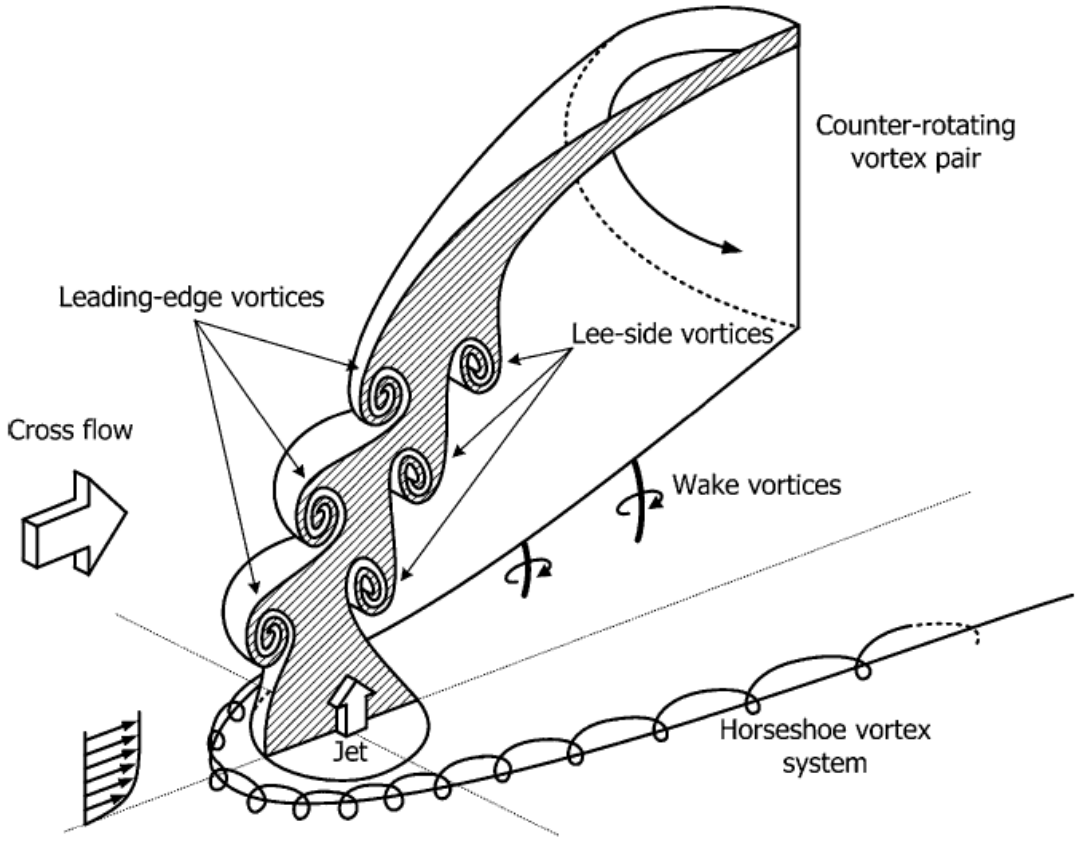

Figure 4 – Schematic of flow structure of a jet in crossflow reproduced from New *et al* [17].

The two coherent structures of particular interest to the pre-flame and post-flame mixing of a RJICF are the shear layer vortices (SLVs) and the counter rotating vortex pair (CVP). The SLVs are generated by the unstable shear layer of the exiting jet. The instability is via the Kelvin-Helmholtz mechanism, and creates rolled up regions of concentrated vorticity. The growth rate and size of these structures have an important influence on near-field mixing of the jet fluid and the crossflow. In addition, the SLVs are distorted by interaction with the crossflow and each other. This distortion of the SLVs results, on a time

averaged basis, in the CVP as described by Kelso *et al* [8] and illustrated in Figure 5. The CVP itself is a critical aspect of JICF topology as it is responsible for the far-field mixing behavior.

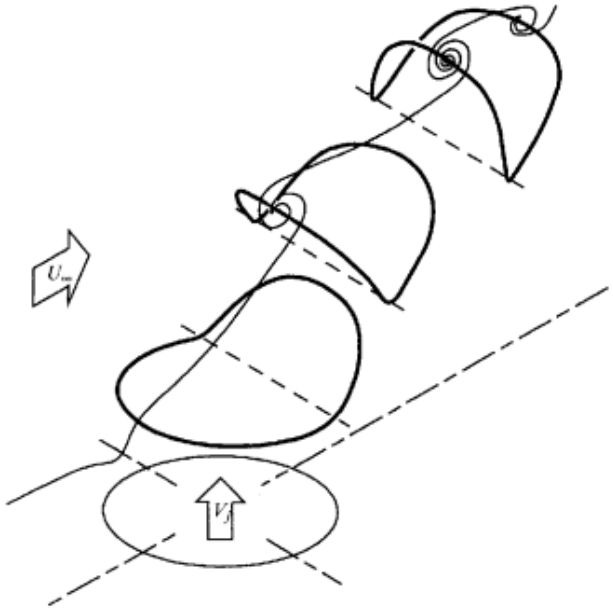

Figure 5 – Illustration of jet in crossflow shear layer vortex rings being distorted as they advect downstream reproduced from Kelso *et al* [8].

Extensive research has been aimed at characterizing JICF mixing, and it has been observed to be divided into near-field and far-field behavior, with the transition between the two being termed the 'branch' point. Smith & Mungal [18] observed the near-field behavior to be more 'jet-like,' with centerline maximum mean concentration (C_m/C_o) decay scaling as shown in Equation 7:

$$\frac{C_m}{C_o} \propto s_c^{-p} \tag{7}$$

with s_c corresponding to distance along the jet centerline trajectory, and p ranging from values of 1 to above 1.3 dependent on J and exit velocity profile [18-20]. The far-field was observed to be more 'wake-like' with C_m/C_o again scaling as in Equation 7 but with p values between 1 and ⅔ [18, 19].

Another useful parameter for characterizing the mixing behavior of JICF is the unmixedness (U), defined by Equation 8:

$$U = \frac{1}{A_i} \iint_{A_i} \frac{(C/C_o - \bar{C}/C_o)^2}{(\bar{C}/C_o)(1 - \bar{C}/C_o)} dA_{rea} \tag{8}$$

with A_i corresponding to the area of investigation, and C/C_o and $\bar{C}/C_o$ to the normalized local value and spatial average of jet fluid concentration respectively. Unmixedness can be applied to both cross-sectional and center-plane data to assess the degree of mixing of the JICF at a point along its trajectory, and Karagozian *et al* [19] observed both applications to follow similar trends. In addition, it was observed that cross-sectional and center-plane unmixedness follow similar trends to centerline maximum concentration decay. Both Smith & Mungal [18] and Karagozian *et al* [19] notice that, in certain instances, much more rapid decay of jet fluid concentration compared to other jets can be experienced, and this can be visualized by a 'crossing' of decay lines.

The rates at which JICF mixing occurs are dependent on the exit velocity profile of the jet [19]. This in turn can be tied back to the growth rates of the SLVs. New *et al* [21] observed, via flow visualization of JICF, that the growth rates of SLVs in jets with a top-

hat (minimal boundary layer) exit velocity profile are much greater than those found in jets with a parabolic (fully-developed boundary layer) exit velocity profile.

1.3.2 Flame Stabilization in a Reacting Jet in Crossflow

A second critical piece of the physical context as relates to RJICF NOx production is the influence of combustion on the JICF, and in turn, the coupled influence of the flowfield on flame stabilization. The manner, and consequently the location, of flame stabilization is particularly important with regards to pre-flame mixing in the RJICF. This is commonly referred to as the manner of attachment and the degree of flame lifting. Broadly speaking, RJICF flames can be characterized as attached or lifted depending upon the flame leading edge being located at the jet exit or at some point downstream. In literature, two distinct attachment locations are often referred to; namely the windward (upstream) and leeward (downstream) sides of the jet exit. Steinberg *et al* [22], who investigated heated H_2/N_2 jets injected into a heated air crossflow, observed the leeward branch oscillated less in location than the windward branch due to the presence of a low speed region generated by the recirculation zone behind the jet. The more transiently located windward branch was observed to stabilize over a wide range of locations, from near the jet exit to the flame tip. In premixed ethylene/air jets injected into vitiated crossflow, Wagner *et al* [23-25] also observed the two flame branches, with the windward branch again more unsteady in its stabilization location. The windward branch exhibited full attachment, windward liftoff with unsteady location of stabilization, and full windward

branch blowoff. This final conditions is referred to herein as lee-stabilization. Schmitt *et al* [26] observed fully attached behavior in premixed natural gas/air jets injected into vitiated crossflow. For equivalence ratios above 0.77, the flame was observed to originate inside the injector tube due to the deposition of hot crossflow fluid upstream of the jet exit by the horseshoe vortex system located at the interface of the windward edge of the jet and the crossflow boundary layer.

The point of flame stabilization in lifted flames, whether a windward branch or the entire flame, is termed the 'flamebase' and is akin to an edge flame in some ways. Hasselbrink & Mungal [27] as well as Han & Mungal [28] investigated flame behavior of lifted RJICF flames of non-premixed methane jets injected into crossflowing air at ambient conditions. The flamebase exhibited premixed flame behavior and experienced strong flow/flame interaction, while the flame downstream was more diffusion based in nature with significantly less flow interaction. In the work presented by Steinberg *et al* [22] discussed earlier in this section, the windward branch flamebase exhibited premixed or tribrachial flame behavior, and its location was shown to be dependent on regions of high extensive principal strain-rate. Large Eddy Simulations (LES) conducted by Schulz & Noiray [29] of jets with parameters matching those investigated by Wagner *et al* [23-25] manifested the transient windward branch behavior, and described the transient windward branch stabilization location as a retreating edge flame that is intermittently "brought back" by auto-ignition. Figure 6 contains representative illustrations of the various flame attachment configurations discussed in this section.

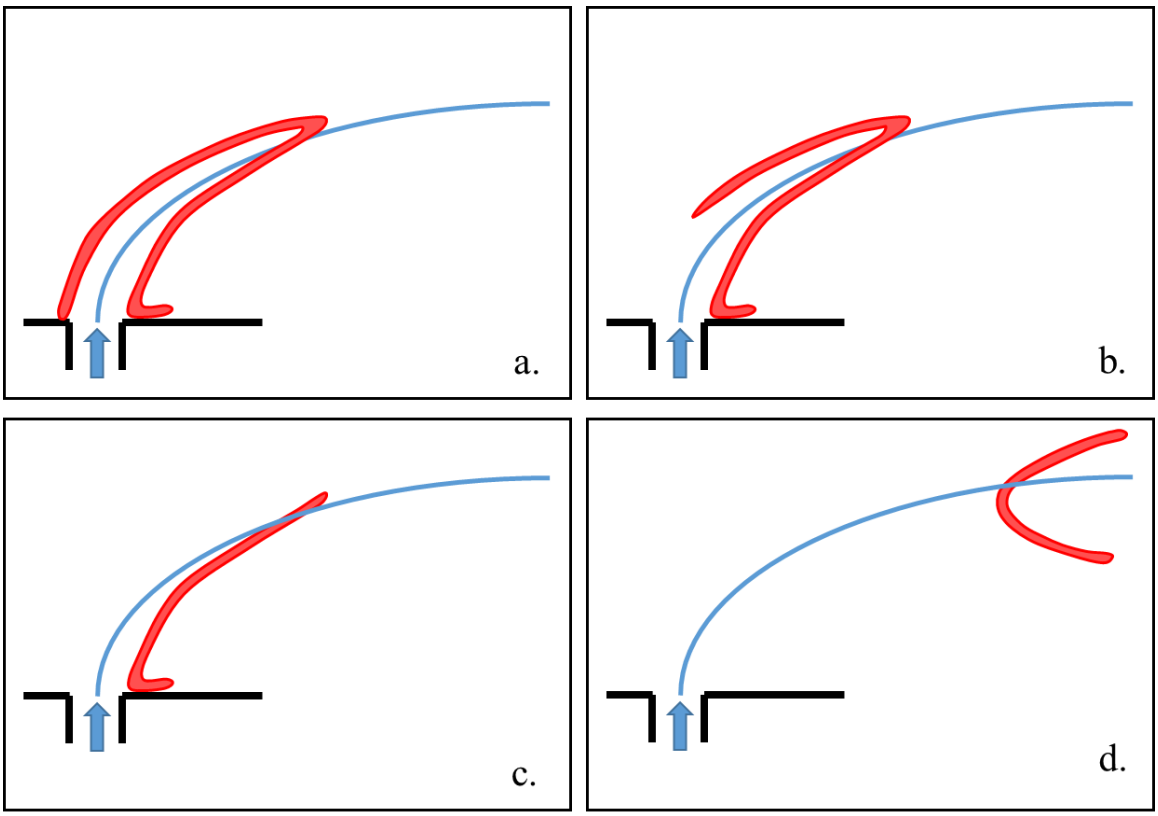

Figure 6 – Illustrations of center-plane section views for fully attached (a), windward lifted / leeward attached (b), lee-stabilized (c), and fully lifted flames (d) in premixed reacting jets in crossflow.

Attempts have been made to model the degree of lifting. Sullivan *et al* [30] showed that the flow times associated with the flame lift-off height of non-premixed jets of various compositions injected into high-pressure and -temperature vitiated crossflow correlated well to calculated auto-ignition times. Gautam [31] asserted, based on liftoff height in jets injected into quiescent air, that flamebase stabilization was propagation based and governed by turbulent flame speed. Kolb *et al* [32] correlated the lift-off height (LO_H) of lean premixed natural gas/air jets in high-temperature vitiated crossflow by incorporating

both auto-ignition and turbulent flame speed considerations. The resultant correlation, Equation 9, indicates the ratio of a mixture Karlovitz number (Ka_{mix}) that represents the flame speed contribution and an ignition delay Damkohler number (Da_{ign}) as the governing parameter in determining liftoff.

$$LO_H = 9.7\left(Ka_{mix}/Da_{ign}\right)^{0.61} \tag{9}$$

The importance of liftoff in regards to pre-flame mixing is not strictly due to providing a temporal/spatial opportunity for the jet fluid and crossflow to mix. Nair *et al* [33] observed, via simultaneous stereographic high-speed particle image velocimetry (stereo-PIV) measurements and hydroxyl radical imaging with planar laser induced fluorescence (OH-PLIF), that the presence of the flame in the vicinity of the jet exit suppressed the growth rate of the SLVs in non-premixed jets composed of hydrogen and diluents injected into a vitiated crossflow. The suppression of these vortices would negatively impact the near-field mixing of a RJICF and impact the CVP structure. However, Nair *et al* [34] did confirm the presence of the CVP in a non-premixed methane RJICF using simultaneous tomographic PIV (tomo-PIV) and OH-PLIF.

1.3.3 NOx Production in a Reacting Jet in Crossflow

Little work has been done to investigate how observed flame behavior impacts the NOx production of these reacting jets. Bandaru and Turns [35] investigated NOx emissions from a reacting jet in a crossflow of air over a range of jet compositions and crossflow velocities and observed a lack of sensitivity of the NOx levels to these parameters, with the

exception of fuels noted for high soot formation such as ethylene. The heat loss to the soot particles causes a reduction in product temperature and thus a noticeable decrease in thermal NO formation. Lyle *et al* [36] investigated the impact of partial premixing in jet flame emissions by injecting rich premixed methane/air jets with a co-flow of air into quiescent air. No significant deviation from NOx emissions produced by fully non-premixed jet flames was seen for jet equivalence ratios (ϕ_{jet}) greater than 5.0. For $5.0 \geq \phi_{jet} \geq 1.5$ reduced NOx production was observed compared to the non-premixed case, with a maximum reduction of 25% at $\phi_{jet} \approx 1.5$. For values of ϕ_{jet} even closer to the stoichiometric condition a significant increase in NOx emissions was observed. This trend is supported by equivalence ratio's impact on flame temperature and in turn by thermal NOx production's exponential sensitivity to temperature as discussed in Section 1.3.3. It follows that the jets Lyle *et al* [36] observed evolved from high-temperature diffusion flames, to low-temperature rich premixed flames, and on to high-temperature near-stoichiometric premixed flames. Prathap *et al* [37] showed that, for a given bulk temperature rise of the flow due to the RJICF flame (ΔT), jet trajectory exhibited strong sensitivity to jet parameters such as momentum flux ratio and Reynolds number, but NOx production experienced little variation. Roa *et al* [38] demonstrated that NOx production from a RJICF was a strong function of ΔT. These results demonstrate that NOx production by a RJICF is primarily driven by the associated ΔT, but did not explore NO sensitivities to parameters such as jet fuel/air ratio or J for a given ΔT. Ahrens *et al* [39] observed a strong correlation between NOx production and local mixture fraction for lean premixed RJICF, indicating

the degree of mixing between the jet and the crossflow prior to combustion as a critical element to NOx reduction.

1.4 Research Questions and Report Outline

This report is focused at addressing three significant outstanding research questions regarding the implementation of axial staging in gas turbine combustion:

1. For a given firing temperature and residence time, what are the minimum theoretical NOx limits?
    - How much lower is this fundamental limit than the limits achievable with current architectures?
2. What do the actual fuel and air distribution patterns look like that attempt to achieve these theoretical values?
    - Then, what are the operational behaviors of such a combustion system?
3. What do local pre- & post-flame mixing patterns look like and how is the heat release distributed?

The remainder of this report presents the methods that were used to address these core research questions and the results of those investigations.

Chapter 2 describes the developed reactor modeling network that is capable of modeling the theoretical minimum NOx achievable with the use of axial staging in a gas

turbine environment. Chapter 2 further describes how the reactor model is able to incorporate finite entrainment and mixing between the main combustion zone and the axial staged injection, thereby investigating the sensitivity of minimum achievable NOx to these parameters.

Chapter 3 describes the results from the reactor model studies and presents the minimum achievable NOx in a gas turbine environment with axial staging. In addition, Chapter 3 presents the sensitivity of this NOx minimum to various factors.

Chapter 4 describes the experimental facility that was developed to investigate premixed fuel/air jets injected into high-temperature vitiated crossflow of lean combustion products. The design of experiments is also presented, laying out the methodology for answering the aforementioned research questions as well as the test conditions and parameter space. Chapter 4 also details the diagnostic techniques used to collect data, the processing methods used to analyze it, and an assessment of the related uncertainty.

Chapter 5 describes the experimental results from the investigations laid out in Chapter 4. This occurs in three sections. Section 5.1 describes the results of preliminary work conducted with rich premixed methane/air jets. This work was conducted over a wide range of crossflow temperatures and ΔT values. The NOx measurements are compared to the associated values of J, ϕ_{jet}, and lift-off distance (LO) for each jet. Section 5.1 seeks to address the scale of impact on NOx emissions by test parameters in relation to ΔT, and to highlight parameters of interest for further investigation.

Section 5.2 describes the results of the main body of NOx emissions measurements conducted on premixed ethane/air jets. This works is conducted over a wide range of J and ϕ_{jet} values and includes both fully developed pipe and top-hat nozzle jet exit velocity profiles. Data is presented where LO is varied independently from other parameters by doping the jet fuel with methane. The focus of the analysis presented in Section 5.2 is on the dependence of RJICF NOx emissions on ϕ_{jet}, LO, and exit velocity profile. Section 5.2 introduces the equivalence ratio of combustion (ϕ_{Flame}) as a governing NOx parameter and a function of ϕ_{jet}, LO, and mixing rate governed by exit velocity profile.

Section 5.3 presents time averaged pre-flame jet/crossflow mixing data, in the form of seeded jet mie scattering, of the same parameter space presented in Section 5.2. Section 5.3 focuses on more directly assessing ϕ_{Flame} values (via local mixture fractions) and its impact on NO production rates and correlating them to the measured NOx emissions.

Chapter 6 presents the methodology for conducting large eddy simulations of several reacting jets. The selected simulation parameters mimic experimental data points presented in Chapter 4.

Chapter 7 presents the results from the LES. The results highlight the local behavior of the RJICF with regards to heat release, flame position, NO production, and other parameters.

Chapter 8 concludes this report with a summary of key findings and a discussion of recommendations for future work in this avenue of scientific investigation.

CHAPTER 2. REACTOR NETWORK METHODOLOGY

A chemical reactor network (CRN) approach is used for NOx prediction; analysis of the overall combustion system is separated into predefined sections of the combustor based on the flow field [40]. CRN modeling is a common approach utilized in analyses of LPM systems for emissions predictions [11, 41]. This approach has also been used in gas turbine combustor design [42] and optimization methodologies [43, 44] to obtain optimum designs for use in engine cycles. This chapter discusses how the CRN methodology is applied to the investigation of axially staged NOx production as part of this project.

2.1 Ideal Reactor Model

In the pursuit of establishing a fundamental minimum NOx level achievable by staged combustion, the CRN system was first divided into the main (or pilot) burner and the secondary (injection) stage, as seen in Figure 7. These can be further subdivided into specific regions if necessary. This approach allows for the configuration of regions and reactors with idealized flow fields, but with detailed chemical kinetics. Kinetic calculations are performed using ANSYS Chemkin, and a MATLAB wrapper is used to invoke these calculations for various dynamically varied design parameters.

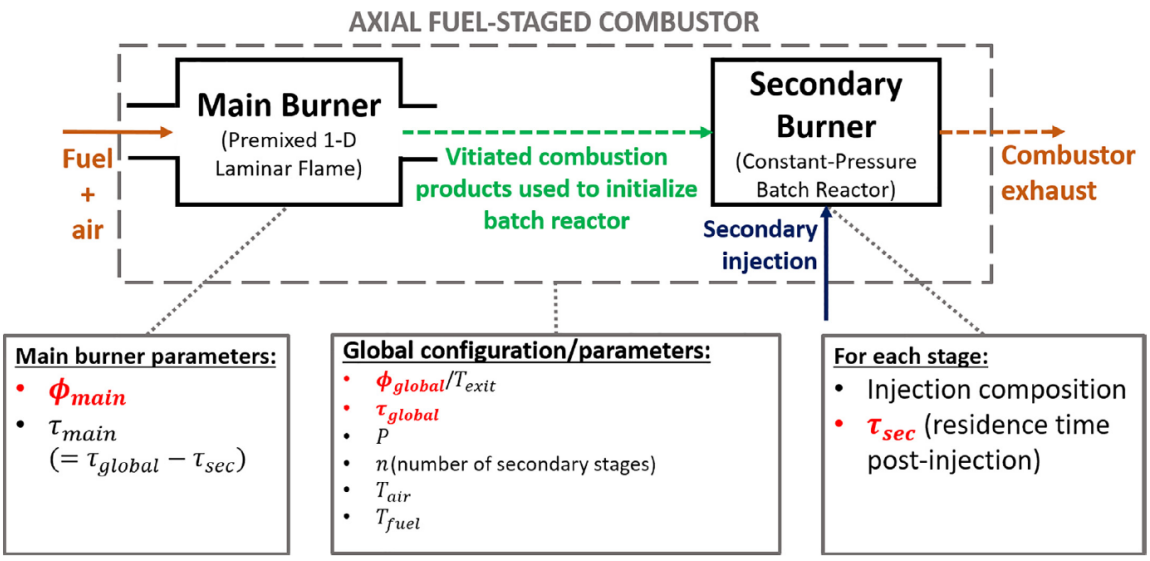

Figure 7 – Chemical reactor network model of the axially-staged combustor used for investigation of fundamental minimum. Dashed lines into and out of closed reactors indicate transfer of thermodynamic state information.

The model is used to study the NOx formation characteristics for a fuel-staged combustor architecture at typical gas turbine operating conditions. Parameters that are held constant in the study are the pressure (25 atm), fuel composition (methane), secondary injection composition (pure fuel), number of secondary stages (n = 1), fuel temperature (300 K), and air preheat temperature (650 K). Additionally, the baseline operating condition for a target cycle efficiency of 65% is used in most of the results shown in this work; this corresponds to a firing temperature (T_{exit}) of 1975K, which is achieved by a ϕ_{Global} of around 0.63. Parameters that are varied in this study are shown in bold red letters. The dependent parameters in this work are τ_{main} (dependent on τ_{global} and τ_{sec}) and T_{exit} (dependent on ϕ_{Global} for a given T_{air}, T_{fuel} and P).

2.1.1 Main Burner

The main burner is modeled as an LPM- type combustor –a configuration typical of staged combustors currently in operation [45] . This combustor is in turn modeled as a one-dimensional premixed laminar flame followed by a constant-pressure batch reactor. The residence time of the main burner, τ_{main}, is the combined residence time from the flame and the batch reactor. The spatial coordinates used by the CHEMKIN PRE-MIX code [46] are converted into temporal coordinates for the purposes of calculating τ_{main}.

Freely propagating premixed laminar flame solvers such as that found in the PREMIX routine [46] specify the flame location through an estimate of the temperature profile. Consequently, flames of different conditions (equivalence ratio, preheat temperature, etc.) are situated at roughly the same region in the spatial domain. The temporal "locations" of flames of different equivalence ratios, however, differ due to the difference in flame speeds, leading to situations, whereby lean flames have unreasonably long ignition times while near-stoichiometric flames ignite almost instantaneously. A definition of the point in the spatial domain that represents the initial time (t_0) should therefore maintain consistency across various equivalence ratios and enable the accurate representation of flame physics on a temporal basis. The point of peak formaldehyde (CH_2O) concentration is a good indicator of the beginning of the preheat zone in methane–air flames of different equivalence ratios, which allows the entire flame to be captured in

the time domain. As such, defining t_0 as the point of peak CH_2O ensures that all cases with burning solutions ignite before the end of the main burner (τ_{main})

Beyond t_0, the residence time at each location is obtained through numerical integration of the axial velocities and distances between consecutive grid points. NOx chemistry in pre-mixed flames has been found to be dominated by temperature effects and is therefore relatively insensitive to turbulence effects [47]. While in-flame NOx formation rates increase with turbulence level, this effect is negated by the decrease in flame length (i.e., residence time) as turbulence increases [48]. In addition to this justification for the use of a laminar (instead of a turbulent) flame regime at the main burner head end, the laminar flame model increases fidelity in the simulation of NOx chemistry within a flame, which is affected by the diffusion of reactants and products into the reaction zone.

2.1.2 Secondary Stage

The second stage of the combustor is separated into two sections:

1. A pre-mixer between the reactants injected in the secondary stage and the vitiated products from the first stage.
2. A constant-pressure, batch reactor in which the mixture can react but does not experience further entrainment of vitiated products from the main burner and secondary (injected) reactants.

With the goal of predicting minimum NOx in mind, the pre-mixer is modeled as a non-reacting device that completely mixes the two streams before reactions occur. This is a similar approach to the LPM technology used to minimize NOx in the main burner, with the only difference being that one of the "reactants" is now a stream of vitiated products of lean combustion instead of air. Indeed, this approach is stated by Sattelmayer *et al* [49] to ensure spatial homogeneity in the temperature distribution within the reaction zone, thus reducing local high-temperature regions, where NOx production rates are high. This approach is justified here, as the goal of this work is not to model a given embodiment of the staged combustion approach, where mixing would take a finite time; rather it is to model the theoretical minimum NOx levels.

2.2 Ideal Reactor Model Method

Answering the question of the theoretical minimum achievable NOx emissions using axial staging is a central focus of the project. The current work aims to solve a constrained minimization problem for any given firing temperature, which can be stated in standard form as follows:

Minimize: $[NO] = f(\boldsymbol{x})$

subject to: $g_i(\boldsymbol{x}) \leq 0$, $i = 1$, ..., m.

where $\boldsymbol{x}$ is the vector of design variables, and g_i represents the ith constraint.

Figure 7 also shows the list of design parameters that can be varied at each stage using the combustor model described in Section 2.1. In the current study, for a given ϕ_{Global} and

τ_{Global}, the parameters are chosen such that the only design variables in $\boldsymbol{x}$ are τ_{sec} and ϕ_{main}. Parameter sweeps are performed across these design variables for the target 1975K temperature; a commercial optimization pack- age (Phoenix Integration ModelCenter) is used to determine the minimum NO levels achievable by this architecture at other exit temperatures. The sensitivity of the results to the reaction mechanisms used in the simulations are discussed in Section 3.1.3.2. As noted earlier, the minimum theoretical NOx is a strong function of the constraint function $g_i(\boldsymbol{x})$, in particular with regards to CO emissions, as they interact strongly in terms of residence time and temperature. As we will discuss in Section 3.1.2.2, the inverse relationship between NO and CO emissions (low NO favors short residence times while low CO requires longer residence times) necessitates the discussion of minimum NO for a given maximum CO. This allowable level of CO manifests as a constraint in the NO optimization problem posed above and directly affects the minimum theoretical NOx level achievable by the staged combustor architecture. A set of different constraints on allowable CO can arise in lieu of part load operability, and the resulting design changes are discussed in Section 3.1.4.

2.3 Finite Mixing and Entrainment Model

The CRN model described in Section 2.1 assumed that the main burner vitiated products and secondary fuel mixed infinitely fast prior to chemical reactions. The relaxation of this assumption and its impact on AFS NOx production is a key focus of this project. The existing literature has shown that emissions in typical staged combustion

systems are limited by large-scale entrainment rather than small-scale mixing [], thus the present model seeks to incorporate the effects of finite-rate entrainment while retaining the assumption that small-scale mixing (at or below the Kolmogorov scale) is infinitely fast. As with the CRN model discussed in in Section 2.1, this model is designed as a generic framework that allows one to simulate reaction kinetics based on physical time scales that are directly related to physical parameters. The authors hope that this model will provide the community with a unified platform for the analysis of entrainment-related combustion problems governed by fundamental scientific parameters.

Consider a shear layer formed by the parallel flow of two fluids composed of different reactants and flowing at different velocities. The interface between the two fluids is unstable and is subject to the Kelvin-Helmholtz (KH) instability. Large scale coherent structures in the form of KH vortices transport reactant from one stream into the vicinity of the other on the other side of the shear layer before any significant molecular mixing occurs at the Batchelor scale. The flow can be conceptualized as consisting of two reservoirs (the two fluid streams) and an entrained region (the mixing layer). Within the entrained region, mixing (due to turbulent structures and molecular diffusion) is assumed to be infinitely fast, and the entrained volume is homogeneous before reactions occur. Figure 8 shows the two reservoir plus entrainment region conceptualization applied to the flow field of a reacting jet in crossflow. In this example the vitiated crossflow forms one reservoir and the jet fluid and potential core from the other reservoir. The robust mixing induced by the many coherent structures found in a RJICF create the entrainment region,

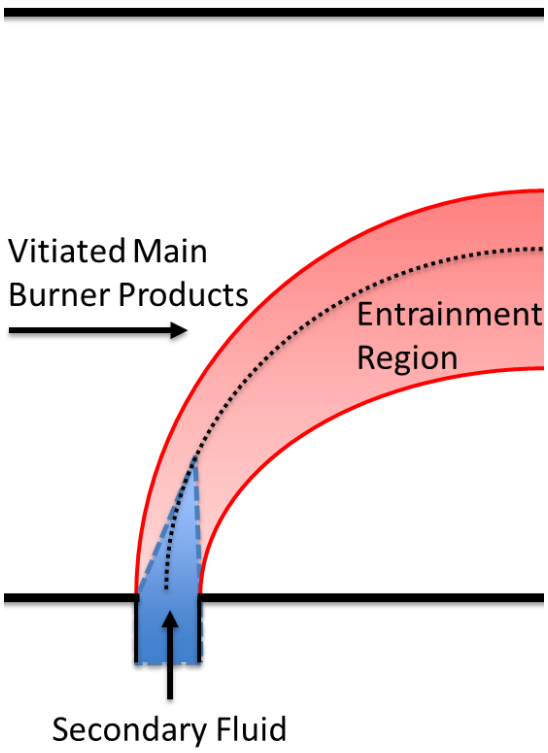

Figure 8 – Reacting jet in crossflow represented as two reservoirs and an entrainment region.

In an axially staged combustor the overall fuel-to-air ratio of the system can be expressed via ϕ_{Global} and is a function of the equivalence ratios and flow rates of both the main combustion zone and the secondary stage.. However, the rates at which the two streams are brought into the red region entrainment region (depicted in Figure 8) i.e., the entrainment rate, is in general not equal to but instead dependent on the flow rates of each stream in addition to other parameters e.g., Reynold's number, momentum flux ratio, Schmidt number, etc. Due to finite entrainment rates, real mixing flows require a finite distance, or characteristic entrainment length (ℓ_{ent}), before the local equivalence ratio

actually matches ϕ_{Global}. Additional entrainment based length scales can defined, such as the distance required before pure main and pure secondary fluid regions disappear ($\ell_{ent,main}$ and $\ell_{ent,sec}$ respectively). While there will still exist local regions of pure "reservoir" fluid in the flow field, an equivalence ratio for the entrained region can be defined (ϕ_{ent}). The equivalence ratio of the entrained regions is dependent on location within the flow field as related to the various entrainment length scales and asymptotes to ϕ_{Global} towards the combustor exit.

From this discussion it is apparent that two sets of flow rates for the reservoir streams need to be considered when modeling the flow field. The first set must reconcile ϕ_{Global} and the second to model the entrainment rates, which governs ϕ_{ent}. Furthermore, we wish to study the effects of entrainment rate in isolation while keeping all other parameters (on which entrainment rate may be dependent) fixed, especially those parameters that directly impact NO production. With these considerations in mind, a simple model of the flow field that enables fluid mechanics and chemical kinetics to be treated separately can be developed by casting the spatial distribution of a steadystate/averaged flow field into a temporal distribution. This approach applies a Lagrangian representation of the flow field, where a control volume is modeled as it evolves downstream. Two reconcile ϕ_{Global}, the two reservoirs can allotted an initial mass at the appropriated ratio. Consequently the flow rate from these reservoirs into the entrained regions will model the entrainment rate of the separate fluid sources.

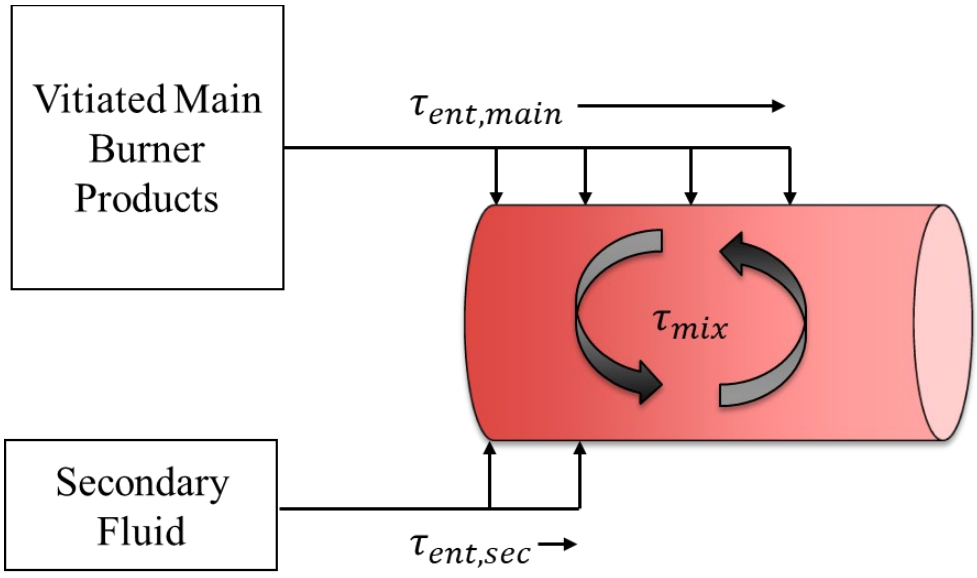

Figure 9 – Schematic of CRN model used for investigating finite entrainment and mixing effects.

Figure 9 presents a chemical reactor network developed on the basis of the model discussed in this section. The network contains an element for each partition in the flow field, namely one for each pure-fluid stream (reservoirs) and one for the entrained region. A CRN representing a staged combustor consists of three elements: a pure main fluid element, pure secondary fluid element, and entrained region. In the network, pure-fluid elements can be modeled as non-reacting reservoirs or constant-pressure batch reactors. The inlet flow rates of main and secondary streams are represented as amounts in this closed system. Each pure-fluid element (to which we assign an index i) has a prescribed mass M_i of fluid of a given composition χ_i at temperature T_i. For a staged combustor model, we model the main burner stream using a batch reactor to capture the full main burner NOx contribution and model the secondary stream using a non-reacting reservoir.

The entrained region is modeled as a constant-pressure batch reactor with multiple inlets. Doing imposes infinitely fast mixing within the entrainment region. The batch reactor inlets are connected to the pure-fluid elements of the network with prescribed mass flow rates $\dot{m}_i$ representing the entrainment rate of each stream. In physical systems, M_i and $\dot{m}_i$ would be coupled. With this framework, $\dot{m}_i$ can be independently controlled to study the effect of varying entrainment rates on reactor kinetics. One approach to controlling entrainment rate is to specify $\dot{m}_i$, however in this work entrainment was instead defined via a time scale $\tau_{ent,i}$ that corresponds to the time required for M_i to be fully entrained (reservoir mass to become 0). This approach creates a to the entrainment length scales found in physical flow fields discussed earlier in the section. In the application of the discussed CRN to work described in this report the entrainment time scales are constants, not functions of time or M_i.

2.4 Finite Entrainment Study Methodology

Parametric studies were performed using the CRN model described in Section 2.3. The parameters of interest to the study were the main burner and secondary stage entrainment rates and the impact varying these parameters had on NOx production in the CRN. The parameters shown in Table 1 are held constant throughout the simulations to simulate engine conditions. The selected value for ϕ_{main} is derived from the optimum value discussed in Section 3.1, it is the leanest fuel-air mixture within the flammability limit of a methane-air system that enabled autoignition of the secondary

stage. The GRI-3.0 mechanism is used throughout this study to reduce computational time.

Table 1 – Parameters held constant during finite entrainment study

Parameter	Value
T_{exit}	1975K
ϕ_{Global}	0.635
ϕ_{main}	0.3719
P	25 atm
T_{fuel}	300
T_{air}	650

CHAPTER 3. REACTOR MODELING RESULTS

This chapter discusses the findings from the chemical reactor network modeling conducted as part of this project, the methodology for which is outlined in CHAPTER 2.

3.1 Minimum Achievable NOx Under Ideal Axial Stage Conditions

The following results are obtained using the model detailed in Section 2.1 with methane as the fuel. Unless stated otherwise, results are shown for calculations of AFS combustors at engine conditions (i.e., 25 atm, τ_{global} = 20 ms) with GRI 3.0 [50] used as the detailed reaction mechanism. Furthermore, the reactor network model is assumed to be adiabatic and constant-pressure. Results are only shown for NO (in corrected parts per million on a dry basis) because NO is the largest constituent in the predicted NOx values. For reference, N_2O/NO levels are approximately 0.5 and 0.07 for studied configurations, where NO levels are on the order of 1 ppm to 10 ppm. Also, NO_2 levels are negligible (NO_2 < 0.01 ppm) for all conditions tested.

3.1.1 *NO Reduction Through Staged Combustion*

To emphasize the primary reason for the potential for NOx reduction in long residence time, AFS combustors, Figure 10 shows comparison between a typical LPM combustor and four different staging configurations, all with the same final combustion temperature of 1975K. The four configurations include two main burner equivalence ratios, ϕ_{main} and two secondary reactor residence times, τ_{sec}. These results demonstrate that the

AFS architecture can achieve varying levels of NO reduction depending on the choice of ϕ_{main} and τ_{sec}. Specifically, these results indicate, as might be expected, that a staged combustor with a leaner main burner, i.e., lower ϕ_{main} and later injection of secondary fuel is beneficial to the reduction of NO.

As a reminder, this lowering of NOx emissions is obtained under the assumption that any additional fuel rerouted from the main burner to the secondary stage for a fixed ϕ_{Global} is mixed with vitiated products from the first stage before any new reactions can occur. As can be seen in Figure 10(b), the thermal NO formation rates (i.e., NO gradients) remain essentially constant across each configuration, so long as the equivalence ratio (and temperatures) of the post-combustion zones are the same. The small dip in temperature and NO at the injection point is due to an increase in the mass of the system resulting from the addition of fuel at the secondary injector.

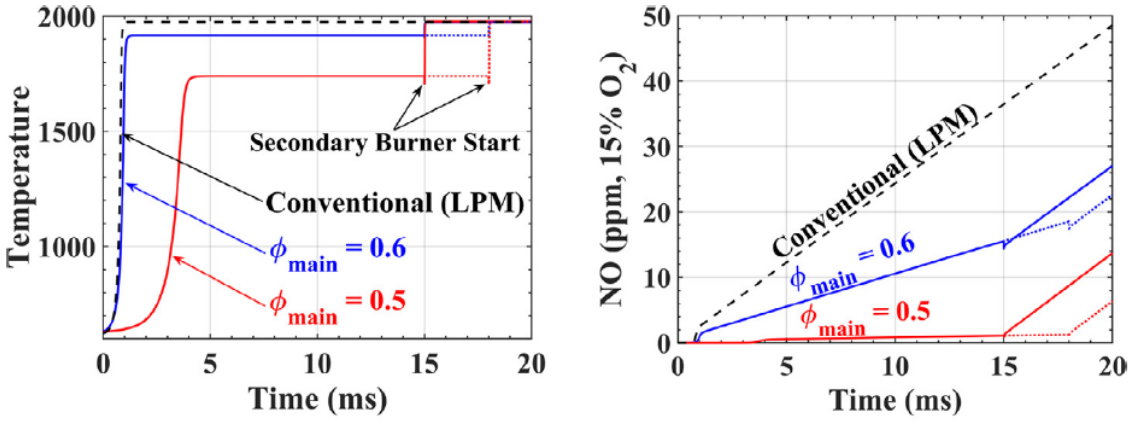

(a). Temperature time trace.

(b). NO time trace.

Figure 10 – Temperature and NO time traces calculated using the AFS combustor model at a 1975K exit temperature; solid lines represent cases, where τ_{sec} = 5 ms, while dotted lines are for τ_{sec} = 2 ms.

3.1.2 Parameter Sweeps

This section describes parameter sweep studies across the two design variables, ϕ_{main} and τ_{sec}, to determine the minimum achievable NO and the corresponding configuration.

3.1.2.1 Fuel Split Sweep

Figure 11 shows the dependence of NO and CO emissions as the fuel split is varied. NO production is reduced when more fuel is diverted from the main burner to the secondary reactor. This reduction in NO production rate is due to the reduction in main burner temperature, as stated in Equation 4 and evidenced in Figure 10a. For a fixed T_{exit} (again set to the baseline value of 1975K) and τ_{sec} , the main burner equivalence ratio was varied

from 0.4 (close to the lean flammability limit for methane) to 0.65 (the limiting LPM case that all fuel is injected at the main burner).

Thus, a very lean main burner is indeed a desirable configuration for the NO minimization at high temperatures. An improvement in NO emissions is achieved across the entire range of main burner equivalence ratios compared to the limiting LPM cases, although lower ϕ_{main} values produce diminished returns. Furthermore, the CO emissions remain at equilibrium levels across the fuelsplit range for the studied τ_{sec} , indicating that CO relaxation at 1975K is completed in less than 1 ms. It should be noted, however, that this analysis does not take into account stability (static and dynamic) issues that can arise when operating highly lean combustors and which could thus limit the achievable main burner equivalence ratio.

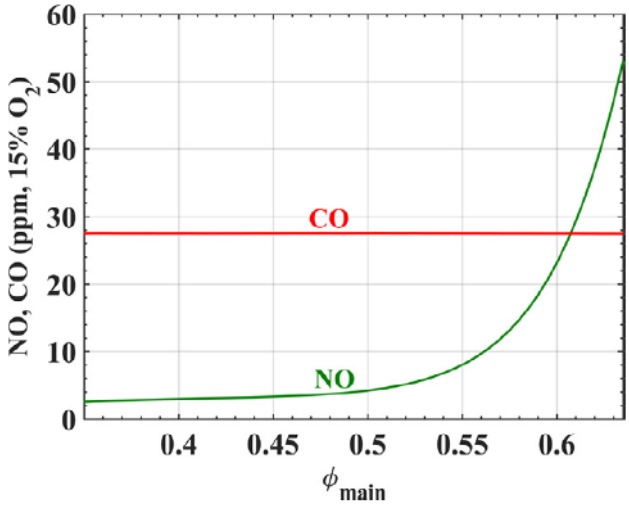

Figure 11 – Variation of NO and CO emissions with ϕ_{main} for a fixed T_{exit} = 1975K and τ_{sec} = 1ms

3.1.2.2 Secondary Reactor Residence Time Sweep

In addition to a dependence on ϕ_{main}, Figure 10b also reveals that NO emission levels in an AFS combustor are dependent on the residence time of the secondary reactor, τ_{sec}. For a fixed global residence time, varying τ_{sec} implies earlier or later injection of the secondary fuel. Figure 12 shows the results of a parameter sweep on this post-injection residence time, which enables identification of the minimum NO configuration for a given firing temperature. As expected, the results in Figure 12a indicate reduced NO emissions for shorter post-injection residence times. Down to $\tau_{sec} \sim 100$ μs, the NO emissions decrease linearly with residence time; for lower times, the NO produced by the secondary injection is not dominated by the thermal (Zeldovich) mechanism. In contrast to the NO behavior, CO levels at the combustor exit remain constant until τsec is less than roughly 0.2 ms. While complete mixing of fuel with the hot main burner products enables rapid combustion, at a short enough residence time, the secondary reactor does not achieve complete CO oxidation.

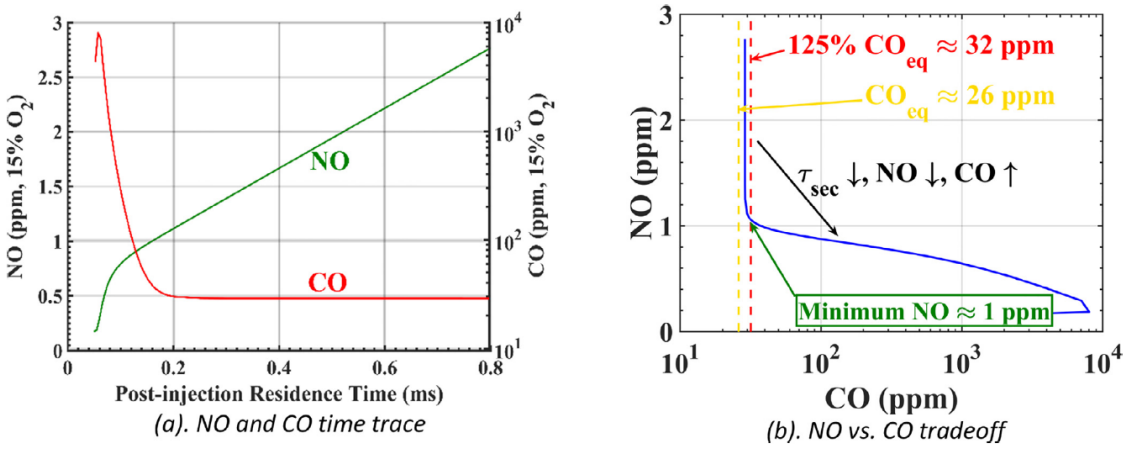

Figure 12 – NO and CO emissions with ϕ_{main} = 0.42 and T_{exit} = 1975K.

This is the familiar trade-off between NO and CO emissions performance, which is more clearly presented in Figure 12b, where NO emissions are plotted against CO emissions for a range of secondary reactor residence times. In order to find a minimum NO configuration, one must enforce some constraint to ensure satisfactory combustion performance. For example, we can require that the CO emissions are no more than 125% of the equilibrium CO levels based on the overall combustor equivalence ratio (and the associated adiabatic combustor exit temperature). The equilibrium CO level and this constraint are indicated in Figure 12b with vertical dashed lines. Of course, the more CO one is willing to allow at the combustor exit, the lower the achievable NO emissions.

3.1.3 Minimum NO – Single-point Design with 125% CO_{eq} Constraint

Using the Darwin Algorithm in ModelCenter with a 125% CO constraint, a set of fundamental NOx limits were predicted across a range of firing temperatures for τ_{global} =

20 ms. Optimization is performed independently for each temperature, so each result represents a single-point optimized configuration (ϕ_{main}, τ_{sec}). Figure 13 shows that the minimum achievable NOx for an AFS combustor is less than 1 ppm for firing temperatures below 1975 K, and on the order of 1 ppm at temperatures of 1975–2000 K. The significance of this result should be emphasized; it demonstrates that there is no fundamental reason that prevents very low NO emissions from being achieved for elevated flame temperature devices. Indeed, given that the most stringent NO emissions today are on the order of 3 ppm @15% O_2, this result indicates that the staging approach has significant potential to enable both increased efficiencies and reduced NO emissions.

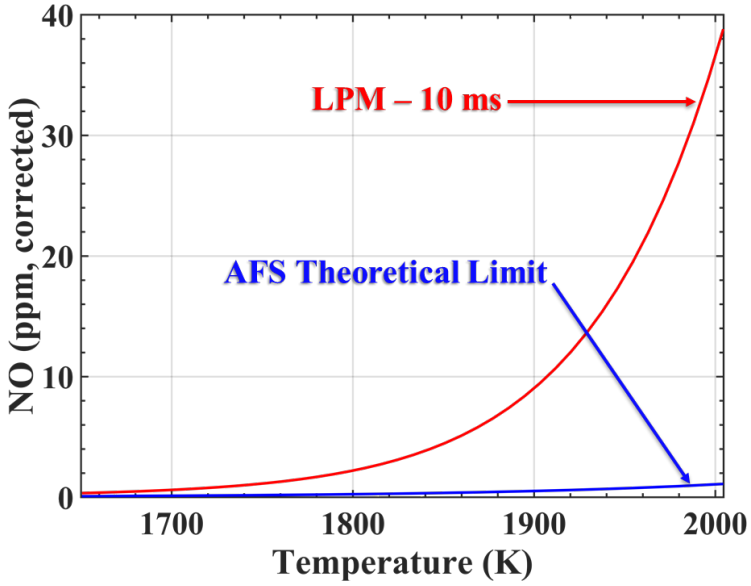

Figure 13 – Predicted minimum NO levels for AFS architecture (blue), subject to 125% equilibrium CO constraint, compared to what is achievable by 10 ms LPM system (red).

Figure 14 shows the corresponding configurations for the staged results obtained in Figure 13. As discussed in Section 3.1.2, the optimum main burner equivalence ratio is one that minimizes NO production in the main burner yet maintains operability. The optimum ϕ_{main} results in Figure 14 show that the optimal main burner in a staged combustor would be operated as lean as possible without sacrificing stability and secondary stage functionality. The optimal secondary stage, on the other hand, is one with the minimum amount of residence time required for sufficient CO relaxation. This is shown in Figure 14, where the optimum τ_{sec} increases with decreasing firing temperature because CO oxidation is slower at lower temperatures and thus requires more residence time. A trade-off between main burner NO, secondary stage NO, and secondary stage operability can be seen in Figure 14. At high temperatures, the lower τ_{sec} and higher ϕ_{main} values curtail the more dominant NO levels produced in the secondary stage (at the expense of slightly more NO from the main burner), whereas the lower ϕ_{main} and higher τ_{sec} values minimize the higher main burner NO levels and enable secondary stage autoignition at low temperatures.

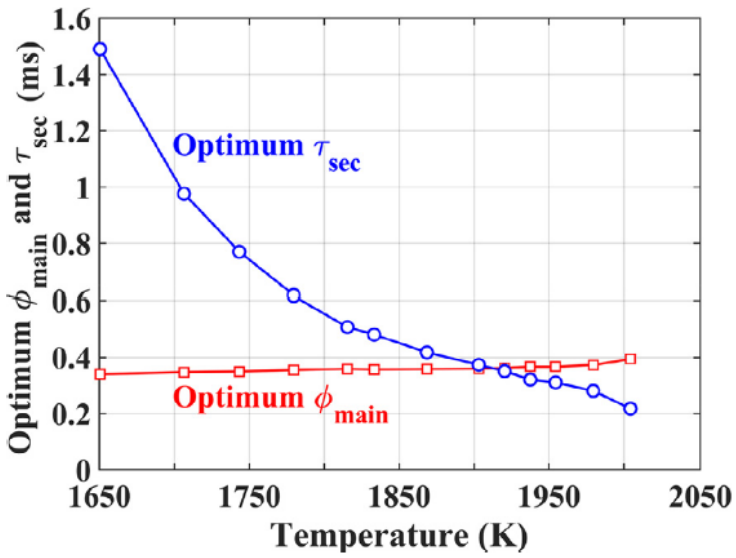

Figure 14 – Configurations corresponding to minimum NO for the AFS architecture

3.1.3.1 Global Residence Time Sensitivity

The results presented in the previous section were for a single global residence time. The sensitivity to τ_{global} of the NOx entitlement for staged combustion was examined by performing optimization studies for five global residence times, ranging from 5 to 25 ms. The shortest residence time studied here is comparable to minimum values obtainable in current engines. All the cases are for the target 1975 K firing temperature. As seen in Figure 15, the minimum obtainable NO for the AFS paradigm is essentially independent of the overall combustor residence time at the high operating temperatures required for 65% efficiency. While a conventional LPM combustor needs to be shortened to reduce NO at high firing temperatures, the AFS combustor can meet the 125% CO constraint while maintaining roughly the same low NO emissions without requiring residence times that

may be unobtainable in practical devices. As the global residence time of the staged combustor decreases, the optimum configuration for a shorter staged combustor changes slightly, favoring a higher ϕ_{main} and lower τ_{sec} for rapid CO oxidation.

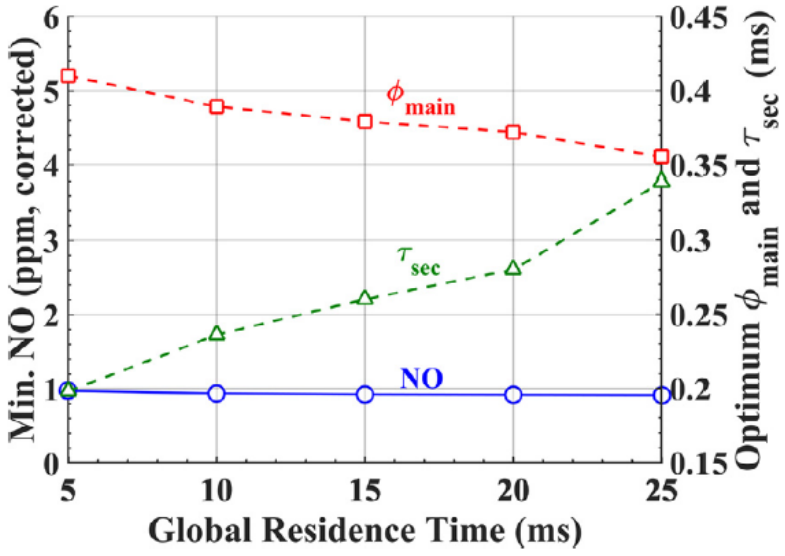

Figure 15 – Minimum NO achievable and corresponding main burner equivalence ratio for the 1975K AFS combustor a multiple residence times.

The above calculations demonstrate theoretical minimums for a single axial stage. A natural follow-on question is the extent to which further emissions improvements are achievable with multiple stages or even continuously distributed fuel injection. In the ideal case with infinitely fast mixing, configurations with multiple injection locations were tested but showed marginal benefit compared to the single injection configuration. For example, we repeated this process for two discrete axial injection points, whereby the optimum configuration resulted in an injection system where (i) most of the fuel is injected

in the second injector (i.e., the third stage), and (ii) the second injector is placed very close to the end of the combustor, similar to the single injector configuration. The lack of improvement for multiple injection locations is likely limited to the case of fast mixing.

3.1.3.2 Sensitivity to Kinetic Reaction Mechanism

A further question that must be addressed is the sensitivity of the results presented so far (both the trends and quantitative NO limits) to the reaction mechanism used, as recent studies have reported uncertainties surrounding the elementary NO reaction rates used in several widely-used reaction mechanisms [51]. This section presents calculations for several reaction mechanisms and shows that these key outcomes do not change. As a means of understanding the uncertainties in the current results based on the chosen GRIMech 3.0 mechanism, the same optimization routine used to obtain the minimum NO values presented in Section 3.1.3 was used to predict the fundamental NO limits for the AFS architecture for two other mechanisms: Konnov 0.6 [52] and UCSD [53]. Note that for each mechanism, the minimum NO results can be associated with slightly different staging configurations; the key trends in how the optimum configuration changes with operating conditions remain the same.

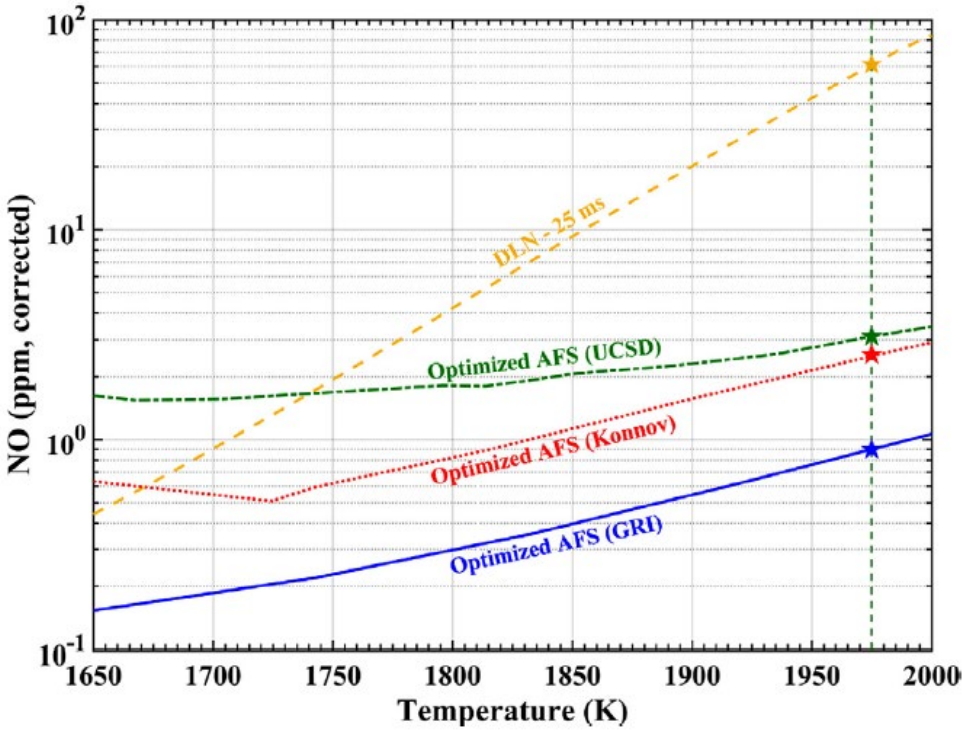

Figure 16 – Fundamental NO limits for staged combustion architecture for a range of firing temperatures determined with three different reaction mechanisms. LPM system is shown for comparison.

As seen in Figure 16, the choice of reaction mechanism does influence the predicted minimum NO levels in relative terms. The differences in absolute values, however, are small. All the optimized NO results are on the order of 1 ppm at 1975 K, regardless of the reaction mechanism. This is well below the value (~60 ppm) for the LPM configuration obtained using the GRI mechanism. It is also interesting to note that the GRI and Konnov mechanisms show similar trends with firing temperature, though the Konnov prediction is roughly 2.5 times higher than that for the GRI mechanism. The minimum NO predicted by

the UCSD mechanism is slightly higher than the Konnov result at 1975 K and shows a reduced sensitivity to firing temperature.

3.1.4 Minimum NO – Multi-point Design with 125% CO_{eq} Constraint at Part Load

While the foregoing results present the fundamental minimum NO levels achievable by staged combustors at various conditions such as operating temperatures and residence times, the optimal configurations were determined for single-point operating conditions. For instance, if one were to operate the optimal 1975K combustor with the 125% CO constraint (i.e., maximum allowable CO of 31.8 ppm) at part-load by reducing the secondary fuel, the CO emissions could become excessive due to the lack of residence time for sufficient oxidation. This section explores the minimum achievable NO emissions for systems that must meet multi-point design constraints. We first explore a two-point staged combustor design by applying the same maximum CO determined by the 125% CO constraint at full load (1975 K) at a chosen part load condition (1650 K). An optimization study is performed with the objective being to minimize NO at full load, subject to the new CO constraint. In contrast to the single-point design, the optimal staged combustor design under this constraint has a higher ϕ_{main} of 0.449 and a shorter τ_{sec} of 0.158ms. This design only increases NO by 0.1 ppm at 1975 K while successfully meeting the CO constraint at 1650K (which 1975K single point optimized solution exceeded by 20X). In this configuration, the staged combustor routes almost all the fuel through the main burner at part load; $\phi_{Global} = 0.45$ equates to an exit temperature of 1650 K. Therefore, a ϕ_{main} of 0.449

indicates that only 0.01% of the fuel is injected into the secondary burner to provide a temperature increase of only 2 K. While this solution does in fact give the minimum NO emissions under the two-point CO constraint, the improvement is insignificant compared to operation of the main burner at ϕ_{Global}. Consequently, we can take the optimum ϕ_{main} to be 0.45 in which case the staged combustor would operate in LPM mode at part load (i.e., with the second stage disabled), producing even less CO (0.8 ppm vs 31 ppm) at 1650 K. As such, an optimized staged combustor based on the two- point CO constraint would run the main burner at the global equivalence ratio for part load and minimize the residence time of the secondary burner such that there is sufficient time for autoignition and CO oxidation at full load.

A comparison of the performance of the multi-point design compared to the spectrum of single-point optimums is shown in Figure 17. As evident, the multi-point design does produce twice the NO compared to the single point optimum at 1975K in order to preserve part-load operability. However, in comparison to NOx produced by conventional architectures the multi-point design represents over an order of magnitude reduction in NOx at high flame temperatures.

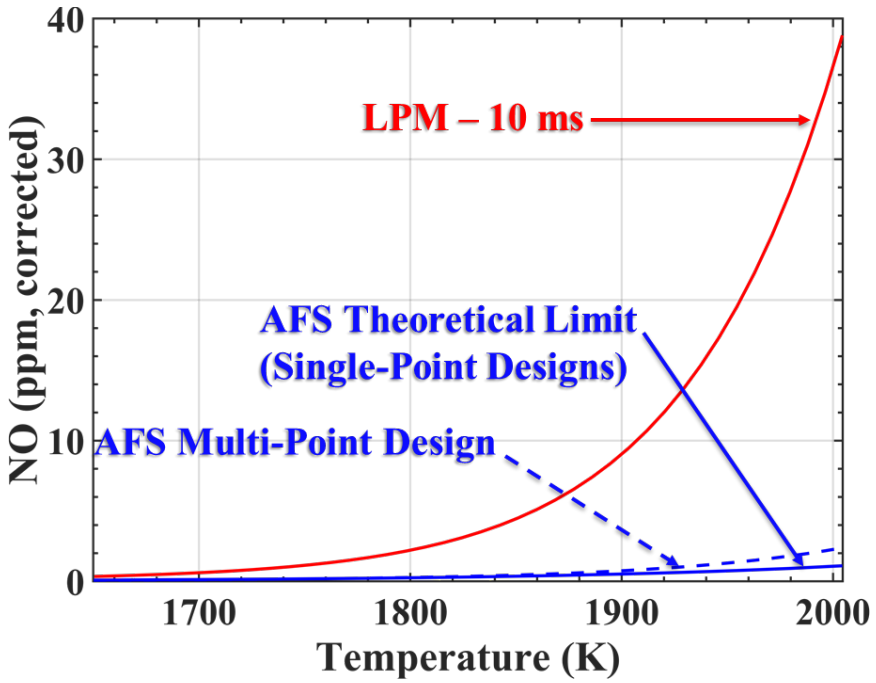

Figure 17 – Minimum NO as a function of exit temperature for optimum multi-point AFS combustor design (dashed blue) compared to single-point optimums for each temperature (blue) and conventional LPM (red).

3.2 Sensitivity of Staged Combustion NOx Entitlement to Finite Entrainment and Mixing

The results presented in Section 3.1 constitute theoretical minima that are based on an infinitely fast mixing assumption. An important question is the sensitivity of these results to mixing rates, which is the key challenge associated with reducing this concept to practice. The model and methodology for assessing these sensitivities was discussed in Section 2.3 and respectively. The results of the analysis are presented throughout the remainder of this Section. The ratio of the entrainment rates defined as $r_\tau \equiv \tau_{ent,main}/\tau_{ent,sec}$ will be an important parameter in the analyses to follow. It is helpful to

keep in mind the inverse relationship between the entrainment timescales and the entrainment rates, as both will be called upon interchangeably in this work; longer entrainment timescales correspond to lower entrainment rates and vice versa.

In this study, emissions values are reported on a corrected (volumetric, dry) ppm basis. Unless stated otherwise, NO values are reported from the point in a staged combustor when final CO burnout reaches 125% of equilibrium CO. As opposed to reporting NO at a fixed point in time, this approach provides a consistent basis on which to compare different entrainment regimes. For instance, larger entrainment timescales will necessitate longer residence times to allow for CO burnout, which leads to higher NO levels than that of combustors with faster entrainment.

3.2.1 Pure Fuel Secondary Stage

Figure 18 shows NO levels from the staged combustor model for various main burner and secondary stage entrainment rates. At low main flow entrainment rates, with $\tau_{ent,main} \approx 0.1$ ms, NO emissions approach the minimum levels identified in Section 3.1, indicating that entrainment time scales on the order of 0.1 ms can be considered "infinitely fast". As shown in Section 3.1, fast entrainment of both streams allows for quicker CO burnout, leading to shorter overall residence times and thus less time for NO production. Indeed, the optimum secondary stage residence time identified in Section 3.1 was approximately 0.2 ms. This value is also on the same order of magnitude as the "infinitely fast" limit just identified.

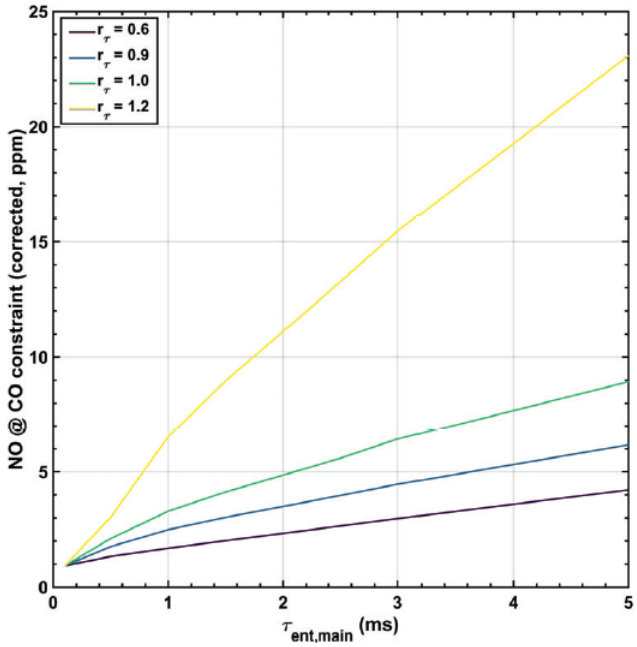

Figure 18 – NO emissions dependency on main vitiated flow entrainment time and secondary stage entrainment time (expressed through r_τ)

For a given value of r_τ , $\tau_{ent,sec}$ increases with $\tau_{ent,main}$. Consequently, increases in $\tau_{ent,main}$ with r_τ held constant serve to increase the total residence time of the secondary stage. It would therefore be expected that NO increases monotonically with $\tau_{ent,main}$ at constant r_τ a result of the linear dependence of thermal NO on residence time. This is confirmed by Figure 18. The degree of dependence, however, is a function of r_τ; or restated oh how quickly the main flow is entrained into the reacting region compared to the secondary injection. An r_τ less than or equal to unity maintains low levels of NO (below 10 ppm) even at high $\tau_{ent,main}$ of on the order of 5 ms. Conversely, cases with $r_\tau > 1$ have a strong dependency on $\tau_{ent,main}$ (i.e., residence time) and exhibit higher NO levels. NO

increases monotonically with r_τ between 0.6 and 1.2. NO sensitivity to r_τ also increases with $\tau_{ent,main}$. Fo example at $\tau_{ent,main}$ = 1 ms, doubling r_τ from 0.6 to 1.2 increases NO by 5 ppm (≈4x), whereas at $\tau_{ent,main}$ = 5 ms, the same change in r_τ yields an increase in NO by 21 ppm (≈6x). This increase in sensitivity is more clearly illustrated in Figure 19, which shows increasing NO–r_τ gradients between the different $\tau_{ent,main}$ cases.

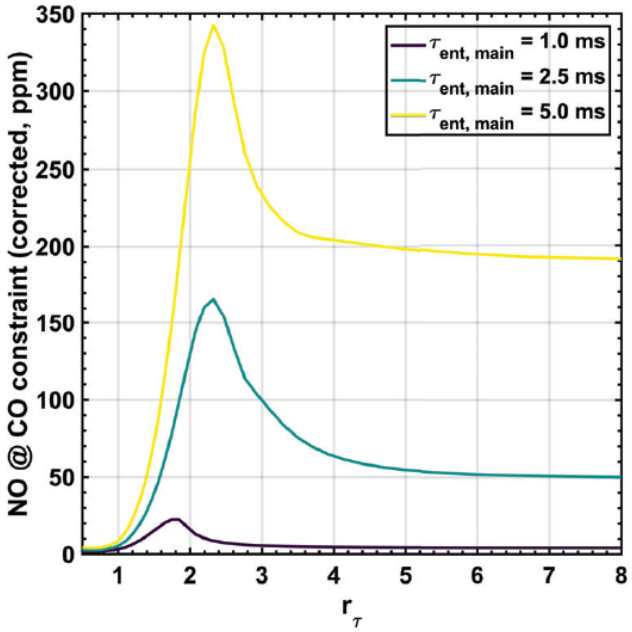

Figure 19 – NO emissions dependency on r_τ at various values of $\tau_{ent,main}$

Figure 20 plots time traces of temperature of the entrainment region and the system averaged NO level (accounting for NO production in both entrainment region and reservoirs) for select values of r_τ at $\tau_{ent,main}$ = 5 ms. The data provides addition insight into the observations made from Figure 18 and Figure 19 – namely that NO increases monotonically with $\tau_{ent,main}$ and r_τ, as well as the dependence of dNO/dr_τ on $\tau_{ent,main}$.

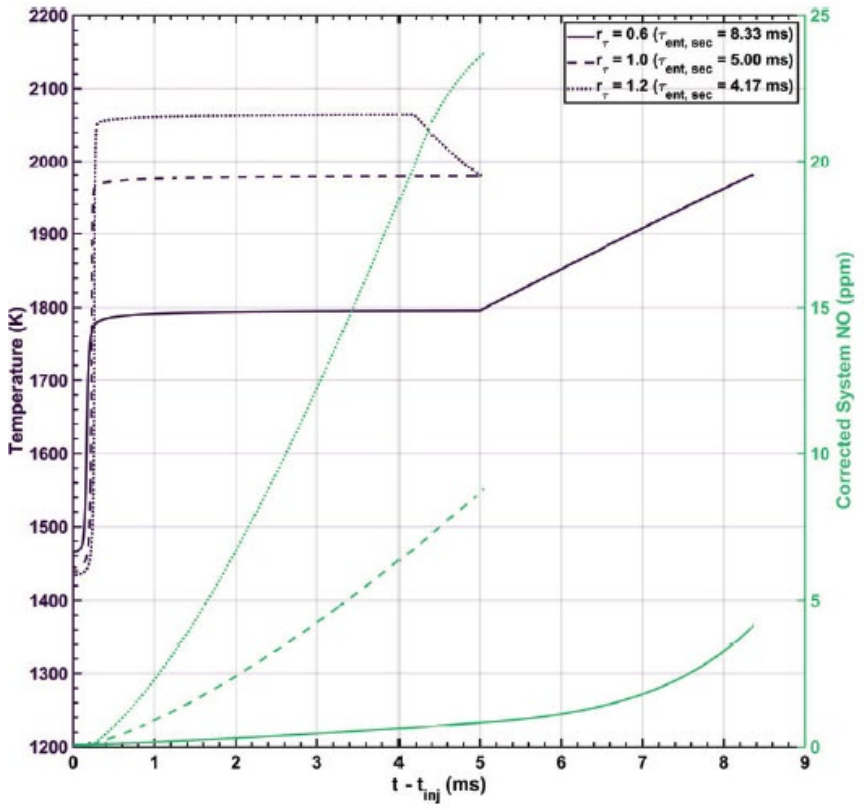

Figure 20 – Temperature and NO time traces of CRN calculations for select values of r_τ (0.6, 1.0, 1.2) at $\tau_{ent,main}$ = 5ms

In the r_τ = 0.6 case (solid lines), vitiated products from the main burner finish entraining earlier than the secondary fuel. The entrained region burns at a constant $\phi_{ent} < \phi_{Global}$ while both streams are entraining and afterwards ,while the secondary fuel continues to entrain, at increasingly higher ϕ_{ent}. The system eventually reaches ϕ_{Global} and the target temperature of 1975 K.

For r_τ = 1.0 (dashed lines), both streams are entrained such that $\phi_{ent} = \phi_{Global}$ throughout the calculation. The entrained region thus burns at the final temperature and the

corresponding NO production rate until there is complete entrainment of both reactant streams and sufficient oxidation of CO. This results in higher overall NO production than the $r_\tau = 0.6$ case, which only attains 1975 K (and the corresponding NO production rate) near the end of the entrained region. The $r_\tau = 1.0$ case and the infinite mixing and entrainment case in Section 3.1 exhibit an interesting similarity – both models burn at the target equivalence ratio throughout the secondary stage, with the primary difference being different residence times.

As seen in Figure 18, the $r_\tau = 1.2$ case (dotted lines in Figure 20) exhibits the highest NO level. This is most clearly understood through the evolution of the local temperature in the entrained region. Here, secondary fuel entrains faster than vitiated main burner products and consequently finishes entraining earlier than the main burner fluid stream. As such, the entrained region burns $\phi_{ent} > \phi_{Global}$, and more importantly closer to stoichiometry compared to $r_\tau \leq 1.0$. This causes a temperature overshoot in the entrainment region beyond the final temperature. This temperature overshoot results in significantly higher NO production rates as evidenced by the NO traces shown in Figure 20, where the $r_\tau = 1.2$ case has the steepest NO slope among all three cases. The higher temperature also leads to the increased sensitivity of NO to $\tau_{ent,main}$ originally observed in Figure 18.

For $\tau_{ent,main} < 5$ ms and $0.6 \leq r_\tau \leq 1.2$, NO levels remain at reasonably low levels. For reference, the minimum NO limit for an ideal LPM combustor with 20 ms residence time under similar operating conditions is 25 ppm. However, an entrainment ratio less than

unity is impractical in staged combustor configurations that employ transverse jets in crossflow. From the point of view of this flow field, the fuel injected by the jet is consumed before all of the crossflow material is entrained. In other words, r_τ is typically greater than unity and represents situations where the secondary mixture is consumed before all the crossflow fluid has entrained into the jet.

Figure 19 includes results for such cases where $r_\tau > 1$. For $\tau_{ent,main} > 1$, NO values are on the order of 100 ppm – significantly above current emissions regulations. Compared to when $r_\tau \leq 1$, NO levels for $r_\tau > 1$ exhibit a higher dependence on $\tau_{ent,main}$, which dictates overall secondary stage residence time. For the range of $\tau_{ent,main}$ tested, a region of high NO exists aat $1.8 \leq r_\tau \leq 2.3$ as shown by the peaks in Figure 19. In this region, slight variations in r_τ can significantly change the amount of NO produced, as do slight perturbations in $\tau_{ent,main}$. In other words, NO production is highly parametric sensitive when the secondary stream entrains roughly twice as fast as the main burner. Beyond the peaks around $r_\tau \approx 2.3$, NO decreases monotonically with r_τ and achieves lower levels (albeit still above regulatory limits), and are less sensitive to increases in r_τ .Of particular interest is the ability of the $\tau_{ent,main}$ = 1.0 ms case to maintain NO levels below 30 ppm across the entire range of r_τ , indicating that so long as the main burner is fully entrained in approximately 1.0 ms, a designer can allow the secondary fuel stream to entrain faster or slower than the main burner stream. This is another result of the linear dependence of NO on residence time – if the overall residence time is capped at 1 ms, NO levels will be relatively low regardless of the rate at which the secondary fuel entrains.

In Figure 20, a temperature overshoot was when secondary fuel entrained faster than the main burner stream such as in the $r_\tau = 1.2$ case. This overshoot was due to $\phi_{ent} > \phi_{Global}$. Figure 21 shows temperature and NO time traces for three additional values of r_τ. As r_τ increases further above 1.2, the entrained region burns at increasingly higher equivalence ratios, leading to a significantly larger overshoot temperature that drives the sharp rise in NO when r_τ passes from 1.2 to around 2.3. This trend peaks near the stoichiometric adiabatic flame temperature (≈ 2460 K for a methane-air system with the initial conditions used in this study). In fact, due to the fast secondary entrainment rate when $r_\tau = 6.0$, the entrained region actually ignites rich and passes through $\phi_{ent} = 1$ before eventually reaching ϕ_{Global}.

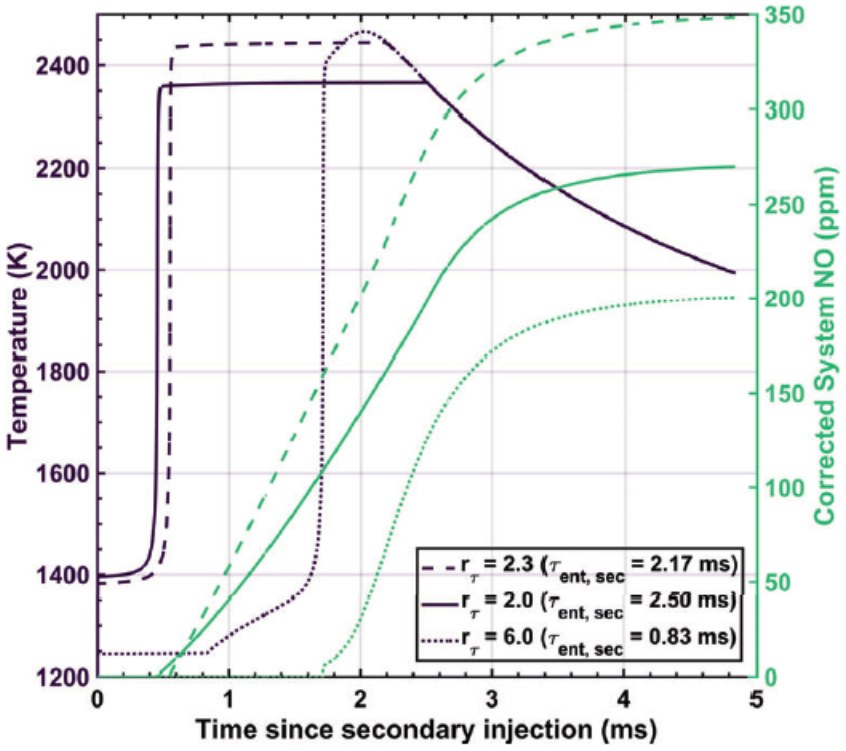

Figure 21 – Temperature and NO time traces of CRN calculations for select values of r_τ (2.0, 2.3, 6.0) at $\tau_{ent,main}$ = 5ms

It should, however, be observed that NO production is not governed by overshoot temperature alone. This is highlighted by the $r_\tau = 6.0$, which does reach the peak overshoot temperature, yet does not yield the highest NO emissions compared to other cases. The combination of elevated temperatures, time spent at those temperatures (as shown by r_τ = 2.3 case), and the availability of O_2 ($\phi_{ent} < 1$) is the cause of the highest NO levels. A significant portion of the difference in time spent at the peak overshoot temperature between the r_τ = 2.3 and 6.0 cases can be attributed to the delay in ignition after the secondary stage begins. The former ignites at around 0.5 ms while the latter ignites at

around 1.6 ms. This difference in ignition delay is in turn driven by the difference in initial temperature of the entrained region, which depends on the temperatures and entrainment rates of both incoming streams. For example, increasing the entrainment rate of secondary fuel (which is colder than the main burner) leads to a lower initial temperature and thus increases ignition delay. Likewise, lowering the temperature of the secondary fuel stream while maintaining constant entrainment rates also increases ignition delay.

Recall that thermal NO production in high-temperature combustion environments depends on temperature and residence time. In an axial fuel-staged combustor with finite entrainment, these two parameters manifest themselves as the maximum temperature in the combustor and the time spent at those temperatures. We have seen that cases with temperatures that stay below the final temperature produce lowest NO levels. These cases burn at equivalence ratios below ϕ_{Global} and eventually "work" their way up to the final equivalence ratio, thereby reducing time spent at the maximum temperature. For cases where a temperature overshoot exits, time spent at the maximum temperature can be reduced primarily by entraining the main burner stream faster and to a lesser extent by delaying autoignition.

3.2.2 Effect of Secondary Equivalence Ratio on NO

The results presented in Section 3.2.1 demonstrate that rapid entrainment of main burner products ($r_\tau < 1$) or predominately rich premixed secondary combustion ($r_\tau \geq 4$) can enable low NOx. In either case, the slower of the two entrainment rates controls the NO

production to a greater extent than r_τ. However, in applied flow fields such as the RJICF it is difficult to precisely control these entrainment rates This section describes how a variable secondary equivalence ratio (ϕ_{sec}) can provide an extra degree of control over NO emissions without having to design a combustor with a flow field that enables the aforementioned entrainment characteristics. The effect of ϕ_{sec} on NO is elucidated by examining the intermediate physical parameters affected by ϕ_{sec} – namely temperature and time. In addition, the sensitivities of NO to entrainment rates and secondary equivalence ratios are also characterized to provide readers with a sense of the design landscape.

In the CRN model, ϕ_{sec} is varied while ϕ_{Global} and ϕ_{main} are held constant. These three equivalence ratios and the total mass flow rate are specified to determine the sizes of each reservoir for the CRN model.

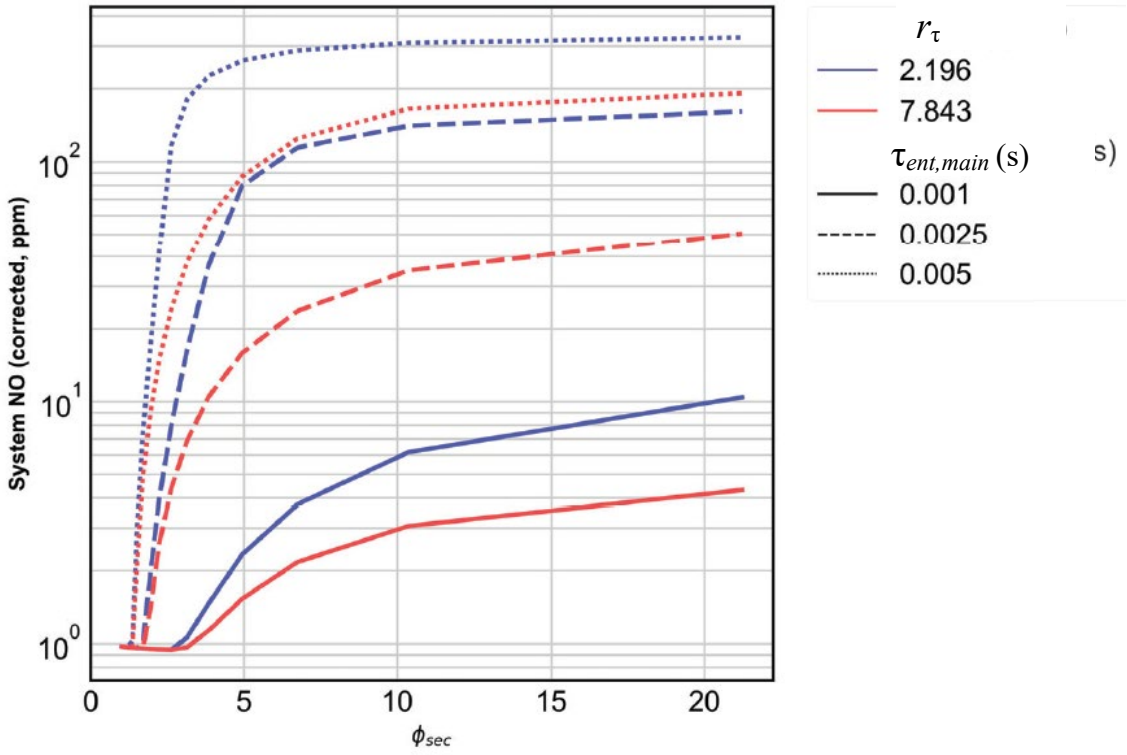

Figure 22 – NO dependency on ϕ_{sec} calculated at various values of r_τ and $\tau_{ent,main}$

Figure 22 shows the variation in NO with ϕ_{sec} for $\tau_{ent,main}$ = 1, 2.5, and 5.0 ms and $r_\tau \approx$ 2.0 and 8.0. The upper limit on ϕ_{sec} can be taken as the limiting pure fuel case whereas the lower limit is the minimum ϕ_{sec} that allows the secondary mixture to reach the final temperature within 15 ms. In general, NO levels are seen to increase with ϕ_{sec}, with a pure fuel secondary stream resulting in the highest NO. This reduction in NO with reduced ϕ_{sec}, stems from the reduction in peak temperature and increase in ignition delay. This is observable in the temperature and NO time traces plotted in Figure 23, which plots several ϕ_{sec} cases for r_τ = 2.1 and $\tau_{ent,main}$ = 5.0 ms.

Referring back to Figure 22, each combination of $\tau_{ent,main}$ and r_τ, three NO-ϕ_{sec} gradients exist. At $\phi_{sec} \approx 1.0$, NO levels stay near the minimum value and do not vary with ϕ_{sec}. A region of high dNO/dϕ_{sec} exists as ϕ_{sec} increases. This rapid rise occurs at lower values of ϕ_{sec} for cases with higher $\tau_{ent,main}$. This region of rapid change is driven by decreases in the temperature overshoot afforded by lower ϕ_{sec}. Cases with slower main entrainment require a leaner secondary stream to achieve a similar NO reduction compared to cases with faster main entrainment. Finally, a region of slow change in NO occupies the upper ϕ_{sec} ranges. This region represents cases where ϕ_{sec} affects the ignition delay more than the overshoot temperature. This region starts at lower ϕ_{sec} values for cases with slower main entrainment rates, indicating that cases with slower main entrainment tend to linger at higher temperatures.

Figure 24 shows the effect of reducing ϕ_{sec} from approximately pure fuel to a stoichiometric secondary on the relationship between NO and r_τ, which was previously seen for the pure fuel case in Figure 19 in Section 3.2.1. For $r_\tau \geq 1$, NO decreases monotonically with ϕ_{sec} – as observed in Figure 22. More interestingly, we observe a downwards shift in the entire NO-rτ curve as ϕ_{sec} is decreased, with the peaks (which occur in cases that spend a long time at high overshoot temperatures) shifting to lower r_τ values. When $r_\tau < 1$, NO actually increases slightly as ϕ_{sec} decreases. This is because these cases start off more fuel lean due to faster main entrainment, thus the longer ignition delay cause by a decrease in ϕ_{sec} provides more time for secondary fuel to mix with the main stream and burn at higher equivalence ratios closer to the final ϕ_{Global}.

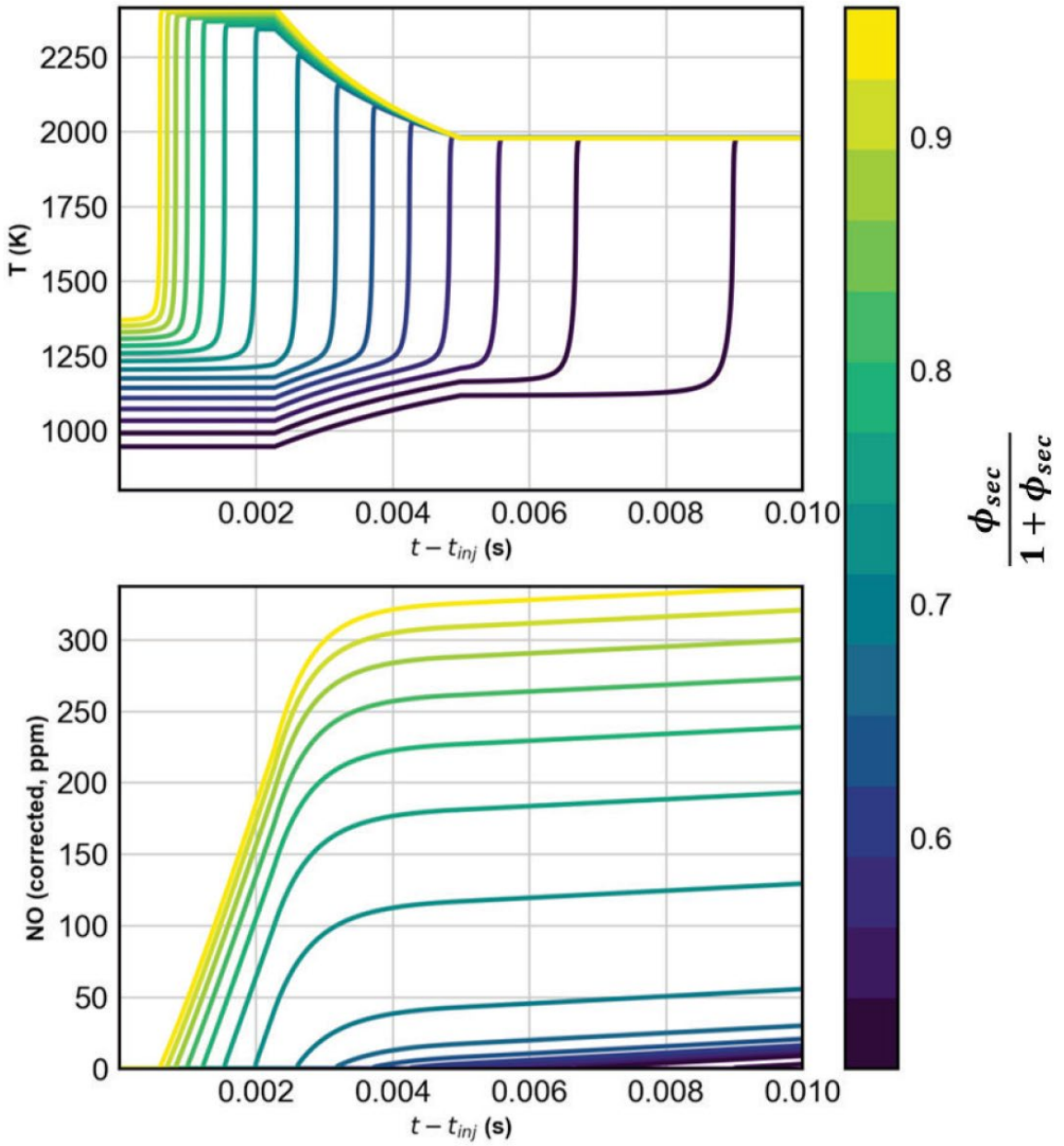

Figure 23 – Temperature and NO time traces for various values of ϕ_{sec} with r_τ = 2.1 and $\tau_{ent,main}$ = 5ms

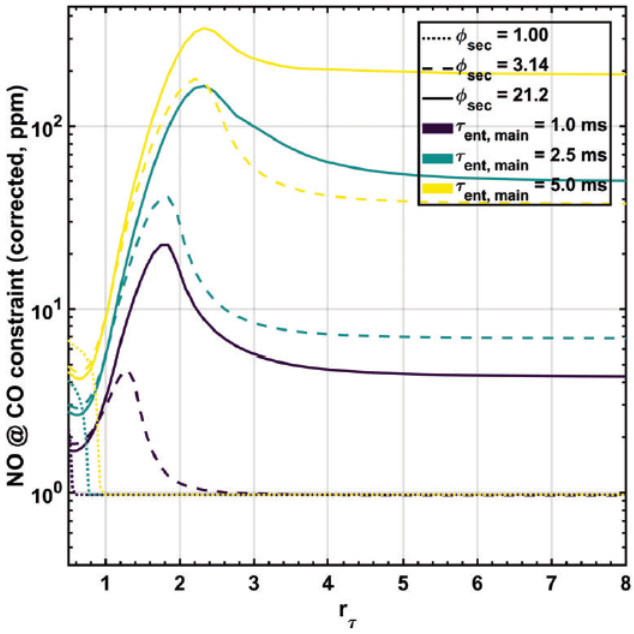

Figure 24 – NO dependency on r_τ for various values of ϕ_{sec} and $\tau_{ent,main}$

CHAPTER 4. EXPERIMENTAL METHODOLOGY

This chapter describes the experimental facility, the design of experiments, as well as the diagnostic methodology and equipment employed in the experimental investigations completed as part of this project.

4.1 Reacting Jet in Crossflow Test Facility

The experimental facility was designed to provide lean, high temperature products of natural gas/air combustion in order to auto-ignite premixed jets of methane and air at atmospheric pressure. The facility was heavily modified from that used by Wilde in his investigation of reacting jet dynamics [54]. The facility was used in multiple configurations over the course of the investigation described in this report. Each configuration is described separately in the subsequent sections.

4.1.1 Test Facility Configuration for Preliminary Investigation

The primary components of the facility include the main burner, flow conditioning section, test section with secondary injection, and chemical quench section. A schematic of the facility as it was used to investigation the parameter space described in Section 4.2.1 is provided by Figure 25.

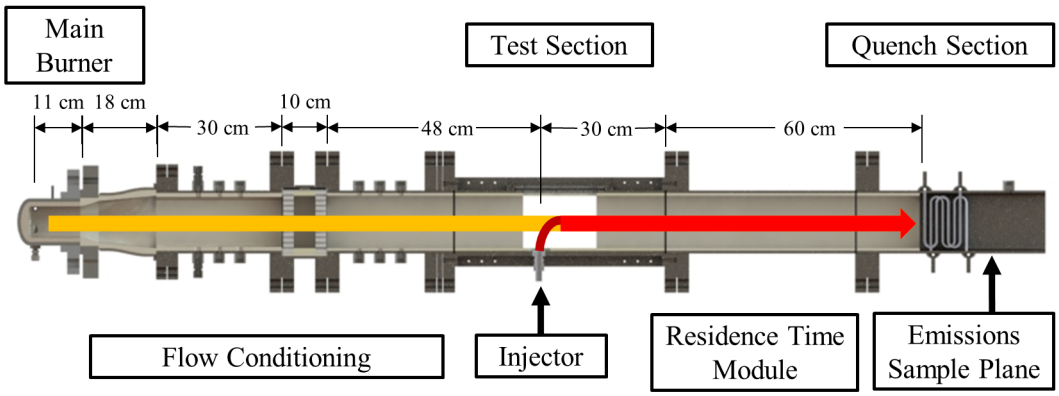

Figure 25 – Schematic of experimental as used for preliminary investigation.

A premixed natural gas/air mixture, preheated to 591K (±5K) to enable stable operation at lean equivalence ratios of approximately 0.5, is combusted in the main burner. The reactants are metered with sub-critical orifices and injected tangentially into a 76 mm diameter circular section via four ports with exit diameters of 11 mm. The main burner stoichiometry was adjusted in order to vary the approach flow temperature to the RJICF and demonstrated stable operation across the entire range of test conditions. The vitiated flow then passes through a flow conditioning section, which consists of a 18 cm long circular to rectangular cross-section transition piece followed by a 30 cm (3.7 channel hydraulic diameters) settling chamber, two ceramic honeycomb flow straighteners (separated by 10cm), and a second 30 cm settling chamber in sequence. The honeycomb flow straighteners are 25 mm thick Mullite Versagrid units comprised of 6.35 mm by 6.35 mm passages. The test section includes optical access (sides and top) and the secondary injection jet. The test section cross-section is 63.5 mm wide by 114 mm tall. This cross-

section initiates immediately after the second flow straightener 48 cm upstream of the jet exit plane. The jet is injected via a 12 mm inner diameter stainless steel tube flush with the ceramic lining of the test section floor. The jet delivered preheated and premixed methane/air mixtures metered using critical orifices. Jet preheat temperatures ranged from 420 – 460K, enabling autoignition of the jet in the vitiated crossflow. The injection tube is straight for 40 diameters prior to the jet exit to ensure fully developed exit flow profile [55], and mixing of the fuel and air flows occurring approximately 100 diameters prior to the jet exit. The jet Reynolds number ranged from 3900 – 7000, and the jet mass flow averaged less than 5% of total mass flow, with a maximum of 6.5%.

The facility delivered a vitiated crossflow of natural gas/air combustion products at equivalence ratios ranging from 0.50 to 0.65 at a fixed average velocity of 17.3 m/s, calculated from the measured temperature and mass flow rate. Corresponding test section temperatures ranged from 1650 – 1810K and cross flow Reynolds numbers from 4375 - 4800 based on a hydraulic diameter of 8.16 cm. The test section temperature was estimated via spectroscopic measurement of the irradiance of a ceramic shielded type R thermocouple installed in place of the jet 3 cm above the jet exit.

After the remaining 30 cm of the test section post-injection and a 45 cm long residence time module, the hot gases enter the NOx measurement section. Because of the highly non-uniform NOx and flow velocity profiles (which implies that simply mapping out spatial NOx values is insufficient, as NOx fluxes can also vary spatially), the flow is

cooled to freeze NOx formation, then mixed, then measured. This quench section consists of a 15 cm ceramic lined entrance section followed by 15cm of pressurized water filled radiator tube banks. The tube banks are made up of two sets of six tubes shaped as indicated in Figure 25 and set opposite each other. Each of the two banks is fed by a manifold that is itself supplied at the sides and top. The waste water is expelled into a similar manifold. The quench section was verified to reduce the gas flow temperature to less than 700K. A reference τ_{res} post jet injection can be calculated using a reference velocity and the 90 cm distance between the jet exit centerline and quench radiator banks. In designing the test matrix, two possible reference velocities were considered: the average velocity of the crossflow (~17.3 m/s), or one based upon the main and jet mass flow rates and the average gas temperature after combustion of the RJICF. The former was used, which leads to a reference τ_{res} of 51 – 53 ms for all tests reported here. The components and methodology used for NOx sampling and measurement are described in more detail in Section 4.3.1.

4.1.2 Test Facility Configuration for Primary Emissions Investigation

A schematic of the facility as used to investigate the emissions of the parameter space described in Section 4.2.2 is provided by Figure 26. The experimental facility consists of a main burner to generate a high-temperature cross flow, a flow conditioning section, an optically accessible RJICF section, a residence time module, a quench section, and an emissions sampling system.

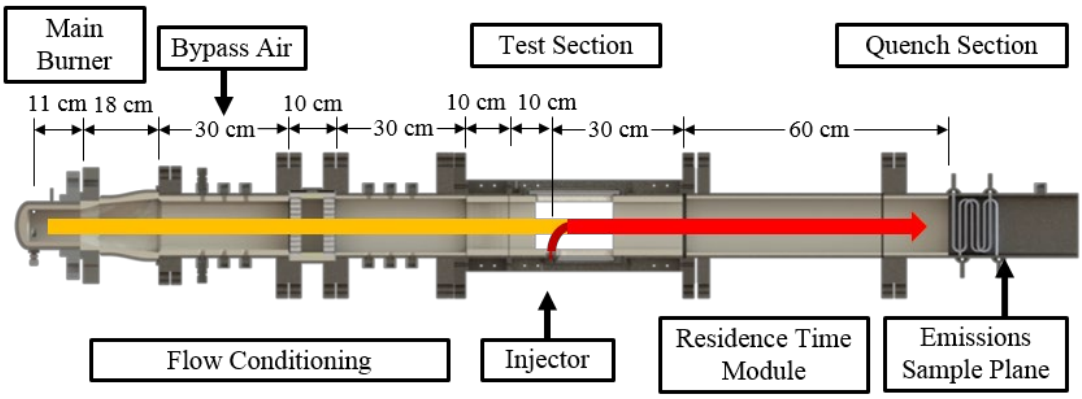

Figure 26 – Schematic of experimental facility as used in primary investigation.

As noted, the primary components of the facility were described previously in Section 4.1.1 and therefore attention will be given to any modifications made to the facility described in Section 4.1.1. The swirling main burner was stably operated at either an equivalence ratio of 0.5 or 0.55. The combined uncertainty and temporal variation in this equivalence ratio was less than 3%. This main burner was supplied with preheated reactants at 590K (±5K). The crossflow then passes through the flow conditioning section as described in Section 4.1.1 to remove the swirl and produce a more uniform crossflow for the secondary injection. In the configuration presented in Figure 26, bypass air was injected into the crossflow as part of the flow conditioning section. The intent of this modification was to provide the means to seed the crossflow with ceramic particles for velocimetry if necessary. After dilution, the effective equivalence ratio of the vitiated crossflow (ϕ_{XF}) is equal to 0.45 or 0.5, with an uncertainty (including temporal variation) of less than 3%. These two crossflow conditions provided two distinct crossflow temperatures of 1350K and 1410K, in order to assess the impact of crossflow temperature on *LO* and NOx

emissions. The temperatures were calculated as follows. A bulk flow density was calculated from metered flow rates and measured bulk flow velocity of the crossflow within the test section (measurement method described subsequently in this section and detailed in Section 4.3.3). This bulk flow density was compared to results from an adiabatic flame calculation to determine the relationship of the bulk crossflow temperature relative to adiabatic flame temperature. The associated Reynolds numbers for each of these two crossflow conditions, based on a hydraulic diameter of 5.70 cm, are 6270 and 6750.

The test section itself is the most significant change to the facility from previous studies. It incorporates a transition section equipped with a contoured (fifth order polynomial curves) ceramic lining to reduce the channel width from 63.5 mm to 38 mm[1]. The reduced width results in a test section cross section of 38 mm x 114 mm and an average flow velocity of 25.8 m/s. The crossflow velocity through the test section was characterized using Laser Doppler Velocimetry (LDV). The system and its implementation is discussed in more detail in Section 4.3.3, and plots of the resulting measurements can be found in Appendix A.1. The test section also incorporates four sided optical access (side and top/bottom) as well as the secondary injection jet.

Two different jet configurations were used in order to explore the limiting cases of fully developed and top-hat jet exit velocity profiles. As will be seen, these two velocity

[1] This width reduction is responsible for the change in hydraulic diameter compared to that reported in Section 2.1.1.

profiles have quite different shear layer growth rates and NOx emissions. The first configuration utilizes a 6mm inner diameter stainless steel tube set flush with the ceramic lining of the test section floor. The tube is straight for 80 diameters prior to the jet exit, sufficient to achieve a fully developed turbulent profile [55]. The second geometry utilizes a contoured ceramic nozzle with a 24 mm and 6 mm entrance and exit diameter respectively; i.e., a factor of 16 area reduction. This significantly reduces the boundary layer thickness at the jet exit. A significant body of work [19, 56-58] utilizing nozzles with similar area reduction and shaped with the same fifth order polynomial have characterized the momentum thickness of the configuration (assessed at a height of $0.1d_j$ above the jet exit) to be between $0.05d_j$ and $0.1d_j$ [59] for the J values investigated here.

In both cases, the jet fluid was premixed and consisted of preheated ethane/air or ethane/methane/air mixtures. The fuel and air are mixed approximately 200 diameters prior to the point of injection to ensure fully premixed jet fluid. The preheat temperature of the jet fluid ranged from 460 – 500K. The Reynolds number of the jet, based on jet diameter, ranged from $6.60\text{x}10^3$ – $18.3\text{x}10^3$. The mass flow of jet never exceeded 8% of the total mass flow, averaging about 5%. The mass flows of all constituent species were metered using critical orifices.

After injection of the jet into the crossflow, the exhaust flow path is identical to that described in Section 4.1.1; no changes were made through the remainder of the test section,

followed by the “residence time module”, and finally through the “quench section” (detailed in Section 4.1.1).

4.1.3 Test Facility Configuration for Primary Pre-flame Mixing Investigation

In order to conduct Mie scattering imaging of the pre-flame mixing as described in Section 0, the facility was further modified from the configuration presented in Section 4.1.2. A schematic of the facility as used in the Mie scattering investigation for the primary parameter space presented in Section 4.2.2 is shown in Figure 27.

The facility was operated identically as described in Section 4.1.2, with the exception of the removal of the quench section and NOx measurement system. This was done so as to not contaminate this hardware and instrumentation with seed particles. After injection of the jet into the crossflow, the exhaust gases flow through the remainder of the test section as well as the residence time module. Following this section, the flow is vented to the laboratory exhaust system.

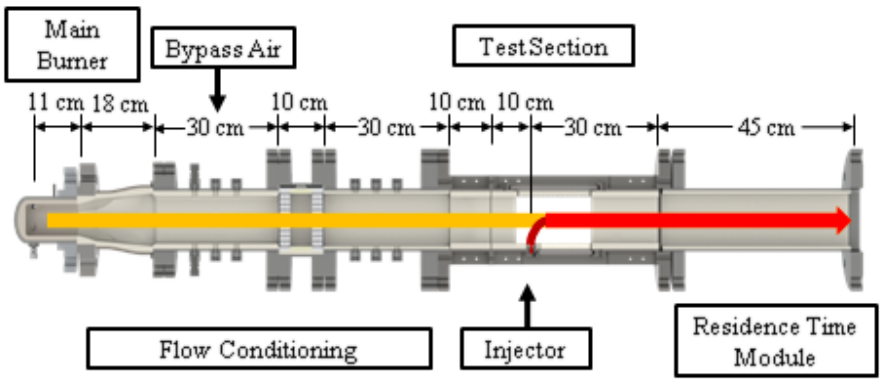

Figure 27 – Schematic of experimental facility as used in pre-flame mixing investigation.

4.2 Design of Experiments

This section describes the design of experiments and the test matrices utilized in conjunction with the various facility configurations described in Section 4.1. The pairings of test matrix and facility configuration are Section 4.2.1 with Section 4.1.1 and Section 4.2.2 with Section 4.1.2 as well as Section 4.1.3.

4.2.1 Parameter Space for Preliminary Investigation

The test matrix for the preliminary investigation was designed to look at the NOx sensitivity to different fractions of heat release in the axial stage versus the main burner. It was also developed to investigate the differences in NOx between achieving a given ΔT across the axial stage with jets of differing J and equivalence ratio in order to provide some insight into the most beneficial manner, from an emissions standpoint, in providing

premixed fuel in an axial staged combustor. The rest of this section describes the test matrix development approach.

The equivalence ratio of the main burner was varied to create values of ϕ_{XF} = 0.5 – 0.65 in increments of 0.025. The crossflow velocity was held nearly constant (u_∞ = 17.1 – 17.7 m/s) between all cases by reducing the mass flow rate with increasing equivalence ratio to account for higher flow temperatures, which allowed ϕ_{XF} to independently control crossflow temperature; the approach-flow temperature has significant effects on flame lift-off height, as described later. For each crossflow condition a range of final system equivalence ratios (ϕ_{Global}) were targeted. The test section temperature data was utilized to ensure that several of the ϕ_{Global} values resulted in equal exhaust temperatures across crossflow conditions.

Once the crossflow conditions were fixed and the target system equivalence ratio was chosen, the jet conditions were then iterated by changing *J* and the jet equivalence ratio (ϕ_{jet}). The target *J* ratios were chosen in the range of 2 to 5 to ensure that the jet stays within the confines of the viewable region of the test section. The associated value of ϕ_{jet} for each test point was derived based on ϕ_{Global}, ϕ_{XF}, and *J* constraints. This created an interdependent relationship between *J* and ϕ_{jet}, with ϕ_{jet} being driven down as *J* increases.

4.2.2 Parameter Space for Primary Investigation

The aim of the test matrix for this work was to include jets over a broad range of J and ϕ_{jet} values, at discrete levels of ΔT, and varying exit velocity profiles and crossflow temperatures. The test point selection methodology was a follows.

The test matrix targeted four intervals of ΔT: 75K, 150K, 225K, and 350K. Each of these ΔT values were obtained for six J values of 6, 8, 10, 15, 20, and 40. This J range sweeps the transition from globally to convectively unstable in nonreacting JICF [15]. This matrix of 24 points was repeated at two crossflow conditions, where ϕ_{XF} is set to 0.45 or 0.5 respectively. The crossflow velocity was held nearly constant at 25.8 m/s (±3.5%) across both crossflow conditions by adjusting the mass flow to account for the different crossflow temperatures. Thus, the two crossflow conditions create two vitiated flows of equal velocity but differing temperature. Utilizing the measured crossflow conditions and adiabatic flame temperatures for the secondary combustion zone, a target final system equivalence ratio (ϕ_{Global}) was calculated for each ΔT. With ϕ_{XF}, ϕ_{Global}, and J now fixed, the necessary ϕ_{jet} value for each data point was calculated. This method, again, creates an interdependency on J and ϕ_{jet}, with ϕ_{jet} decreasing as J is increased for a given selection of ΔT and ϕ_{XF}. The entirety of the matrix was repeated for each of the two jet exit velocity profiles. The parameter space associated with these ethane-fueled tests consisted of 6 (J) x 4 (ΔT) x 2 (ϕ_{XF}) x 2 (jet velocity profiles) = 96 points.

Additional data points were taken to decouple LO from stoichiometry and J values, with mixtures of ethane and methane. Methane addition increases autoignition delays

compared to ethane and was observed to increase *LO* values for these crossflow test conditions. Reactor modeling conducted with CHEMKIN indicated that mixing in methane into the jet fuel stream could increase autoignition delay with only a change in adiabatic flame temperature on the order of 20K or less. The resulting methane composition of these points ranged from 40 – 55% of the jet fuel mass. Again, each combination of ΔT and J for these replicated points was conducted at each crossflow condition and jet exit velocity profile. Two ΔT values were selected thereby adding an additional 48 test points to the matrix, bring the total interrogated conditions to 144.

4.3 Diagnostics and Measurement Techniques

4.3.1 Gas Sampling and Emissions Measurement

Emissions sampling was conducted using a slotted probe located 12.5 mm after the section of radiator tube banks. The slotted probe intakes gas through a 1.6 mm wide and 120 mm tall slot in order to simultaneously sample the entire vertical span. The spatial variation of NO was mapped out in a 4 by 3 grid with single point measurements taken at the center of each 30 mm wide by 35 mm tall box for a several jet configurations similar to those in the test matrix. The spatial variation of NO measurements in the direction transverse to the slotted probe was less than 1 ppm (corresponding to less than 15% of average for each vertical position). Gas collected by the probe is funneled into a 7.75 inner diameter tube which connects the probe to the gas analyzer. Gas samples were analyzed by a Horiba PG-350 gas analyzer which uses a cross-flow modulation chemiluminescence detection method to measure NOx (NO and NO2 in this instance) at a rate of 1 Hz. After a steady state was achieved for each reacting jet condition, emissions data was collected for two to three minutes.[2] All reported NOx data is based on an average of the collected data for each test condition.

The total NOx produced by the test rig is a function of that produced by the vitiated crossflow and the reacting jet. In order to assess the NOx production of the jet, baseline

[2] Results from test matrix described in Section 2.2.1 used two minute average and results from test matrix described in Section 2.2.2 used three minute average.

NOx levels were obtained. These measurements were obtained by emissions sampling of the crossflow conditions without any mass flow from the secondary injector. Consequently, the reacting jet NOx contribution (ΔNOx), calculated by subtracting the baseline NOx from the test point NOx level, serves as a measure for the complete impact of the jet on the NOx level.

4.3.2 Flame Chemiluminescence Imaging

Images of flame chemiluminescence emissions were obtained from side-on imaging using an intensified high speed camera at either 2000 or 5000 frames per second (fps) dependent upon the test campaign. To capture CH* chemiluminescence (with contributions from CO_2*), a combination of a single-band bandpass filter and a long wave pass filter were used. The Semrock BrightLine bandpass filter had a center wavelength of 434 nm with a bandwidth of 17 nm and the Semrock EdgeBasic long wave pass filter had an edge wavelength of 364 nm.[3] CH* is a commonly used heat release marker for hydrocarbon flames [23-25, 30]. For comparison with the CH* images, comparable high speed OH* chemiluminescence was simultaneously obtained for certain cases through a single-band bandpass filter with a center wavelength of 320 nm and a bandwidth of 40 nm. The equipment and acquisition rate details for each measurement campaign are presented in Table 2.

[3] The bandpass filter had significant transmission levels in near infrared spectrum. This prompted the use of the long wave pass filter due to its reduced transmission profile in the near infrared.

Table 2 – Equipment details for chemiluminescence imaging

Test Matrix	Species / Subset	Camera	Intensifier	fps
Section 4.2.1	CH* / All	Photron Fastcam SA-1	Lambert HiCATT	2000
Section 4.2.2	CH* / Pipe Geometry: Emissions	Photron Fastcam SA-1	LaVision IRO	5000
Section 4.2.2	CH* / Pipe Geometry: Mie Scattering	Photron Fastcam SA-1	LaVision IRO	5000
Section 4.2.2	OH* / Nozzle Geometry: Emissions	Photron Fastcam SA-1	Lambert HiCATT	5000
Section 4.2.2	CH* / Nozzle Geometry: Emissions	Photron Fastcam SA-Z	Lambert HiCATT	5000
Section 4.2.2	CH* / Nozzle Geometry: Mie Scattering	Photron Fastcam SA-Z	Lambert HiCATT	5000

4.3.3 Laser Doppler Velocimetry

As mentioned in Section 4.1.2, the crossflow velocity through the test section was measured using LDV. The system consists of an Innova 90C-6 Argon Ion laser system to generate a multiline beam with a wavelength range from 457.9 to 514.5 nm. This multi-wavelength beam then passes through a Bragg cell operating at 40 MHz to create two beams, with the second frequency shifted compared to the first. A pair of prisms is used to separate two pairs of beams (with each pair including a frequency shifted component). The wavelength of the pairs were nominally 488nm and 514.5nm. The beam pairs are then coupled to optical fibers connected to a transceiver unit. The transceiver unit contains a lens with a focal length of 363mm to create a 3.74μm fringe spacing. Aluminum oxide

(Al_2O_3) particles with a nominal diameter of 5 μm were injected via the bypass air circuit into both the top and bottom of the flow conditioning channel in order to seed the crossflow. The flow velocity was measured at six discrete intervals above the center of the jet exit at heights ranging from 6 – 50 % of the test section height. The location of each interrogation point is given in Table 3. The scattered light from the seeded flow is collected by the transceiver and focused onto a photomultiplier. A photodetector module (PDM) then reads the transduced light signal and controls the gain for the measurement to be analyzed by the frequency size analyzer (FSA) digital signal processor. The processed signal is passed through an 80 MHz low pass filter, after which it is downmixed by a specified frequency, and then finally passed through a bandpass to remove outlying frequencies and noise.

Table 3 – Interrogation locations for laser Doppler velocimetry of crossflow

Interrogation Point	Height (mm)	Normalized Height
1	7	0.06
2	12	0.105
3	17	0.15
4	27	0.23
5	37	0.32
6	57	0.5

4.3.4 Mie Scattering

The jet was seeded with 0.3 – 1 micron TiO_2 particles that were used for Mie scattering imaging. As discussed Section 4.4.2, the spatial density of these particles was used to assess local mixture fraction and to quantify pre-flame mixing levels. A frequency doubled ND:YLF laser was used to produce a 5 kHz pulse train of 527 nm pulses in order to illuminate the particles. The beam was formed into a sheet 63.5 mm wide and 2 mm thick. The laser sheet was passed through the test section from above (shown in Figure 28), entering through the top window and impinging upon the test section floor, with a portion of it exiting through the bottom window. The center of the beam width was aligned with the center plane of the test section floor. The resultant field of interrogation was 60 mm x 60 mm, initiating 1 mm upstream of the jet exit.

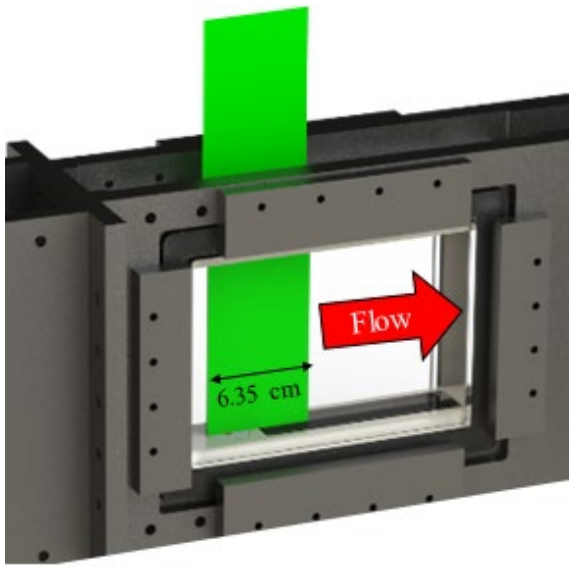

Figure 28 – Mie scattering illumination beam path through test section.

The illuminated particles were imaged with a high speed camera at 5000 fps, using bandpass filter with a center wavelength of 527 nm and a bandwidth of 20 nm

4.4 Image Processing

4.4.1 Chemiluminescence Images

The instantaneous and time averaged chemiluminescence images were analyzed to determine the spatial flame structure. Of particular interest was the degree of flame lifting, which strongly influences pre-flame mixing. Flame structure was assessed via analysis of a time averaged flame probability density map developed from the instantaneous chemiluminescence images. The processes for creating the flame probability map is described here.

The raw images were normalized and filtered using a guided image filter [60] to remove most of the noise. An example instantaneous raw image for a given case is shown on the left of Figure 29. The filtered image is then binarized by using a threshold based on Otsu's method [61] (which does not require an arbitrary threshold), see center pane of Figure 29. The binarized instantaneous images were then averaged to create a probability field of the flame existing at that location, an example of which is shown in the right panel of Figure 29. The flame probability maps from the testing described in Section 4.2.1 were built from 909 images for each test condition, and the flame maps from the testing described in Section 4.2.2 were built from 2500 images.

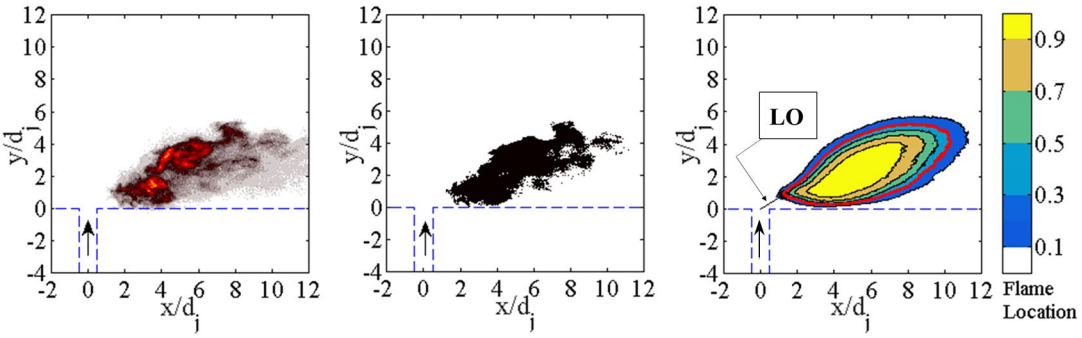

Figure 29 – Raw (left), binarized (center) flame images, and probability density field of flame position (right) with 0.3 contour corresponding to *LO* highlighted in red. Images from test case with ϕ_{XF} = 0.60, ϕ_{Jet} = 1.40, and *J* = 1.56.

LO was defined as the minimum distance between the center of the jet exit and the 0.3 contour (highlighted in red in right pane of Figure 29) of the flame probability map. The CH* results were used for the purpose of this analysis. No significant difference was observed for *LO* values obtained from CH* and OH*.

For the portion of the work associated with pre-flame mixing rates presented in Section 5.3, the position of the leading edge of the flame image was of particular interest; it was used to approximate the mixture fraction at the flame. The leading edge was extracted at each instant by identifying a boundary around the line of sight flame image. The maximum and minimum vertical position were identified and the front edge of the boundary between the top and bottom points was extracted as the flame leading edge. Figure 30 shows a sample binary flame image with top and bottom points identified and flame edge extracted.

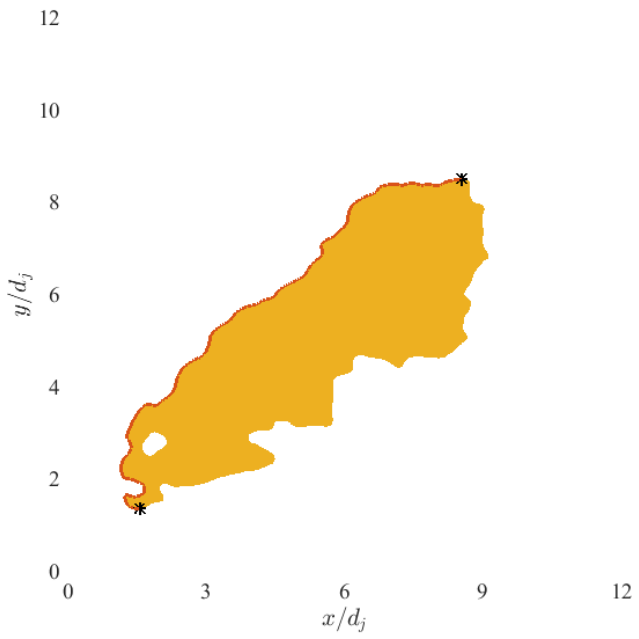

Figure 30 – Illustration of flame edge extraction methodology. The solid region denotes the binary flame chemiluminescence, and the solid line denotes the front edge of the flame.

4.4.2 Mie Scattering Images

The Mie scattering images were background subtracted with a 15 image sliding minimum to remove reflections from the test section floor and side windows. The image was then thresholded using a technique similar to the chemiluminescence images (Section 4.4.1) to remove contributions from out of focus/plane particles and trace amounts of other luminosity. The resultant image was binarized and passed through a 9x9 box filter. This reduces the field's spatial resolution but assigns a value proportional to the area (in pixels) that is illuminated inside the binned region, i.e. the illuminated area. Another consequence

of using the box filter is the discretization of the measurement into 81 intervals. The illuminated area values are then normalized in reference to the jet core, immediately at the jet exit, where the mixture fraction is known; this normalized illuminated area value is defined as Θ. Figure 31 shows a sample Mie scattering image through this process.

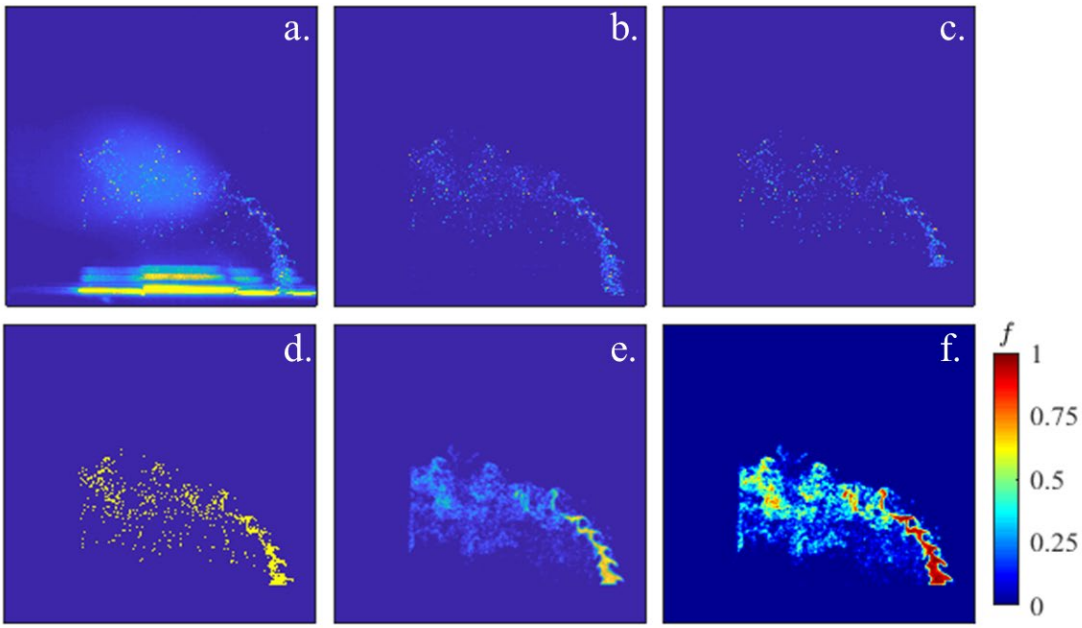

Figure 31 – Sequence of mie scattering image processing; shown is raw image (a), sliding minimum subtracted (b), thresholded (c), binarized (d), binned to generate normalized particle illuminated area field (e), and transformed to mixture fraction field (f).

The next step of the process is the conversion of the normalized illuminated area (Θ), shown in Figure 31e, to mixture fraction, shown in Figure 31f. Similar efforts to derive mixture fraction or other scalar concentrations from Mie scattering has been conducted

previously [62, 63] and validated against the well understood behavior of a free jet. The approach described next is similar to Sautet & Stepowski [63], but generalizes their work to account for temperature differences between the fluid streams. Its key assumptions are that (i) particles follow the flow, and (ii) mixing of sensible enthalpy and mass occurs at the same rate. This procedure and these assumptions are discussed next.

First, the relationship between Θ and the seed particle number density will be discussed. Depending upon the scale comparison of the wavelength of incident light (λ) to the diameter of the seed particle (d_p), the scattered light intensity varies from being proportional to the volume of the seed in the Rayleigh limit ($d_p/\lambda << 1$), or proportional to the cross-sectional area of the particle when $d_p/\lambda >> 1$. In the case of the presented data, where 0.3 – 1 μm diameter particles and 532 nm incident light make $d_p/\lambda \approx 1$, the intensity of light is proportional to the Rayleigh cross-section, which accounts for the refractive properties of the material. It is critical to note that due to particles being identified in a binary fashion (Figure 31d), the data presented do not have a dependence on the intensity of the scattered light. The exception to this statement is the threshold level. Due to variations in seed particle size, laser sheet intensity, and shot-to-shot intensity, the threshold value does not represent a constant value of Θ across all images and test points. This impacts the lowest values of f that are identified in each image. However, low values of f are associated with low flame temperatures in these experiments. As discussed in Section 1.1, thermal NO production is exponentially dependent on temperature. Therefore, thermal NO production is insensitive to small changes in temperature, when that

temperature is below a certain critical value. As the *f* values that are impacted by the varying threshold are associated with flame temperatures below this critical value, this effect is neglected.

The impact of variation in light intensity was minimized by using binary images to determine Θ, as discussed above. However, the size of each particle (in pixels) is of critical importance. For most optical applications, the size of an image is proportional to the size of the object through a magnification factor. However, below a certain limit the object size has no correlation on the image size. This is defined as diffraction limited. Using Equations 2.7 and 2.8 from Raffel *et al.* [64] it is clear that in the data reported here, the images size is governed by the diffraction limited minimum image diameter. The implications of this is that the illuminated area discussed above is proportional to the number of particles in each 9x9 bin and not their projected areas. By extension it follows that Θ is therefore proportional to the local particle number density normalized by the jet core value.

It is important to note an additional source of uncertainty associated with this methodology. As described, the method for determining the mixture fraction is dependent on the diffraction limited nature of the imaging. This opens the possibility for multiple small particles in close proximity to appear identical to a single particle on the image. This effect will have the most impact on identification of the core region. If the core region is inaccurately identified the entire mixture fraction field is biased towards higher values of *f*. Depending on the magnitude of this bias it could have significant consequences such as

indicating a flame is burning fuel rich when in fact it is fuel lean but near stoichiometric. These two conditions have significantly different thermal NO production rates due to [O]. It is critical, therefore, to compare the potential core lengths acquired from this method with literature to gain insight into the magnitude of any bias and the validity of the measurement.

The method for transforming Θ into *f* is now addressed. This section has established that, subject to several assumptions, Θ is proportional to seed number density. This number density can be impacted (prior to the flame) by two mechanisms: mass exchange and thermal expansion. Due to the temperature disparity between the jet and the crossflow, mixing of the jet with the crossflow will reduce Θ by both mechanisms, and their impact must be accounted for simultaneously. Therefore the following expression relates the local values of Θ to these mechanisms:

$$\Theta = \frac{T_j}{T}\frac{N_j}{N_{tot}} \tag{10}$$

where T is the local temperature, T_j is the temperature of the jet core, and N_j/N_{tot} is the local mole fraction of jet fluid. N_j/N_{tot} relates to the mixture fraction as:

$$f = \frac{m_j}{m_{tot}} = \frac{MW_j}{\overline{MW}}\frac{N_j}{N_{tot}} \xrightarrow{yields} \frac{N_j}{N_{tot}} = \frac{\overline{MW}}{MW_j} f \tag{11}$$

where m_j/m_{tot} is the local mass fraction of jet fluid, MW_j is the jet fluid molecular weight and $\overline{MW}$ is the mixture molecular weight. Substituting Equation 11 into Equation 10 yields the following relation between *f* and Θ:

$$\Theta = \frac{T_j}{T}\frac{\overline{MW}}{MW_j} f \xrightarrow{yields} f = \frac{T}{T_j}\frac{MW_j}{\overline{MW}}\Theta \tag{12}$$

The local temperature (based on an assumption of uniform specific heat) and molecular weight are themselves functions of *f* given by Equations 13 and 14:

$$T = fT_j + (1-f)T_{XF} \tag{13}$$

$$\overline{MW} = fMW_j + (1-f)MW_{XF} \tag{14}$$

where T_{XF} and MW_{XF} are the temperature and molecular weight of the crossflow. Combining Equations 12 – 14 gives a quadratic formula in terms of the measured fluid properties and Θ which can be solved for *f:*

$$\left(1 + {MW_{XF}}/{MW_j}\right) f^2 + \left[{MW_{XF}}/{MW_j} + \Theta\left({T_{XF}}/{T_j} - 1\right)\right] f - {T_{XF}}/{T_j}\,\Theta = 0 \tag{15}$$

The presented method is invalid in the near vicinity of the flame as another source of temperature increase/sensible enthalpy addition is present. The mixture fraction of the flame is thereby assessed by using an expected value that is compiled from instances when the flame is not present in this location. A time-averaged mixture fraction field is compiled from 2500 images for each data point. Only data that is at least 12 pixels (≈ 1 mm) upstream of the flame in each instantaneous mixture fraction field contributes to the average. This interval insures that no 9x9 bin in which the flame is present contributes to the time average. In addition, if the flame position is dependent on mixture fraction, then the used expected value does not capture this cross-correlation. Consequently, the flame is, in essence, being characterized by the mixture fraction of the flow preceding it. This is done out of necessity as, once again, this methodology is invalid at the flame. This effect reinforces the necessity of comparison between the pre-flame flow fields and JICF literature in order to establish confidence in the data.

4.4.3 Flame Edge NO Production Rates

The time averaged mixture fraction fields are in turn used to calculate NO production rates that are meant to simultaneously capture the multiple impacts that varying ϕ_{Flame} would have on NOx production; i.e. via T_{Flame}, [O] (or [O2]), and [N2]. For the presented data, NO production rates were calculated at each location along each flame edge. An average NO production rate for the test point was obtained for comparison to the measured emissions by averaging over all valid locations of all instantaneous flame edges.

The NO production rate for a specific location is a function of the data point ϕ_{jet} and the local mixture fraction. As *f* at the flame in each instance is not possible to determine with the method described in Section 4.4.2, the local mixture fraction is determined by superposition of the instantaneous flame edge on the expected mixture fraction field. Contributions from locations associated with a mixture fraction average that is comprised of less than 100 samples are discarded. The composition of the reacting mixture is a function of ϕ_{jet} and *f* and serve as parameters for a series of tabulated CHEMKIN equilibrium calculations. Values for *T,* $[O_2]$, and $[N_2]$ are extracted from the tabulated results for the specific mixture created from ϕ_{jet} and *f*. The local NO production rate is then calculated based on the following expression[4] from Bowman [6], which is an extension of Equation 4 that also utilizes partial equilibrium assumptions to substitute $[O_2]$ for [O]:

$$\frac{d[NO]}{dt} = 1.45x10^{17}T^{-1/2}[O_2]^{1/2}[N_2]e^{-69{,}460/T} \tag{16}$$

To highlight the sensitivity of NO production rate to the local mixture fraction, Figure 32 plots *d[NO]/dt* as a function of *f* for three different values of ϕ_{jet}.

[4] The units for *d[NO]/dt* in this expression are in mol/cc*s. The data is presented in ppm/ms.

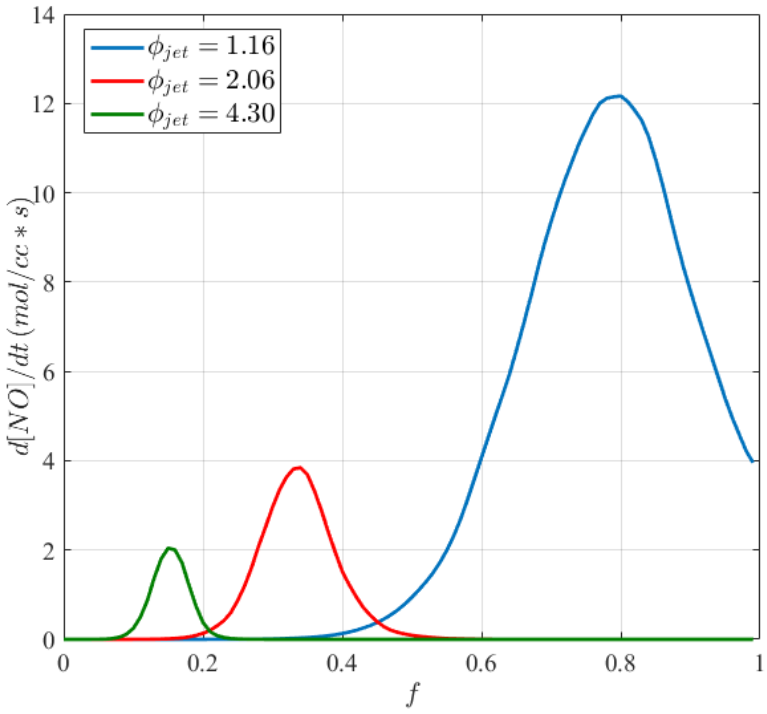

Figure 32 – NO production rates as a function of mixture fraction for select jet equivalence ratios.

4.5 Uncertainty Characterization

4.5.1 Uncertainty in Fluid Flow Rates

The metering system of the facility was very similar to that used for previous experimental investigations such as that conducted by Wilde [54]. In this work, Wilde extensively characterized the uncertainty of both the sub-critical orifice and critical orifice flow metering systems of the facility. The uncertainty in sub-critical flow systems, which include the main burner air and fuel flows, was evaluated as 1.79% of the flow

measurement. The error in critical orifice flow metering, which include all jet fluid as well as the crossflow bypass air, was evaluated at 1.67% of the flow measurement.

4.5.2 Uncertainty in NOx Emissions

The Horiba PG-350 gas analyser measures NOx with a repeatability of ±1.0%, linearity of ±2.0%, and drift of ±1.0% per day referenced to the measurement range utilized. The majority of the data utilized a NOx measurement range of 0 – 25 ppm. The Horiba was calibrated at the onset of every day of data collection with calibration points at 0 and approximately 22 ppm. As a result the drift was only taken to be ±0.5% and linearity is neglected for data in the vicinity of the calibration nodes.

All NOx data reported in this report is corrected to 15% O_2. As such, the error in O_2 concentration measurement contributes to the uncertainty in reported NOx. However, the resultant O_2 measurements from the tested system equivalence ratios were all in close proximity to the O_2 calibration node. Therefore, the linearity contribution from O_2 was neglected except for high ΔT test series, where O_2 levels were significantly different than the calibration node.

The uncertainty in the normalized NOx metric introduced in Section 5.2.2.1, contains contributions from the uncertainty in the measurement of the two jet fuel stream mass flow rates in addition to the NOx measurements. The uncertainty of the flow rates is

addressed in Section 4.5.1. The resultant uncertainty is indicated on the relevant plots for each data point.

4.5.3 Uncertainty in Particle Tracing of the Flow

As noted in Section 4.4.2, a key assumption of the approach of using the Mie scattering images to determine mixture fraction is that the particle seed follow the fluid flow. A key parameter in assessing the validity of this assumption is the Stokes number (Stk). Stk is a ratio of a particle response timescale (t_p) to a flow timescale (based on a flow scale of interest). High fidelity of flow tracing by the particle exists for Stk << 1, but in practice Stk < 0.1 provides tracing accuracy of less than 1% and is deemed negligible [65]. Two flow time scales will be used for comparison. As this analysis is focused on utilizing time average pre-flame mixing, a flow time scale associated with bulk fluid motion (t_∞) will first be considered. As the jet penetration is on the order of half the channel height, this will be the length scale used to calculate a bulk flow time scale. This yields $t_\infty = (\frac{1}{2}h)/u_j$. The highest J value in the investigated parameter space is 40, which combined with the fact that all of the jet density ratios where at 3 or slightly above gives a maximum potential bulk jet velocity of approximately 100 m/s. Combined with the 144 mm channel height yields t_∞ = 570 μs. The second flow time scale will be utilized to assess fluid motion related to the shear between the jet and crossflow and will use the jet radius as its length scale, yielding $t_j = (\frac{1}{2}d_j)/u_j$. The 6mm jet diameter combined with the maximum potential bulk velocity yields t_j = 30 μs.

Under Stokesian flow (i.e. creep flow), a particle response time (t_p) can be calculated with $t_p = \rho_p d_p^2/18\mu_g$, where ρ_p is the density of the particle ($\rho_p \approx 4$ g/cm^3 for TiO_2), d_p is the particle diameter, and μ_g is the gas dynamic viscosity. In order to check the validity of the assumption that the particle is experiencing Stokesian flow, the Reynolds number of the fluid flow over the particle must be considered. Reynolds number of the particle (Re_p) is given by: $Re_p = u_p d_p/\nu_g$, where u_p is the magnitude of the velocity of the flow over the particle, in other words the relative velocity of the particle compared to the flow, and ν_g is the kinematic viscosity of the gas. The gas kinematic viscosity will be lowest in the jet compared to the cross-section mainly due to the disparity in temperature. As even for the richest jets the jet fluid is still at least 70% air, the ν_g equal to that of air at 460K will be used in this analysis ($\approx 3\text{x}10^{-5}$ m/s^2). Using the quoted value of ν_g, the upper limit of the particle diameter range (1 μm), and the maximum bulk jet velocity to create a very conservative estimate yields $Re_p = 3.33$. At this very conservative estimate, Re_p is still O(1), and it is apparent for any realistic value of relative particle velocity that Re_p will be below unity, validating Stokesian assumptions.

Returning to the particle response time, using the dynamic viscosity of air at 460K makes for a conservative estimate of $t_p = 8.25$ μs. This particle response time yields Stokes numbers of $Stk_\infty = 0.014$ and $Stk_j = 0.275$. Based on these estimates of Stokes number it is clear that very little error is associated with the tracing of the particles for

the bulk flow which is the focus of the work. However, it is also evident that the error in tracing the smaller scale fluid motion is significant and greater than 1%. It is worth noting however that this flow time scale equates to flow fluctuations on the order of 30 kHz, which the sampling frequency of 5 kHz is unable to resolve. This analysis demonstrates that the acquired data is adequate for its intended purpose of assessing time averaged pre-flame mixing.

CHAPTER 5. EXPERIMENTAL RESULTS

5.1 Nitrogen Oxide Sensitivites of Rich Premixed Reacting Jets with Low Momentum Flux

This section discusses the data obtained in the investigations detailed in Section 4.2.1. The discussion focuses on the sensitivity of flame lift-off distance to ϕ_{XF}, J, and ϕ_{jet}. Subsequently, the sensitivity of NOx emissions of these rich premixed methane/air jets to ϕ_{XF}, J, ϕ_{jet}, and LO is also assessed.

5.1.1 Liftoff Analysis of Rich Premixed Methane Jets

For all conditions reported in this chapter, the flame initiates on the leeward side of the jet. The observed RJICF flames present with a highly lifted windward branch to the point that they are deemed as lee-stabilized flames (defined in Section 1.3.2), or as fully lifted flames. This behavior is shown by the representative flame images in Figure 33.

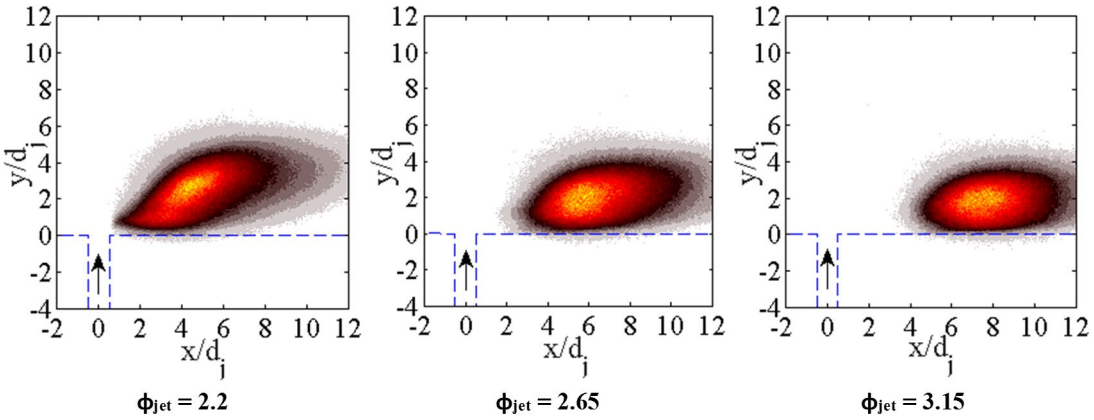

Figure 33 – Characteristic time averaged flame images. Images from test cases with constant crossflow conditions of ϕ_{XF} = 0.6.

Figure 34 summarizes the results for *LO* as a function ϕ_{jet}, at a constant target exhaust temperature of 1956K. Also indicated on the figure are contours of constant crossflow conditions (in the form of ϕ_{XF}), and *J*. First, Figure 34 indicates a clear sensitivity of *LO* to cross flow temperature; i.e., increasing ϕ_{XF} results in a reduction of *LO,* as expected. At constant crossflow conditions (constant ϕ_{XF} contour), *LO* increases with increasing ϕ_{jet}. Kolb *et al* [32] similarly demonstrated that flame lift-off height is a strong function of the crossflow temperature, jet temperature and jet equivalence ratio. For the data reported here, the trend between *LO* and ϕ_{jet} corresponds to a slight increase in *LO* with a reduction in *J*, due to the interdependent nature of *J* and ϕ_{jet} (described in Section 4.2). This appears as a departure from the Kolb *et al* [32], who demonstrated increases in lift-off with increases in *J*, over a range of *J* values from 6 – 210. However, Kolb *et al* [32] did not show significant change in liftoff for values of $J \leq 20$. In Section 5.2, RJICF with higher values of *J* will be addressed. The observed *J* sensitivity presented here may be due to jet stability effects [15]

associated with low J jets, or simply a dominant ϕ_{jet} sensitivity. The impact of these relationships on NOx production is discussed further in Section 5.1.2.

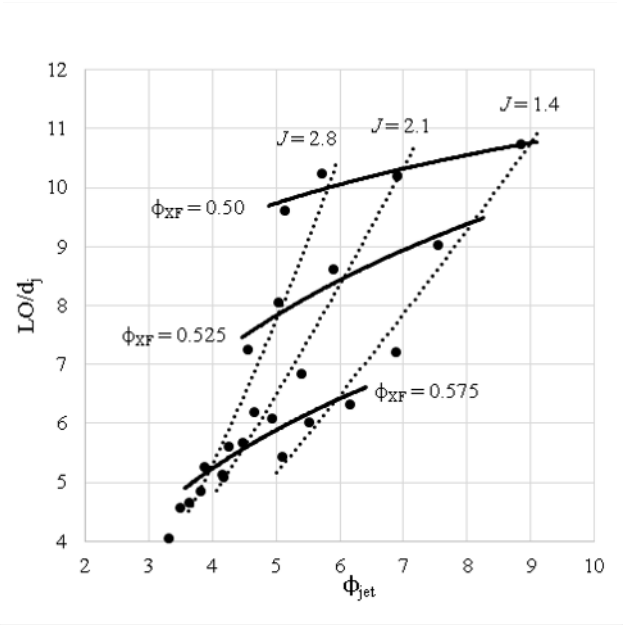

Figure 34 – Dependence of lift-off distance at constant exhaust temperature of 1956K upon the jet equivalence ratio. Contours of constant crossflow equivalence ratio (solid) and momentum flux ratio (dotted) are indicated.

5.1.2 Emissions of Rich Premixed Methane Jets

Figure 35 plots representative results for the NOx production by the RJICF as a function of ϕ_{jet}, at $\phi_{XF} = 0.525$. Also indicated on the figure are contours of constant rise in system equivalence ratio due to the jet ($\Delta\phi$), J, and normalized flame liftoff, LO/d_j. $\Delta\phi$ is used as a measurable surrogate for ΔT in this discussion. It is highly correlated to ΔT or the secondary fuel mass flow rate in a linear fashion for this range of conditions. Immediately apparent from Figure 35 is a clear monotonic relationship between ΔNOx and $\Delta\phi$ at a given

ϕ_{XF}. Thus, as ΔT increases so does RJICF NOx production, which is congruent with the primary sensitivity of RJICF NOx production identified by Roa *et al* [38].

One of the questions highlighted in the introduction concerns the factors that influence NOx production at a given ΔT, as the majority of available data has ΔT varying with other parameters, such as J. Insight into this question is possible by following a fixed $\Delta\phi$ line. At constant values of $\Delta\phi$, the figure shows that the lower J and richer jets produce less NOx than their less rich and higher J counterparts.

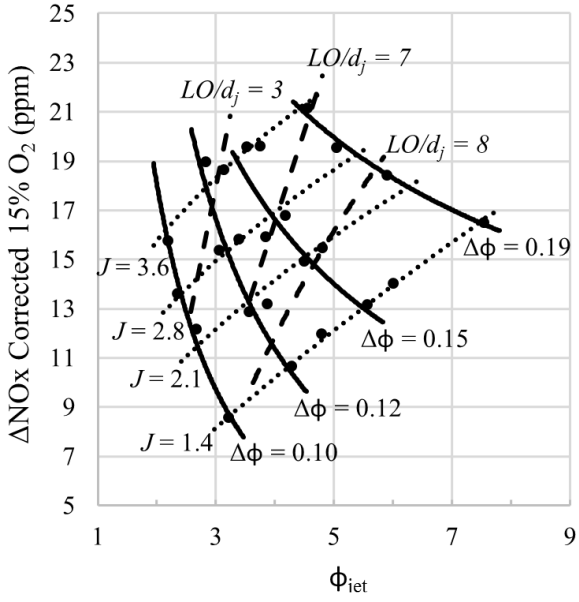

Figure 35 – Dependence of reacting jet NOx contribution at constant crossflow conditions of ϕ_{XF} = 0.525 upon the jet equivalence ratio. Contours of constant temperature rise (solid), momentum flux ratio (dotted), and lift-off distance (dashed) are indicated.

Figure 36 plots the same parameters, except at ϕ_{XF} = 0.625. The increase in ϕ_{XF} implies a hotter crossflow, which also reduces *LO*, as shown. Again, the figure shows a rise in ΔNOx as the fuel flow rate into the jet increases, quantified by $\Delta\phi$ for a given *J* value. For a given $\Delta\phi$ value, it is clearly evident by the contours of differing momentum flux ratio that the richer, lower *J* jets are producing less NOx than their less rich, higher *J* counterparts, as also demonstrated in Figure 35.

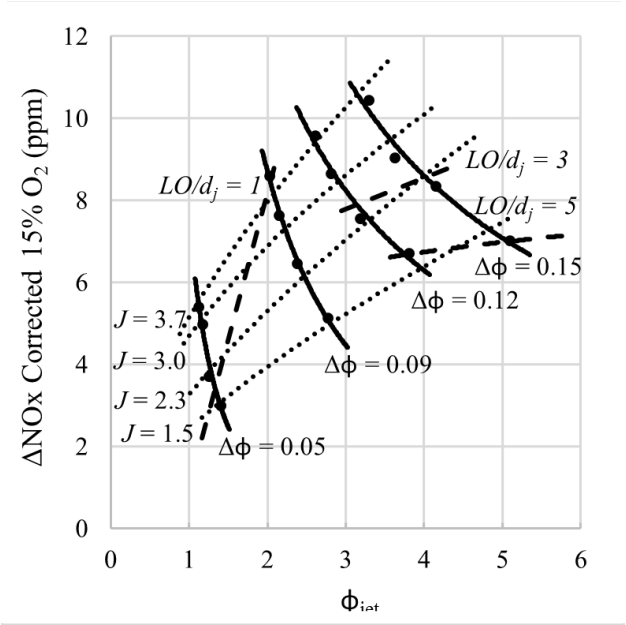

Figure 36 – Dependence of reacting jet NOx contribution at constant crossflow conditions of ϕ_{XF} = 0.625 upon the jet equivalence ratio. Contours of constant temperature rise (solid), momentum flux ratio (dotted), and lift-off distance (dashed) are indicated.

Referring to the contours of constant LO/d_j presented in Figure 35 and Figure 36, the sensitivity of lifting to crossflow temperature and ϕ_{jet} is again evident. The values of *LO* associated with the lower crossflow temperature case (Figure 35) are significantly higher

for similar values of ϕ_{jet} than for the high crossflow temperature case (Figure 36). Also as previously discussed in Section 5.1.1, at constant crossflow conditions and ΔT, *LO* increases with increasing ϕ_{jet} and decreasing *J*. In addition, Figure 35 and Figure 36 also show an increase in *LO* as *J* decreases with constant ϕ_{jet}. As this increase in *LO* at constant ϕ_{jet} involves a reduction in $\Delta\phi$, changes in heat release, in combination with the aforementioned jet stability effects, is a potential driver of the observed *J* sensitivities presented here.

Figure 35 and Figure 36 show contours of constant *LO* cutting across lines of constant $\Delta\phi$. For constant $\Delta\phi$, ΔNOx decreases with increasing *LO*. This is associated with an increase in ϕ_{jet} which has already been shown to correspond to a reduction of ΔNOx at constant $\Delta\phi$. For constant ϕ_{jet}, ΔNOx decreases with increasing *LO* as well. This is associated with a decrease with $\Delta\phi$, which has been shown to correlate with NOx production. While flame lifting certainly has an impact on NOx formation, as Kolb *et al* [32] has similarly demonstrated for a lean premixed jet, *LO* is itself sensitive to parameters such as ϕ_{jet}, *J*, and crossflow temperature that directly impact NOx contribution of the reacting jet.

It is important to note the extent by which ΔNOx varies along a contour of constant $\Delta\phi$. Variations in ΔNOx ranging from 1.5x up to 3x are found in Figure 35 and Figure 36. This variation is considerable. Furthermore, when compared to the change in ΔNOx across $\Delta\phi$, at either constant *J* or ϕ_{jet}, it is clear that it is on the same order of magnitude.

The high equivalence ratio of these jets introduces considerations not touched upon in Chapter 1. First, while it was discussed in Section 1.3 that the stoichiometry at which combustion occurs in a RJICF is critical, due to the strong temperature sensitivity of thermal NOx production rates, the impact of this stoichiometry on other sources of NOx was not touched upon. Other mechanisms of NOx production besides thermal NOx were omitted from the context laid out in Section 1.1 due to their relative insignificance at DLN combustor operating conditions. However, for rich premixed flames, NOx production within the flame (prompt NOx) via the Fenimore mechanism can be significant and is sensitive to equivalence ratio. For this prompt contribution, the rate at which the cyano compounds (e.g. CN and HCN) react to produce NO versus N_2 is dependent on equivalence ratio [6]. Second, for rich premixed burning of the fuel jet, the excess fuel that is not oxidized will be in the form of diluted synthesis gas, H_2/CO, that can subsequently burn either as a non-premixed flame or, if it premixes with the crossflow prior to combustion, as a premixed flame. The stoichiometry of this H_2/CO combustion will have as significant an impact on product temperature, and therefore NOx production, as the initial methane combustion.

5.2 Nitrogen Oxide Sensitivities of Premixed Reacting Jets

This section presents the results for lift-off distance and NOx production in reacting jets with the parameter space described in Section 4.2.2. The results are organized by first discussing the observed regimes of flame stabilization / lifting behavior, followed by the

NOx emissions. In each instance, the data associated with the pipe exit geometry and $J \leq 20$ is used as a reference set to explore the impact of the various RJICF parameters. All data is denoted via the scheme presented in Table 4. Circular points are used for the pipe exit geometry data, triangles for the nozzle exit geometry data, hollow circles are used to denote pipe geometry points with $J = 40$, and x's are used for the forced lifting points via methane doping. In addition all points have a color corresponding to their crossflow condition, with blue for $\phi_{XF} = 0.45$ and red for $\phi_{XF} = 0.50$.

Table 4 – Symbol legend for Section 5.2 figures

●	Data from pipe exit geometry
▲	Data from nozzle exit geometry
○	Data from pipe exit geometry with $J = 40$
✖	Data from methane doped pipe exit geometry
	$\phi_{XF} = 0.45$
	$\phi_{XF} = 0.50$

Finally, two pipe geometry data points and one nozzle geometry data point oscillated in *LO* value between lee-stabilized and "lean lifted" flame stabilization. These points are not plotted because of their intermittent behavior.

5.2.1 Lifting Behavior of Premixed Ethane Jets

As noted in Section 1.3.2, flame lifting has significant influences on pre-flame mixing. As such, while the primary focus of this paper is on NOx emissions, it is appropriate to first describe *LO* characteristics, as it will subsequently be used as a scaling parameter. All flames considered here were either stabilized on the leeward side of the jet

(with lifting of the windward side), or fully lifted. Figure 37 shows measured flame *LO* values as a function of reduced ϕ_{jet} for those jets with $J \leq 20$ ($J = 40$ points are lifted for all ϕ_{jet} values and will be considered further starting in Section 5.2.2.3).[5] The results are indicated as described in Table 4. A secondary axis for ϕ_{jet} is also included for reference. Values of LO/d_j of less than 3 are considered lee-stabilized based on similar behavior presented in the flame probability maps, and values greater than 3 are considered fully lifted.

[5] Reduced $\phi_{jet} \equiv 2\phi_{jet}/(1 + \phi_{jet})$. It was selected to assist in plotting data with such a large range for ϕ_{jet}.

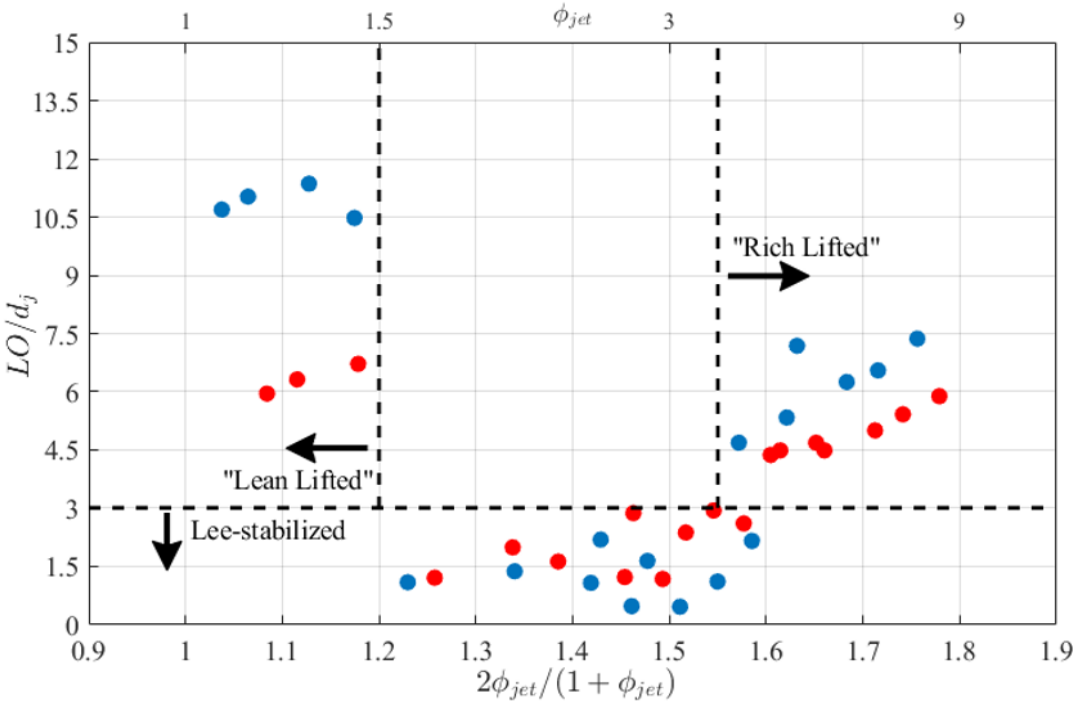

Figure 37 – Lift-off distance for jets with $J \leq 20$ as a function of reduced equivalence ratio for pipe exit geometry at constant crossflow conditions of $\phi_{XF} = 0.45$ and $\phi_{XF} = 0.50$.

Immediately apparent in Figure 37 is the presence of a region of jet equivalence ratios where the flame exhibits lee-stabilized behavior. In addition two branches of fully lifted behavior exist, one with values of ϕ_{jet} lower (more fuel lean) than the central region of lee-stabilization and one with higher (more fuel rich) values of ϕ_{jet}. These branches will be referred to as "lean lifted" and "rich lifted" respectively. It is important to note that, as shown in Figure 37, the transition to "lean lifted" is much more abrupt with respect to jet stoichiometry than the transition to "rich lifted."

Note the impact of crossflow temperature on *LO*. Specifically, increases in temperature (due to increases in ϕ_{XF}) reduce *LO* of the fully lifted branches, as expected. Little change is observed in the transitions between fully lifted and lee-stabilized behavior.

No significant variation in *LO* due to *J* (for $J \leq 20$) was observed, with ϕ_{jet} and ϕ_{XF} emerging as the governing parameters of *LO*. Both Kolb *et al* [32] and the results presented in Section 5.1.1 also observed a strong dependence of flame lift-off height (or distance) on crossflow temperature. The dependency on ϕ_{jet} is in agreement with the results presented in Section 5.1.1. Kolb *et al* [32] did observe an increase lift-off height as *J* was increased. However, Kolb *et al* [32] observed this behavior across *J* values ranging from 6 – 210, but showed little change in lift-off for *J* values of 20 and below.

5.2.2 NOx Emissions Behavior in Premixed Ethane Jets

5.2.2.1 Raw NOx Emissions of Premixed Jets

Figure 38 plots the NOx production from the RJICF (ΔNOx) as a function of Δ*T*. ΔNOx is calculated by subtracting a baseline crossflow NOx level (Section 4.3.1) from the measured reacting jet emissions. The data are indicated as per Table 4, with the uncertainty in the ΔNOx measurement displayed with error bars. Immediately apparent from Figure 38 is the monotonic, nearly linear, overall relationship between NOx production and Δ*T*. Also evident is the variation in NOx at a given Δ*T*. Depending on Δ*T*, this variation can be on the order of 2x. The relationship with Δ*T* is congruent with literature [35, 37, 38] and the

results presented in Section 5.1.2 are in agreement with both this relationship and the potential variation at constant ΔT.

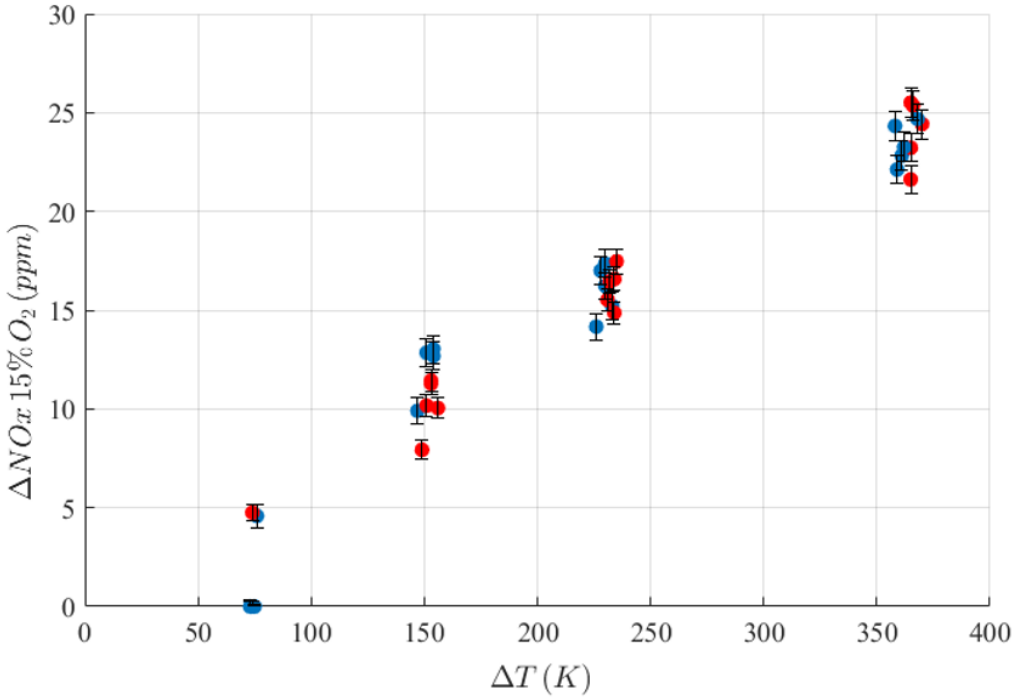

Figure 38 – RJICF NOx production as a function of ΔT at constant crossflow conditions of ϕ_{XF} = 0.45 and ϕ_{XF} = 0.50.

It is useful to normalize the impact of varying ΔT on NOx, to better facilitate analysis of other NOx drivers. To this end, an effective fuel mass flow in the jet ($\dot{m}_{ef}$) was chosen, and is defined as:

$$\dot{m}_{ef} = \dot{m}_{C_2H_6} + {LHV_{CH_4}}/{LHV_{C_2H_6}}\,\dot{m}_{CH_4} \tag{17}$$

where $\dot{m}$ and LHV are the mass flowrates in the jet and lower heating value, respectively. Values for both ethane and methane are used and are denoted by their respective chemical formulas in the subscript. This normalization parameter was chosen for three reasons: first, fuel mass flow rate is more accurately measureable than ΔT itself and is commonly used as a normalization parameter (e.g. to calculate Emission Index [35, 36]); second, weighting $\dot{m}_{CH_4}$ by the ratio of the lower heating values accounts for the difference in heat release per kg of the two fuel species; third, it is nearly linear with ΔT values, as shown by adiabatic flame temperature calculations.

5.2.2.2 Sensitivity of Emissions to Jet Equivalence Ratio

Results presented in Section 5.1.2 identified both ϕ_{jet} and LO as influencing RJICF NOx emissions, but their effects were strongly coupled. To look into the effects of these parameters further, the fully developed velocity profile data is used as a reference. Trends discussed in this section are the same for the top hat velocity profile (exit velocity profile effects are discussed in detail in Section 5.2.2.4). Figure 39 plots ΔNOx normalized by $\dot{m}_{ef}$ as a function of reduced ϕ_{jet} for RJICF and $J \leq 20$. The data is indicated per Table 4.

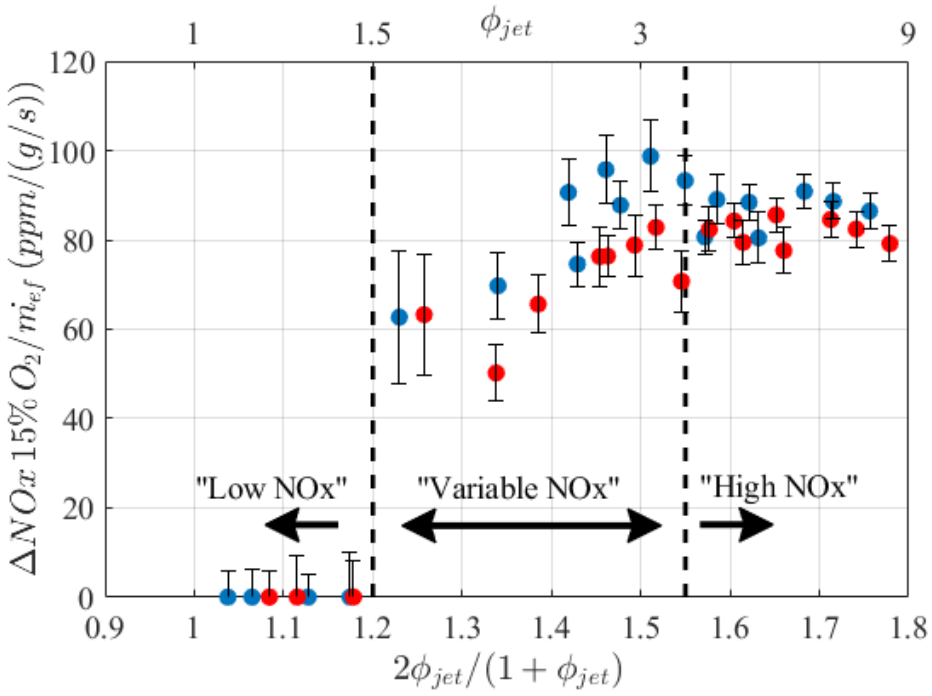

Figure 39 – Normalized NOx production as a function of reduced equivalence ratio for reacting jets with a pipe jet geometry and $J \leq 20$ at constant crossflow conditions of $\phi_{XF} = 0.45$ and $\phi_{XF} = 0.50$.

Figure 39 reveals three regions. At reduced equivalence ratios below 1.2, a region of negligible NOx production exists,[6] labeled "low NOx", regardless of ϕ_{jet} value. In this region, the flames are all lifted. At reduced jet equivalence ratios between 1.2 and approximately 1.5, labeled "variable NOx", the flames are lee-stabilized and the NOx generated monotonically increases with ϕ_{jet}. In other words, for these lee-stabilized flames, the NOx production is dependent on ϕ_{jet}. Above the reduced ϕ_{jet} value of ~1.55, labeled

[6] The emissions measurements for these cases were within the error of the associated base NOx measurement. They are plotted as having a normalized ΔNOx value of 0 with the positive portion of their error bars.

"high NOx", the normalized NOx contribution for this region is relatively invariant with changes in ϕ_{jet}. This sensitivity, or lack thereof, of normalized NOx production on ϕ_{jet} is associated with distinct flame stabilization behaviors. The ϕ_{jet} dependent region is associated with lee-stabilized flames, and the ϕ_{jet} invariant regions are associated with fully-lifted flames, either "lean lifted" or "rich lifted".

5.2.2.3 Sensitivity of Emissions to Flame Lift-Off Distance

Consider further the impact of LO on NOx emissions, by examining normalized ΔNOx values as a function of LO. These data for RJICF with a pipe exit geometry and $J \leq 20$ are presented in Figure 40. The different flame lifting regimes and stoichiometries are also noted.

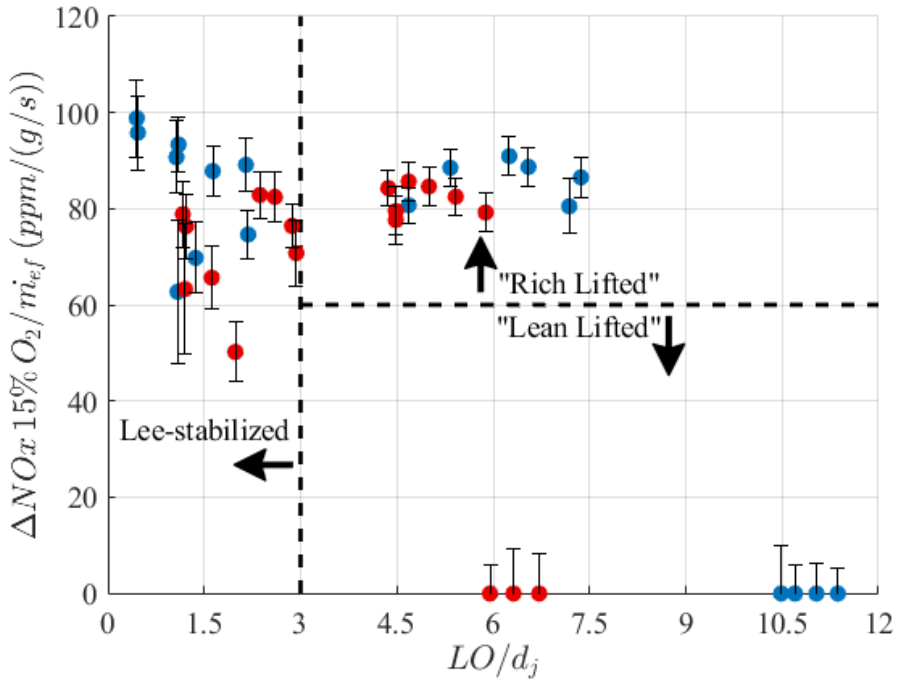

Figure 40 – Normalized NOx production as a function of *LO* for reacting jets with a pipe jet geometry and $J \leq 20$ at constant crossflow conditions of $\phi_{XF} = 0.45$ and $\phi_{XF} = 0.50$.

Figure 40 makes it immediately apparent that, while lifting has a significant impact on NOx production, NOx emissions are not linearly correlated to *LO*. Rather, the results fall into the three groups, using the lee-stabilized, "rich lifted", and "lean lifted" identifiers. The negligible NOx solution is clearly associated with reacting jets exhibiting the "lean lifted" behavior discussed in Section 5.2.1, and high NOx is associated with both lee-stabilized and "rich lifted" reacting jets (also discussed in Section 5.2.1). The lee-stabilized jets show significant variation in NOx*;* as shown in the prior section, these NO variations are associated with variations in ϕ_{jet}. The "rich lifted" jets display the reverse, a range of *LO* values with invariant NOx production.

It is important to note the interdependencies of ϕ_{jet} and *LO* when interpreting these data. All variations in *LO* observed in Figure 40 are accompanied by changes in ϕ_{jet}, as shown in Figure 37. We next consider the methane doped and $J = 40$ results, which allow for variations in *LO* that are independent or much less sensitive to ϕ_{jet}. In all repeated cases, ϕ_{jet} and *J* are identical to the corresponding pure ethane case. The impact of the methane doping and high momentum flux is primarily the same: to induce fully-lifted behavior in the intermediate ϕ_{jet} range that is associated with lee-stabilized flames in the pure ethane, $J \leq 20$ cases.[7] The methane doping had the additional effect of increasing *LO* in "rich lifted" reacting jets. For reference, Figure 64 plots these measured flame *LO* results in Appendix A.2.

The normalized emissions of the pipe geometry data (shown in Figure 39) with the addition of methane doping and $J = 40$ data added is shown in Figure 41.

[7] Note also that the high *J* cases show that there is a *J* impact on *LO*. These observations are consistent with Kolb *et al* [32] who noted lifting in flames with *J* values on the order of 60 and above, and a *J* sensitivity of *LO* for these higher *J* values.

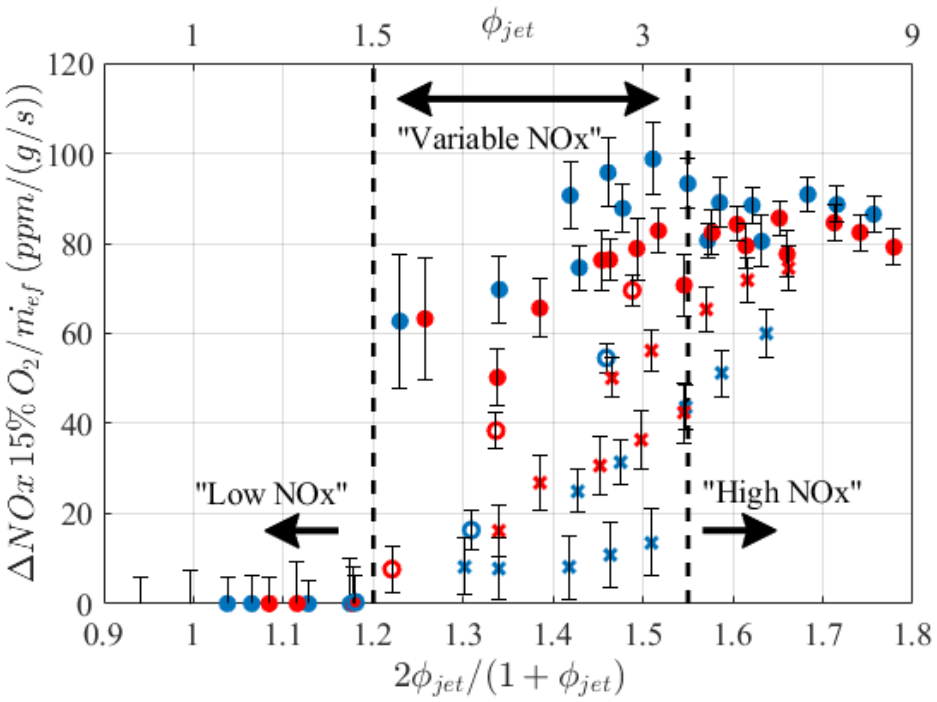

Figure 41 – Normalized NOx production as a function of reduced equivalence ratio for reacting jets (including high *J* and methane doped) with a pipe jet geometry at constant crossflow conditions of ϕ_{XF} = 0.45 and ϕ_{XF} = 0.50.

Every $J = 40$ and methane doped point at similar ϕ_{jet}, compared to $J \leq 20$ data, has a significantly higher *LO*. The key takeaway from Figure 41 is that in every instance, this increase in *LO* is associated with significant NOx reduction, as expected based upon pre-flame mixing considerations. To more explicitly explore how the increase in *LO* impacts NOx production, Figure 42 compares data point pairs between the doped and undoped cases for otherwise identical conditions. Specifically, it plots the change in NOx production due to the doping of the jet fuel with methane as a percentage of the corresponding undoped normalized emission. This metric is plotted as a function of the corresponding change in

LO due to the methane doping. In addition a least squares fit line with a forced intercept of unity is included. This fit will be utilized in Section 5.2.2.4.

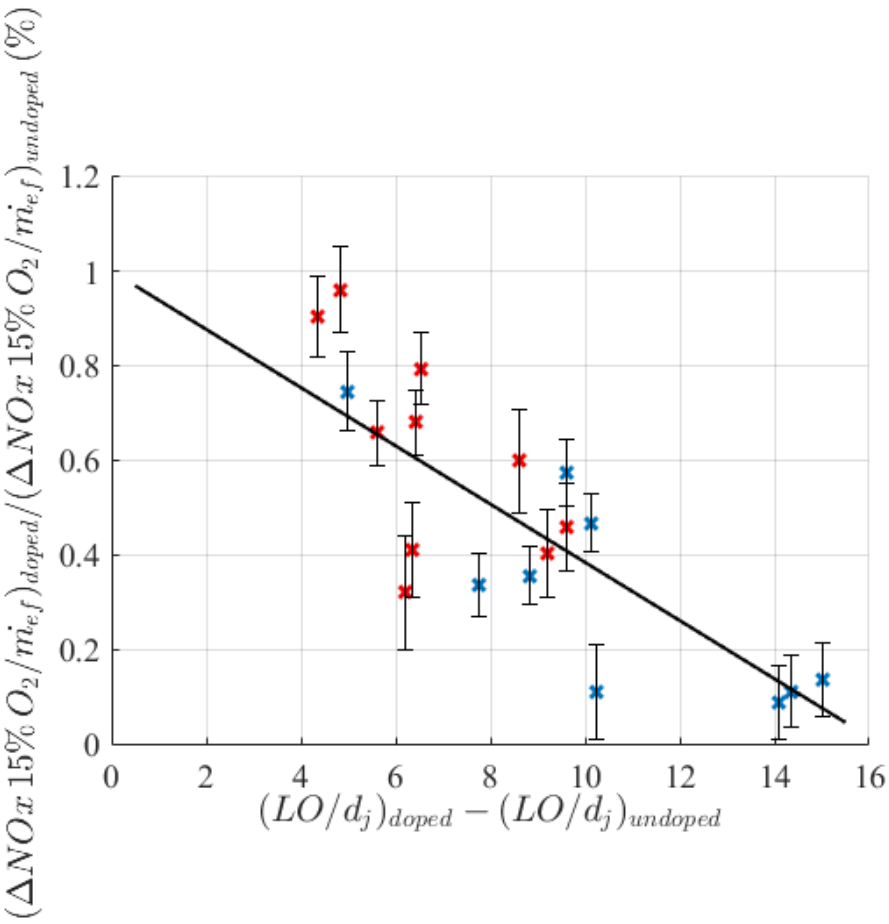

Figure 42 – Fraction of NOx production from ethane/methane/air reacting jets compared to ethane/air reacting jets (all with pipe exit geometry) as a function of the associated change in *LO*. For each point all other test parameters remain constant between the two different compositions.

Figure 42 shows a reduction in NOx with increased *LO*, and quantifies the effect of lifting on the NOx production of RJICF. In general, larger increases in *LO* are associated with larger reductions in NOx. Note that significant fractional reductions in NOx

production are possible by lifting the flame, all other conditions being equal. While not unexpected, this result clearly shows the importance of engineering designs that enhance flame lifting for NOx minimization from RJICF. It is important to note that CO levels of the exhaust were monitored during the experiment. CO levels did not rise significantly for the doped data, indicating the reduction in NOx is not due to partial oxidation of the fuel.

5.2.2.4 Impact of Exit Velocity Profile on Emissions

This section considers the impact of jet exit velocity profiles on NOx production. More fundamentally, these velocity profiles influence *LO* and shear layer growth rates and, consequently, pre-flame mixing rates. For example, several studies [19, 21] have observed more rapid nearfield mixing of the jet with crossflow for nozzle geometries compared to pipe geometries. This increase in mixing rates can be tied back to the sensitivity of the SLV growth rate to jet exit shear layer thickness. The disparity in SLV growth for the different exit velocity profiles can be inferred qualitatively from Figure 43, which shows Mie scattering images from identical rich lifted cases. The images were obtained as described in Section 4.3.4.

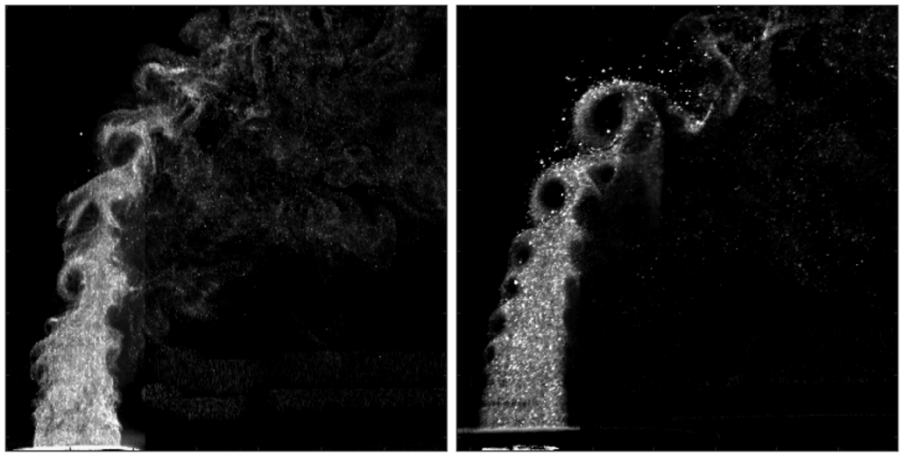

Figure 43 – Mie scattering images of reacting jets in crossflow with a pipe (left) and nozzle (right) exit velocity profiles. Both jets have identical composition, ϕ_{jet} = 4.73, and J = 15.

Because the velocity profile influences both *LO* and SLV growth rates, care must be taken in elucidating the relative effects. There is a slight reduction in *LO* value for the top hat exit velocity profile relative to the fully developed profile for cases where the flame is lifted. In addition, the nozzle geometry jets transition from "lean lifted" to lee-stabilized at lower values of ϕ_{jet} than the jets with pipe injection geometry. These results are illustrated in Figure 65 in Appendix A.2.

Consider next the SLV growth rate impact of the two jet geometries. Figure 44 plots the ratio of NOx production from the nozzle jet profile to that from the pipe case. In order to exclude the *LO* impact noted above, the following procedure was used for comparison of data points. Data associated with "lean lifted" flames are not plotted as the NOx production remains negligible in the "lean lifted" cases for the nozzle geometry. Also

excluded are the transitional ϕ_{jet} points where one geometry is lifted and the other attached. For the remaining points that are to be discussed next, the nozzle geometry has a lower *LO* relative to the pipe geometry that is on the order of a single jet diameter, as shown in Figure 65. The data for the subset just described are adjusted using the linear fit in Figure 42 back to constant *LO* values, which changes the raw ratios by about 5% to account for the slight difference in *LO* values between the two geometries.

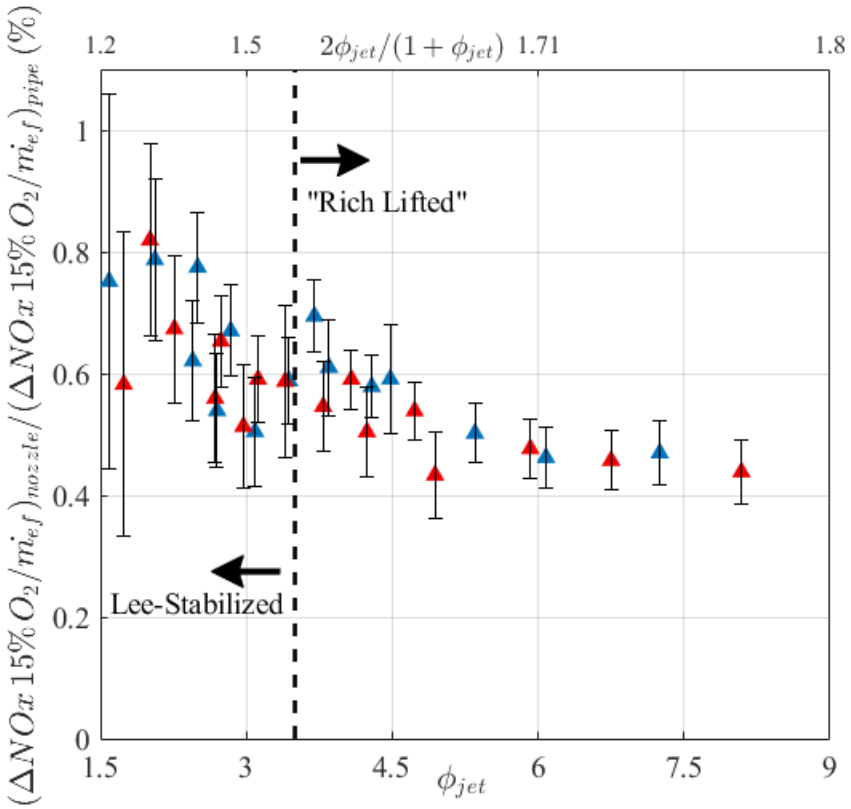

Figure 44 – Fraction of NOx production from reacting jets with nozzle geometry compared to reacting jets with pipe geometry as a function of the associated change in ϕ_{jet}.

Figure 44 shows that the NO production from the nozzle geometry is about 20-55% lower than that corresponding to the pipe geometry. The magnitude of this reduction is dependent on ϕ_{jet} (which is accompanied by variations in LO) with larger reductions in NOx for richer jet stoichiometry. This effect does level off at very rich equivalence ratios ($\phi_{jet} > 4.5$) with NO levels asymptoting to approximately 45% of those found for the pipe geometry. This demonstrates that, at low LO, the magnitude of the impact of a change in exit velocity profile is more significant with higher ϕ_{jet}. As LO increases to fully lifted values the impact is constant and invariant with both LO and ϕ_{jet}. As with the methane doped cases, no accompanying rise in CO with the reduction in NOx was observed.

These results are consistent with the hypothesis that the increase in shear layer growth with the nozzle geometry increases pre-flame mixing rates, and drives down NOx production; e.g., the NO reduction effect increases as ϕ_{jet} and LO increase. However, the fact that a reduction is observed even for attached flames, where the pre-flame mixing is reduced, suggests that post-flame mixing effects are also present. Since the downstream CVP structures that would influence post-flame mixing are themselves ultimately due to the re-orientation of SLVs, it is reasonable to expect a coupled influence of pre- and post-flame mixing effects. Further work is needed to develop approaches to decouple pre- and post-flame mixing and to quantify their relative impacts on NOx.

5.2.3 Equivalence Ratio of Combustion Considerations

Overall, the data presented thus far in this chapter are consistent with the hypothesis that within constant ΔT NOx emissions are controlled by the stoichiometry at which combustion actually occurs, which will be referred to as ϕ_{Flame}. The objective of this section is to explore this hypothesis.

ϕ_{Flame} is influenced by ϕ_{jet}, as well as pre-flame mixing of the jet and crossflow, captured in this investigation by nozzle geometry and LO. Consider the impact of LO and ϕ_{jet} on ϕ_{Flame}. For a fixed crossflow condition, ϕ_{jet} serves as the initial condition for the evolving stoichiometry of the reactants. In turn, LO controls the spatial duration over which pre-flame mixing occurs. The spatial duration can be transformed into a temporal one by utilizing the jet exit flow velocity, $\tau_{pre\text{-}flame} = LO/u_j$. The rate of mixing during this time is a function of the flowfield, which in turn is a function of the instability of the SLVs (most strongly influenced by exit velocity profile in this data).

The three branches of NOx emissions shown in Figure 39 are readily interpretable with this approach. As a reminder, the three branches are: negligible NOx production associated with "lean-lifted" flames, ϕ_{jet} dependent NOx production in lee-stabilized flames, and high NOx production in "rich-lifted" flames that is invariant with LO and ϕ_{jet}.

For the negligible NOx case, the low NOx production suggests a lean ϕ_{Flame} value and therefore low flame temperatures. This interpretation is supported by the lower ϕ_{jet} values and large LO values associated with the low NOx production cases, indicating a well-mixed jet and crossflow. It would also account for the lack of sensitivity to either LO

or ϕ_{jet}. As long as the resulting value of ϕ_{Flame} due to the variation of these parameters is below the threshold of significant NO production, the reacting jet NOx emission would remain negligible. In the lee-stabilized regime of increasing NOx with increasing ϕ_{jet}, this correlation would indicate that ϕ_{Flame} is varying with ϕ_{jet}. Due to the much more limited variation of LO in this region, it stands to reason that ϕ_{Flame} and ϕ_{jet} are much more closely coupled. The "rich-lifted" data exhibits near constant NOx levels. This would suggest a more constant value of ϕ_{Flame}, and a decoupling of its value from $\phi_{jet.}$ Due to the elevated emissions levels, the value of ϕ_{Flame} would most likely be near stoichiometric combustion and its high flame temperatures. The lack of sensitivity of NOx to LO or ϕ_{jet} in this region is due to the variation of these parameters in combination with the fluid mechanic mixing rate to achieve roughly constant ϕ_{Flame}. Near stoichiometric ϕ_{Flame} would also have a high flame speed to assist with stabilization, and would also be the non-premixed limit as ϕ_{jet} increases towards pure fuel.

The reduction in NOx associated with increased LO or increased fluid mechanic mixing rate (exit velocity profile) at fixed conditions shown in Figure 42 and Figure 44 can also be re-interpreted from the perspective of ϕ_{Flame}. In both cases, ϕ_{Flame} is driven to leaner values by the increase in duration or rate (or both) of the pre-flame mixing region at fixed ϕ_{jet}. This is consistent with the hypothesis that a reduction in ϕ_{Flame} leads to a reduction in NOx as plotted in Figure 42 and Figure 44.

These pre-flame mixing ideas can be further explored through the use of a simple mixing model. Consider the RJICF pre-flame mixing as a parcel of fluid at an initial stoichiometry (ϕ_{jet}) that entrains and/or exchanges mass with the crossflow reservoir at a lower equivalence ratio (ϕ_{XF}). The spatial rate of change of the equivalence ratio of that parcel of fluid would be proportional to a mixing rate and the difference between the equivalence ratio of the parcel and the crossflow with which it is mixing; i.e:

$$d\phi/dr = -1/\ell_m (\phi - \phi_{XF}) \tag{18}$$

where r is the distance from the jet exit, and ℓ_m is a mixing length scale. Solving this equation with $\phi = \phi_{jet}$ as an initial condition and $\phi = \phi_{Flame}$ at LO yields the following:

$$\phi_{Flame} = (\phi_{jet} - \phi_{XF}) e^{-LO/\ell_m} + \phi_{XF} \tag{19}$$

This relationship can be also be recast as the following relationship between LO and ϕ_{jet}:

$$LO/d_j = \ell_m/d_j \, ln(\phi_{jet} - \phi_{XF}) - \ell_m/d_j \, ln(\phi_{Flame} - \phi_{XF}) \tag{20}$$

The above discussion hypothesized that constant normalized NOx (such as in the "rich lifted" regime) corresponds to a constant value of ϕ_{Flame}. If ϕ_{Flame} is constant for a given set of data (i.e., independent of LO and ϕ_{jet}), Equation 20 predicts a linear relationship

between LO/d_j and $ln(\phi_{jet} - \phi_{XF})$, with a slope and y-axis intercept of ℓ_m/d_j and $\ell_m/d_j \, ln(\phi_{Flame} - \phi_{XF})$, respectively.

Motivated by Equation 20, Figure 45 plots *LO* as a function of $ln(\phi_{jet} - \phi_{XF})$ for three subsets of data with a linear fit shown for each subset. The first set (Case 1) is the "rich lifted" points associated with the pipe exit geometry (solid fit line). The second set (Case 2) is the "rich lifted" points associated with the nozzle exit geometry (dash-dot fit line). Both of these sets have normalized NOx levels that are invariant with ϕ_{jet} and *LO*; thus, we anticipate a linear trend and a lower slope of the nozzle data than the pipe data due to the faster mixing rates. The third subset (Case 3) is selected from the methane doped pipe exit geometry data based on self-similar NOx values (dotted fit line). Due to being fully lifted RJICF with a pipe exit geometry, a linear relationship with a similar slope to Case 1 but a significant shifted intercept (due to a different ϕ_{Flame} value) is anticipated. These three data sets correspond to circular, triangular, and x data points, respectively.

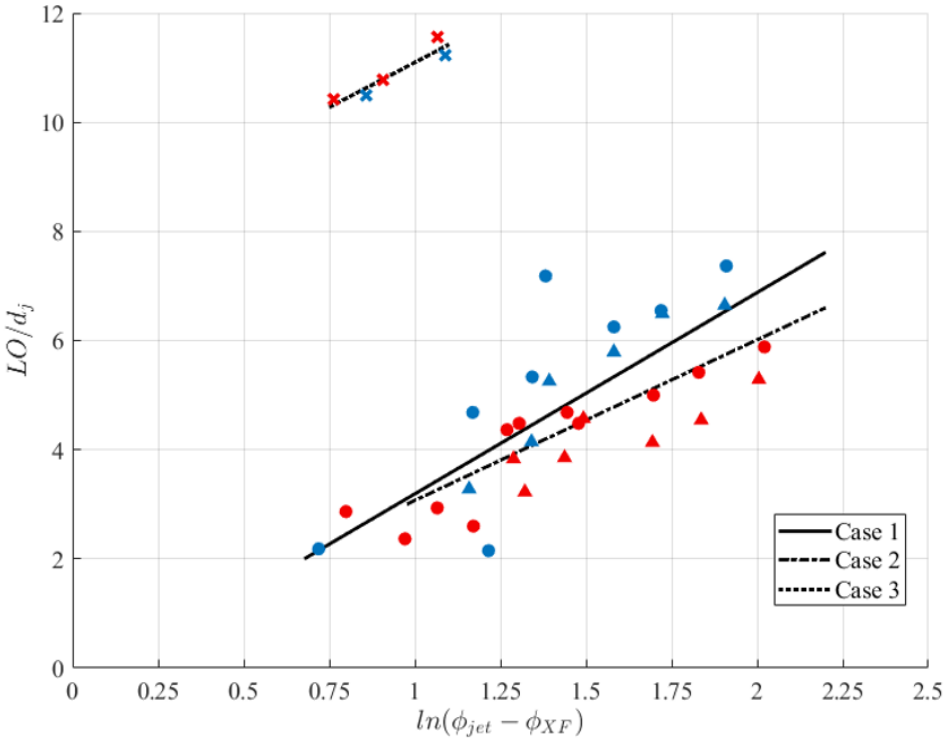

Figure 45 – Plot of selected RJICF data using analytical form suggested by Eq. 20.

Figure 45 bears out the anticipated results outlined above and helps visualize the impact of exit velocity profile and forced liftoff. Case 3 does indeed show a similar slope, which supports similar mixing rates in the two sets of pipe geometry lifted reacting jets. The significantly increased y-intercept of Case 3 compared to Case 1 results in a significantly leaner value for ϕ_{Flame} when calculated. This reduction in ϕ_{Flame} due to increased LO is in agreement with the lower normalized NOx levels measured for these test points. With regards to the exit velocity profile, Case 2 does indeed exhibit a lower slope compared to Case 1, corresponding to a smaller spatial mixing length scale and therefore faster spatial mixing rate compared to the pipe data. This is in agreement with

literature [19, 21]. In addition the shift in y-intercept (with the change in ℓ_m accounted for), results in a small reduction in ϕ_{Flame}. If the preferred ϕ_{Flame} is near values associated with peak flame temperatures (as hypothesized) this would account for reduction in NOx levels. However, if the preferred ϕ_{Flame} was significantly richer than this peak, NOx levels should increase. Although, increased post flame mixing could compensate for this to a degree. It is also important to note that when considering the confidence intervals of the respective slopes there is significant overlap. At this point, therefore, it is still not possible to pinpoint the relative impact of exit velocity profile on pre-flame and post-flame RJICF mixing.

5.3 Impact of Preflame Mixing on Equivalence Ratio of Combustion

The overall objective of this section is to evaluate the extent to which NOx emissions can be correlated with averaged pre-flame mixing levels. As such, these results are organized into three parts. The first qualitatively discusses the instantaneous mixture fraction fields to assess any evident differences between RJICF with different parameters and then how these differences manifest in the time averaged mixture fraction field. The interaction between the expected mixture fraction field and flame position is also discussed. The second part examines the time averaged pre-flame mixing rates of these flows. The third part compares NO production rates calculated based on the presented data with NOx emissions measurements previously presented in Section 5.2.

In each instance, the data associated with the nozzle exit geometry and $J \leq 20$ is used as a reference point to explore the impact of the various RJICF parameters. For the sake of consistency, the data is denoted via the scheme presented in Table 5 throughout all subsequent figures. Circular points are used for the pipe exit geometry data, triangles for the nozzle exit geometry data, hollow points are used to denote data with $J = 40$, and x's and +'s are used for the forced lifting points via methane doping for pipe and nozzle geometries. In addition all points have a color corresponding to their crossflow condition, with blue for $\phi_{XF} = 0.45$ and red for $\phi_{XF} = 0.50$.

Table 5 – Symbol legend for Section 5.3 figures.

▲	Data from nozzle exit geometry
△	Data from nozzle exit geometry with $J = 40$
✚	Data from doped nozzle exit geometry
●	Data from pipe exit geometry
✖	Data from doped pipe exit geometry
	$\phi_{XF} = 0.45$
	$\phi_{XF} = 0.50$

As a final note, the data presented herein is a subset of the parameter space described in Section 4.2.2. The data presented is that which was of sufficient quality to be successfully processed by the method described in Section 4.4.2. Some data points were unusable due to overabundance of reflections and/or poor seeding densities.

5.3.1 Fraction Fields and Flame Position of Premixed Jets

This section presents illustrative results for mixture fraction fields and flame position statistics. Figure 46 shows three consecutive instantaneous mixture fraction fields for three

jet conditions. The time sequence is shown from left to right in the figure. The various jet conditions presented have the following parameters from top to bottom: $J = 8$ with nozzle geometry, $J = 15$ with nozzle geometry, and $J = 15$ with pipe geometry. For clarity, these images do not have near flame values discarded. However, in these instances the flame is located in a position that does not impact the following discussion of the figure. Evident in Figure 46 is the well-formed shear layer vortices in the nozzle geometry cases, especially in comparison to the pipe case. The higher J cases present with observably higher jet penetration transversely into the crossflow. While it is difficult to see a difference in trajectory between the nozzle and pipe geometries in these cases, it is apparent that the jet fluid maintains more coherency than in the nozzle case which appears to more effectively disperse the jet fluid.

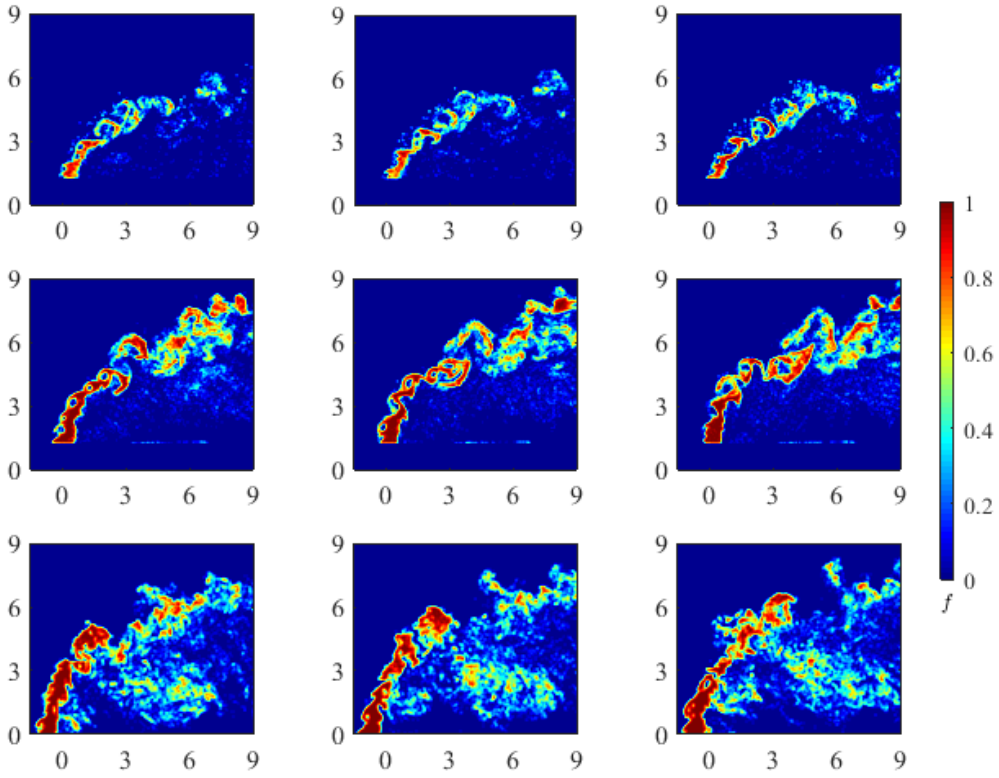

Figure 46 – Sequence of three successive instantaneous mixture fraction fields (left to right) for three reacting jets (top to bottom). The jets have the following parameters: $J = 8$ with nozzle geometry (top), $J = 15$ with nozzle geometry (middle), and $J = 15$ with pipe geometry (bottom). Axis are coordinates normalize by d_j.

Figure 47 shows the averaged mixture fraction fields for the three RJICF whose instantaneous images were presented above. As discussed the values are conditioned based on flame position and points with less than 100 samples are discarded (area shown in grey on image).[8] Also plotted are mean concentration centerline trajectories. The jet trajectory

[8] The flame associated with the field shown in the right pane of Figure 29 was highly lifted and not-steady in position, resulting in all locations with > 100 samples.

was determined using a power law fit of the loci of maximum f values in a manner similar to Gevorkyan *et al.* [19]. In the time-averaged fields the higher transverse jet penetration with increased J is clearly evident, as is an increase in the length of the jet core. Comparing the left and right panes of Figure 47, corresponding to the nozzle and pipe geometries, it is observable that the jet fluid persists in higher mixture fractions further along the jet trajectory, indicating reduced pre-flame mixing in comparison to the nozzle exit geometry.

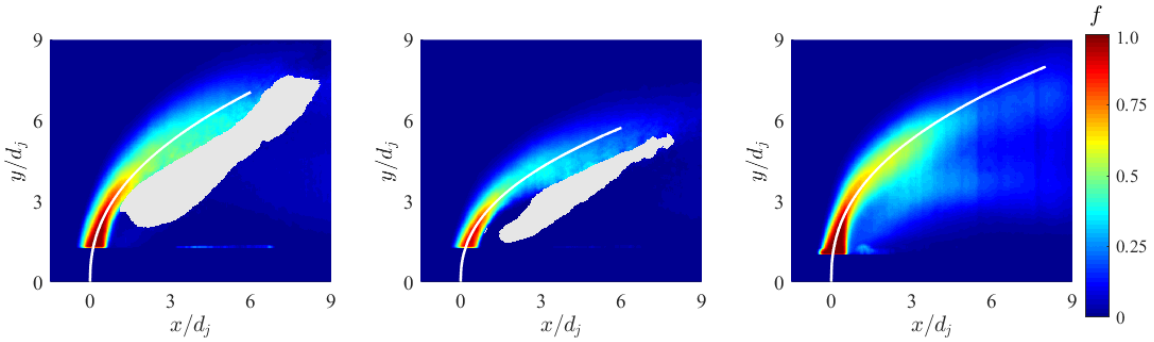

Figure 47 – Time average mixture fraction fields for three reacting jets. The jets have the following parameters: J = 15 with nozzle geometry (left), J = 8 with nozzle geometry (middle), and J = 15 with pipe geometry (right).

The discussion in Section 5.2.1 identified three regimes of flame behavior that were associated with different NOx emissions behaviors. Figure 48 shows expected mixture fraction fields for a characteristic data point for each of the three flame behaviors: “lean lifted”, lee-stabilized, and “rich lifted.” Overlaid onto the mixture fractions maps is the stoichiometric mixture fraction contour shown in white and an instantaneous flame edge in magenta. The J value for all three jets are identical. These images provide significant insight into the flame stabilization behavior of each of these flames.

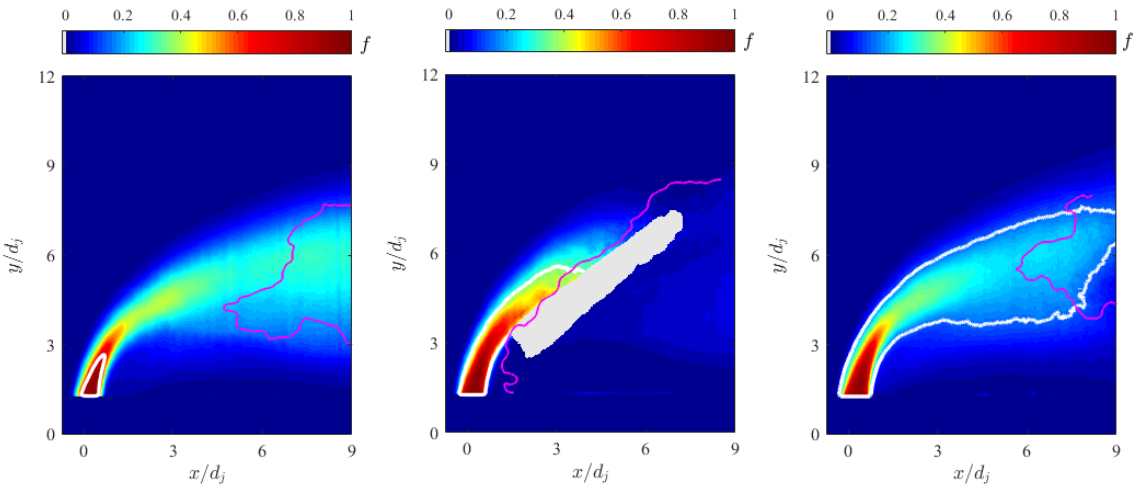

Figure 48 – Instantaneous flame position superimposed onto expected mixture fraction fields for a "lean lifted" (left), lee-stabilized (center), and "rich lifted" (right) flame.

For the "lean lifted" case, in the left pane of Figure 48, the flame sits well away from the stoichiometric contour and roughly centered on the scalar centerline. The lee-stabilized case, in the center pane of Figure 48, displays a lean flamebase situated in the lee of the RJICF that serves as an anchor for a flame angling into and across the jet trajectory. This is most likely a premixed flame propagating into the jet fluid reactants that is anchored by the lean flamebase in the wake of the jet. This is congruent with the findings of Schulz and Noiray [29] who identified that attached RJICF flames initiate in regions corresponding to the most reactive mixture fraction, which is very lean in this configuration due to the temperature discrepancy between the jet and crossflow. Finally, the "rich lifted" case, in the right pane of Figure 48, shows that the flamebase/front configuration has been shifted downstream. The presence of a stabilizing flame base is still interpreted, as is a front propagating into the reactant steam. However, the richness of the jet has forced the flame

to situate itself further downstream in order that the propagating flame meets a flammable mixture. These observations support the hypothesis presented in Section 5.2 with regards to the different flame behaviors.

In addition, Figure 48 clearly indicates that the flame spans a wide range of mixture fractions and thus equivalence ratios of combustion, ϕ_{Flame}. This variation will induce a large variation in the adiabatic flame temperature along the flame edge and consequently significant variation in NOx production rates in the post-flame region directly behind the edge. This highlights the need to utilize an estimated NO production rate, to assess the consequence of ϕ_{Flame}, in order to properly weight the variation in flame temperature (T_{Flame}) and local availability of oxygen and nitrogen.

5.3.2 Pre-flame Mixing Length Scales of Premixed Jets

As noted in Section 5.2.3 and evident from the images in Figure 47 and Figure 48, the pre-flame mixing rates, expressed through the decay of the centerline concentration, are themselves functions of *J*, exit velocity profile, and flame position [19, 21, 33]. In this section, we define and characterize representative mixing lengths enabling us to reduce the spatial mixing fields.

From the concentration jet trajectories, the evolution of the centerline concentration can be extracted. Figure 49 plots three examples of the decay of the centerline mixture fraction as a function of distance along the trajectory (s_c). The three cases correspond to

those presented in Figure 46 and Figure 47. Also plotted are reference power law decay rates for centerline decay rates from literature[18-20]. The scalar potential core is clearly evident in Figure 49, persisting to approximately $s_c/d_j = 2.0 – 2.5$; indicating a relationship between the potential core length and J, congruent with Gevorkyan *et al* [19]. In addition, the decay of the mixture fraction field is also clearly apparent, as is a disparity between the rate of decay for the nozzle and pipe cases. From these results, two distinct length scales are evident, associated with the potential core length (ℓ_{core}) and the decay length scale (ℓ_{decay}). The two length scales are defined as the s_c/d_j value require to reach mixture fractions of 0.975 and 0.6 respectively.[9]

[9] The 0.6 threshold was selected based on the limit of the centerline concentration decay for the pipe cases along the fitted trajectory, which is finite in length.

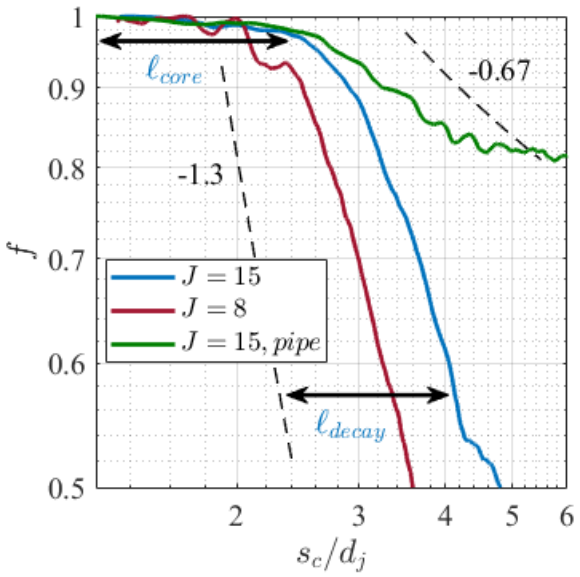

Figure 49 – Mixture fraction values as a function of distance along jet scalar trajectory for three reacting jets: *J* = 15 with nozzle geometry (blue), *J* = 8 with nozzle geometry (red), and *J* = 15 with pipe geometry (green).

Figure 50 plots ℓ_{core} and ℓ_{decay} as a function of *J*, with the data indicated per Table 5. For ℓ_{core}, a strong correlation between the potential core length and *J* is again apparent. This is agreement with Gevorkyan *et al* [19], who presented similar results. This agreement with literature helps alleviate concerns associated with particle overlap as discussed in Section 4.4.2. The dependence of ℓ_{core} on *J* is in large part due to the impact of the jet exit velocity (which *J* is directly related to since the crossflow velocity is held constant) on how long the jet potential core persists. Gevorkyan *et al* [19] also showed that the decay rates post core had little correlation to *J* and could be more varied. This trend is also evident in Figure 50 when examining ℓ_{decay}.

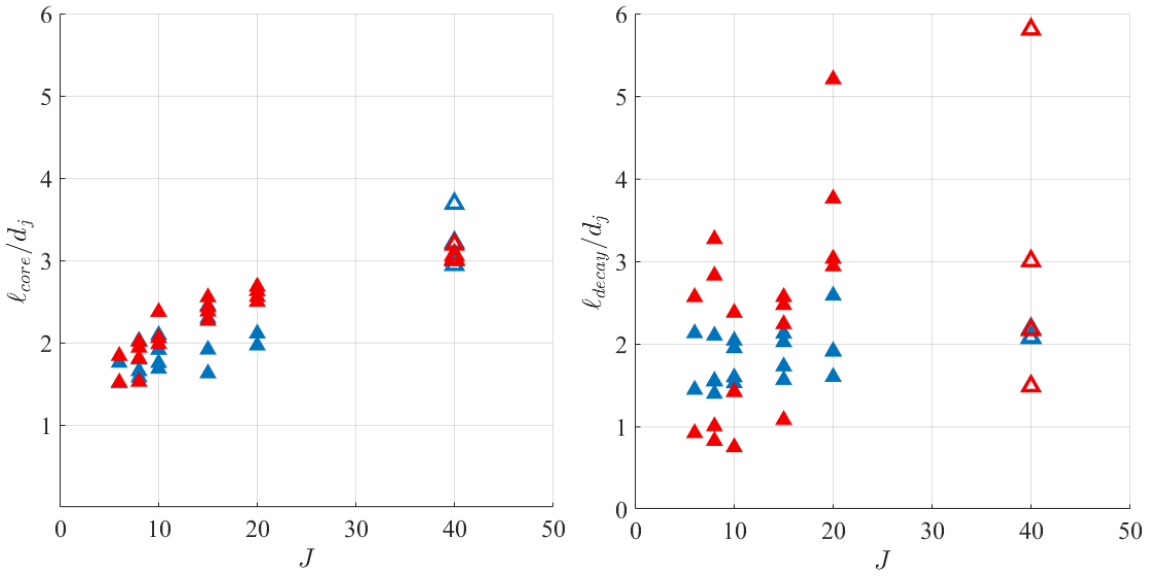

Figure 50 – Potential core (left) and decay rate (right) length scales as a function of J for reacting jets with nozzle geometries at constant crossflow conditions of ϕ_{XF} = 0.45 and ϕ_{XF} = 0.50.

Considering the impact of flame position next, it was noted in Section 1.3.2 that Nair *et al* [33] observed a suppression of SLV growth in RJICF cases where the flame was in close proximity to the jet exit. As a result, a dependency of ℓ_{core} or ℓ_{decay} on whether a flame was lee-stabilized or fully lifted would be expected. However, no significant correlation was observed. The previously noted trends remained dominant. This result is unexpected as Nair *et al* [33] observed the suppression of SLV growth in RJICFs with the flame in close proximity of the jet exit. However a significant difference between that work and the data presented here is that Nair *et al* [33] analyzed jets that were primarily fully attached as opposed to lee-stabilized. In fact, Nair *et al* [33] notes a reduction in the strength of the suppression when the windward edge begins to lift. This finding sparks the need for

further work to identify what the impact of a lee-stabilized flame is on the JICF vorticity field.

Finally the impact of exit velocity profile is considered. In this instance, $\ell_m \equiv \ell_{core} + \ell_{decay}$ will be used as a metric to assess the disparity in pre-flame mixing rates between the different exit velocity profiles. Figure 51 plots the mixing length scales for both nozzle and pipe exit geometry test cases as a function of J (similar to Figure 50).

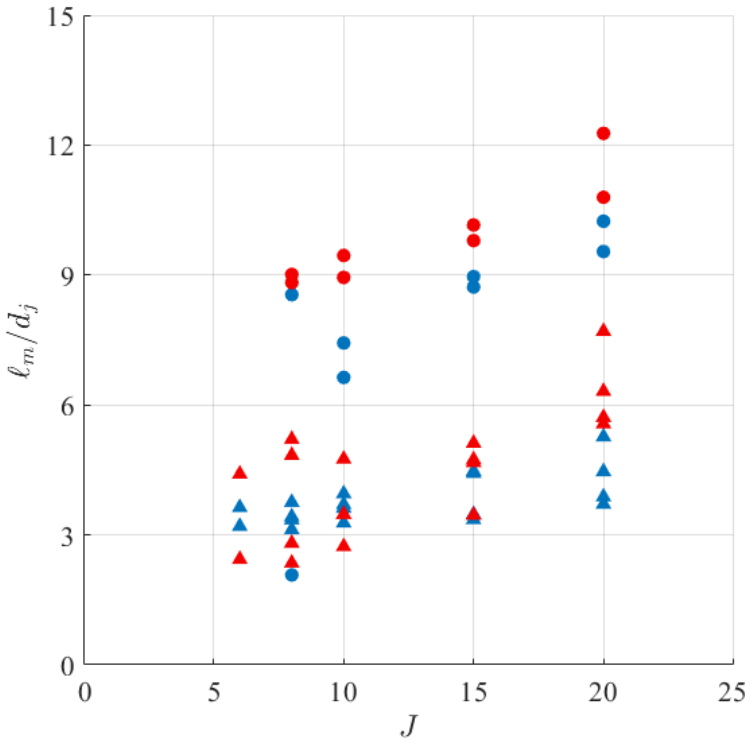

Figure 51 - Pre-flame mixing length scales as a function of J for reacting jets with both nozzle and pipe exit geometries at constant crossflow conditions of ϕ_{XF} = 0.45 and ϕ_{XF} = 0.50.

The pipe data has significantly higher ℓ_m values that those associated with the nozzle geometry, on the order of 2x. This finding is congruent with the observation of New *et al* [21], reviewed in the Introduction, that higher SLV growth rates can be found in jets with nozzle geometries compared to the fully developed pipe. This further supports importance of SLV growth rates in pre-flame mixing.

5.3.3 Comparison of NO Production Rates to NOx Emissions for Premixed Jets

This section assess whether time-averaged pre-flame mixing considerations can accurately capture NOx emissions levels in RJICF. This is assessed via NO production rates calculated from time-averaged mixture fraction fields and equilibrium considerations as described in Section 4.4.3. The calculated NO production rates are compared to measured NOx emissions taken under identical test conditions. The NOx emissions data and its parametric sensitives were discussed in Section 5.2. This section begins its analysis by focusing on two key functional parameters for ϕ_{Flame} hypothesized in Section 5.2.3: pre-flame mixing duration and rate. Pre-flame mixing duration is investigated via the comparison of the undoped and doped data point pairs that generate variations in *LO* at fixed jet parameters as described in Section 4.2.2. Pre-flame mixing rate is investigated via comparison of the nozzle and pipe exit geometries as Section 5.3.2 confirmed the disparity in mixing rates between these cases. Finally a complete comparison of the nozzle data set with the measured NOx emissions is presented.

5.3.3.1 Impact of Forced Liftoff on NO Production Rates for Premixed Jets

The results presented in Section 5.2.2.3 indicated a strong correlation between NOx reduction and LO in cases where ϕ_{jet} was constant, mainly through forcing increased LO via the doping of the ethane fuel with methane at constant ϕ_{jet}. Figure 52 shows the change in NOx against the change in $d[NO]/dt$ due to the fuel stream doping. The change is indicated as percentage of the undoped value. Data with both with nozzle and pipe geometries are plotted, denoted as per Table 5, with the uncertainty indicated by error bars.[10]

[10] The contributions to the uncertainty in NO production rate are the variance of mixture fraction at a given location determined by the mixture fraction variance field and the variance in flame location.

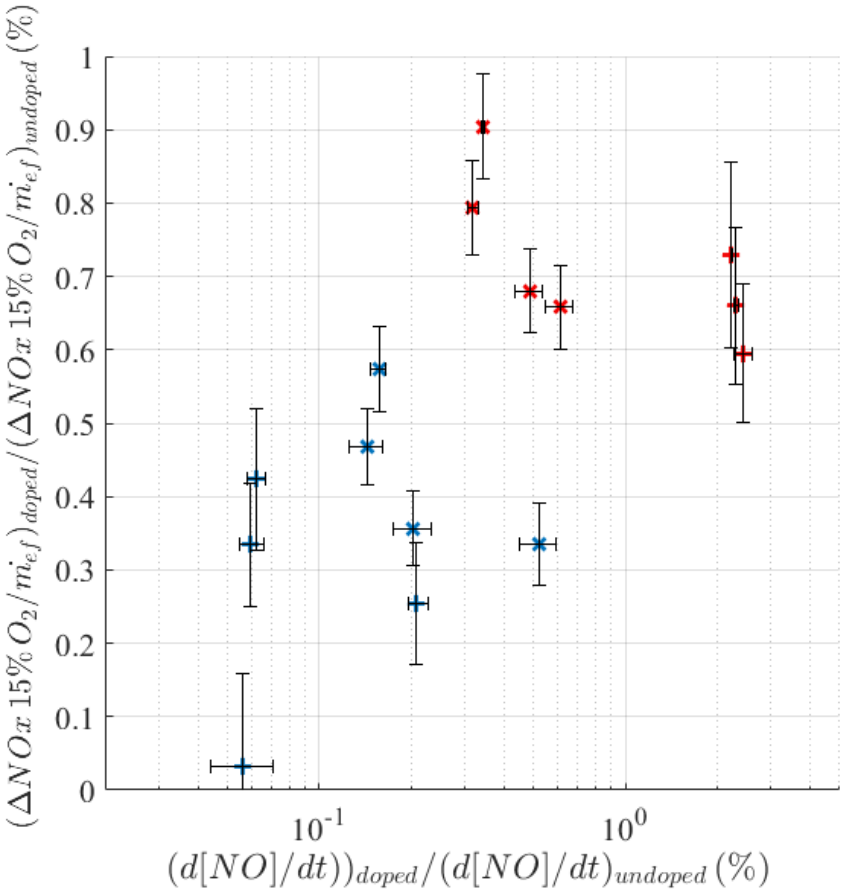

Figure 52 - Change in NOx with change in thermal NO production rates for doped data pairs for reacting jets with nozzle and pipe geometries at constant crossflow conditions of ϕ_{XF} = 0.45 and ϕ_{XF} = 0.50.

The discussion presented in Section 5.3.2 indicated a lack of significant variation in mixing length scale with *LO.* Therefore, it is anticipated that the major driver for the NOx reduction associated with forced liftoff is due to the manipulation of ϕ_{Flame}. For the majority of data, Figure 52 indicates reductions in NOx corresponding to reductions in *d[NO]/dt* for the majority of the data as expected. However, several test points experienced an increase in NO production rate but were still observed with a significant NOx reduction. These

observations indicate other significant factors at play. While the near field mixing data (Section 5.3.2) indicates that flame position does not have a large impact on SLV growth rate in these lee-stabilized and fully lifted premixed RJICF, the data presented in Figure 52 shows that the far field mixing in the form of the CVP might be impacted due to NOx reduction despite elevated NO production rates. It also suggests that post-flame dilution rates are an equal order parameter of significance compared to ϕ_{Flame}. This spurs another need for further work: to characterize the impact of parameter variation on the far field mixing rate, potentially in the form of CVP strength and size.

As for why certain points experienced a rise in NO production rates with increased LO: these points correspond to data that was lee-stabilized near the rich end of the stabilization range. It is likely that they transitioned into a "rich lifted" modality when doped and not a "lean lifted" one. This would create a situation with similar T_{Flame} but increased [O].

5.3.3.2 Impact of Exit Velocity Profile on NO Production Rates of Premixed Jets

Consider now the impact of varying jet exit velocity profile. Section 5.2.2.4 indicated a reduction in NOx data with the nozzle exit velocity profile compared to the pipe. Due to the nature of the relationship, it was however unclear whether the higher SLV growth found in JICF with nozzle geometries compared to pipe geometries , as observed by New *et al* [21], generated a reduction ϕ_{Flame} or an enhancement of post-flame dilution rates (or both).

Figure 53 plots the change in NOx emissions due to the change in exit velocity profile to a fully developed profile as a percentage of the corresponding normalized emission from the top hat profile case. This change is plotted as a function of the percentage change in *d[NO]/dt* due to the change in exit velocity profile. A dashed line indicating a 1:1 correlation is also shown for reference.

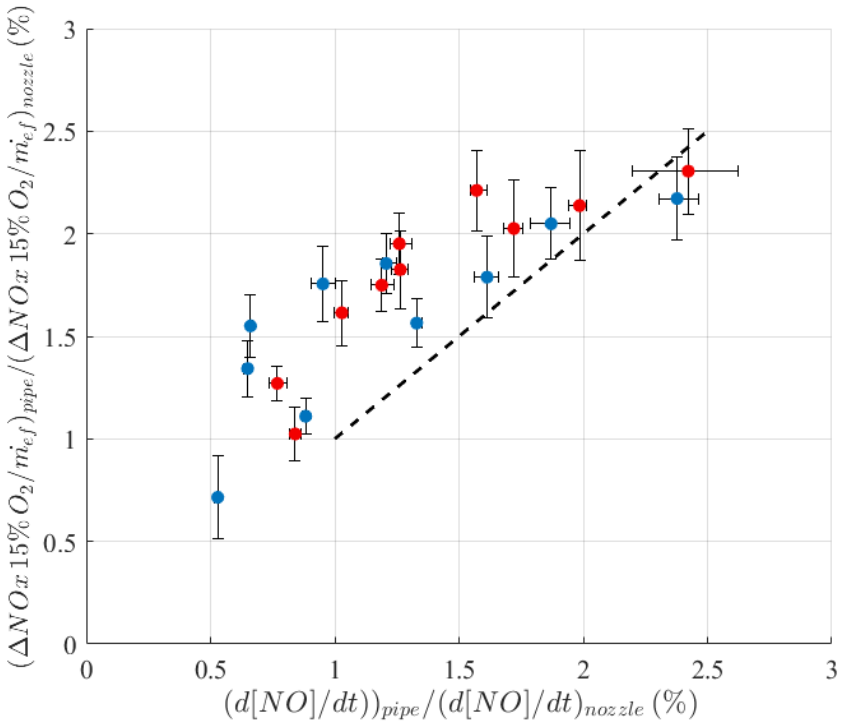

Figure 53 – Fraction of NOx production from reacting jets with pipe geometry compared to reacting jets with nozzle geometry as a function of the associated percentage change in NO production rate.

From the data in Figure 53 it is apparent that the pipe geometry results in higher NOx emissions compared to the nozzle cases. In addition this increase in NOx correlates with increases in NO production rates, supporting the hypothesis that the increased SLV growth

rates, and reduced mixing length scales, induce a reduction in ϕ_{Flame}. However, several cases experience little increase in production rate or even a decrease in production rates but still observe and increase in NOx emissions. This suggests that the nozzle geometry is indeed inducing high post-flame dilution rates and that ϕ_{Flame} reduction only accounts for a portion of the observed NOx reduction.

5.3.3.3 Correlation of NOx Emissions to NO Production Rates for Premixed Jets

The key hypothesis that this section seeks to test is whether NOx emissions are dominated by average pre-flame mixing rates. To this end, Figure 54 plots the NOx emissions of reacting jets for the investigated parameter space utilizing the nozzle geometry as a function of an effective NO production rate based on Equation 16. The NOx emissions are normalized by the effective fuel mass flowrate of the jet ($\dot{m}_{ef}$) as in Section 5.2, and the NO production rate is an average rate across all locations of all instantaneous flame edges for a given data point. The data is indicated per Table 5. In addition the associated uncertainty in the NOx measurement and the uncertainty in the NO production rate are indicated with error bars.

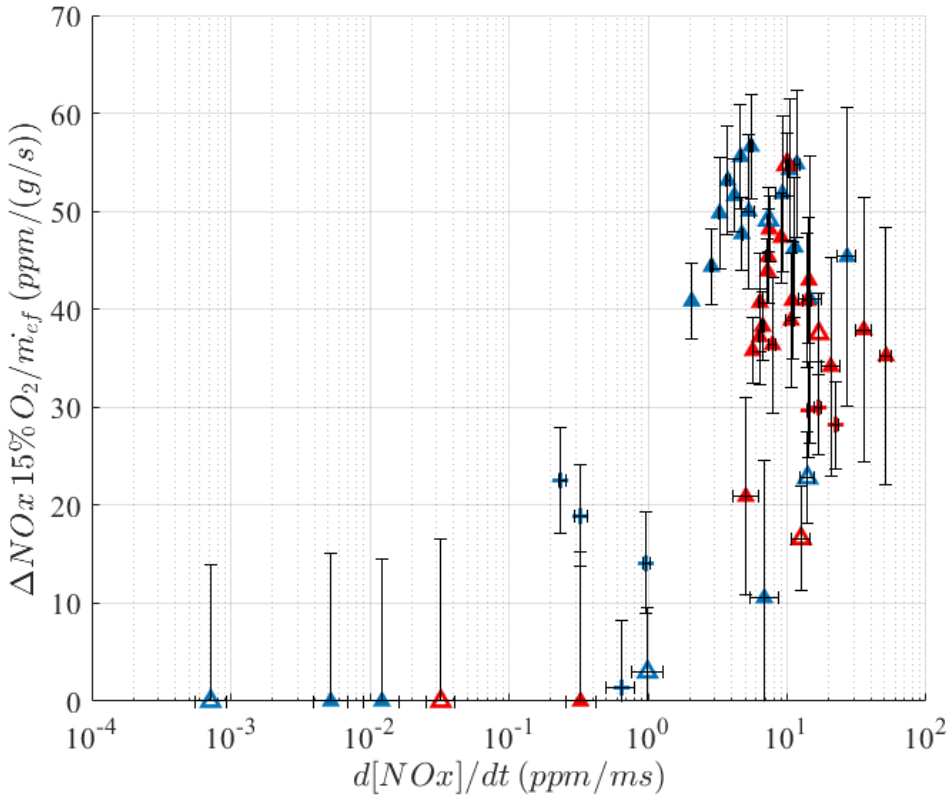

Figure 54 – Normalized RJICF NOx production as a function of estimated thermal NO production rates for all nozzle geometry data at constant crossflow conditions of ϕ_{XF} = 0.45 and ϕ_{XF} = 0.50.

Several key observations can be made from Figure 54. First, there is a clear relationship between the reacting jet NOx emissions and the thermal NO production rate, strongly supporting the hypothesis that the initial temperature determined by ϕ_{Flame} is a key driver of NOx production. Second, there appears to be a threshold below which NOx becomes negligible. It is possible that this cutoff is due to the sensitivity of the gas analyzer and that given a more precise means of measuring the emissions, the trend would remain monotonic. Finally, when focusing on the unforced cases (undoped and $J \leq 20$) the production rates tend to cluster either below the threshold for detected emissions or at high

production rates of roughly equal value that is associated with the whole range of high NOx emissions data. This indicates that time averaged ϕ_{Flame} considerations are capable of distinguishing whether a low or high NOx situation will result from the RJICF, but is not sufficient to accurately predict the NOx emissions in cases where these levels are high.

Several potential sources exist for the lack of correlation between the calculated NO production rates and the NOx emissions within the high NOx region of the parameter space. First, the underlying assumptions in f calculations might be overly restrictive. Second, reactant mass fluxes / consumption rates most likely vary across the flame edge. This would impact how different portions of the flame contribute to the averaged NO production rate. Third, is that instantaneous variation is significant and intermittency in NO production rates can be significant. Finally, as identified in Sections 5.3.3.1 and 5.3.3.2 it is likely that the sensitivity to post-flame dilution rate remains significant in comparison to the sensitivity to ϕ_{Flame}. In summary, while time averaged ϕ_{Flame} considerations are certainly a key parameter in RJICF production other effects (most likely post-flame dilution rates, or internal intermittency of NO production) are significant as well.

CHAPTER 6. LARGE EDDY SIMULATION METHODOLOGY

This chapter describes the methodology employed in the implementation of Large Eddy Simulations of reacting jets in cross flow. The numerical tool used is the multi-block, multi-physics code named LESLIE (large eddy simulation code with the linear eddy model), which in its latest release version used here (GTR 2.3.3) is capable of employing an adaptive mesh refinement (AMR) technique [66]. AMR allows for computationally inexpensive simulations and thus enables parametric studies of the system with short turn-around times, such that the effect of design parameter changes can be evaluated quickly. The capabilities of the software are constantly extended in the Computational Combustion Laboratory (CCL) at Georgia Tech.

6.1 Problem Setup

Two experimental data points were selected to be replicated by the simulation. These two points were from the preliminary data set described in Section 4.2.1. A lee-stabilized reacting jet and a fully lifted reaction jet were selected. Both of the data points produced similar NOx levels, however the fully lifted point had a higher ΔT. This indicates that the fully lifted case was more efficient from an emissions standpoint. Table 6 shows the experimental parameters of the two data points being simulated.

Table 6 – Experimental parameters of simulated reacting jets

Data Point	J	ϕ_{jet}	ϕ_{XF}
Lee-stabilized	3.7	1.1	0.6
Fully Lifted	1.5	2.2	0.6

In order to achieve shorter turn-around times compared to those in early validation attempts (trajectory comparisons to published data for these validation runs are plotted in Figure 66 found in Appendix A.3), the experimental setup described in Section 4.1 was scaled to a smaller geometry but higher velocities, while keeping the Reynolds numbers of cross-flow and jet constant. This reduces the flow-through time of one convective flush through the domain and increases the accuracy of the solution, as the LES code used is designed for compressible high-speed flows [67]. Table 7 compares the relevant dimensions and velocities of the experiment and simulation for the lee-stabilized test case. A scaling factor of 3 was used. All other relevant quantities like *J*, and temperatures were kept constant across the scaling. Computation cost savings after the Reynolds scaling was applied were found to be a speed up in the turn-around times at a factor of 2.3 faster for the reacting case. Comparisons of the simulation to experimental flame images indicated that the scaling had not radically altered the relative position of the flame with regards to the jet and that a Damkohler based scaling was not necessary.

Table 7 – Dimensions of experiment and scaled simulation.

	Experiment	Simulation
d_j	12 mm	4 mm
Width (w)	63.5 mm	21.6 mm
Height (h)	114.3 mm	38 mm
Length (L)	-	80 mm
Pipe Length (L_p)	-	10 mm
u_j	17.3 m/s	51.9 m/s
u_∞	17.0 m/s	51.1 m/s

Figure 55 provides an illustration of the simulation boundaries and and how AMR is realized across the domain. It is important to note that the upstream boundary is 5.5 jet diameters upstream of the center of the jet.

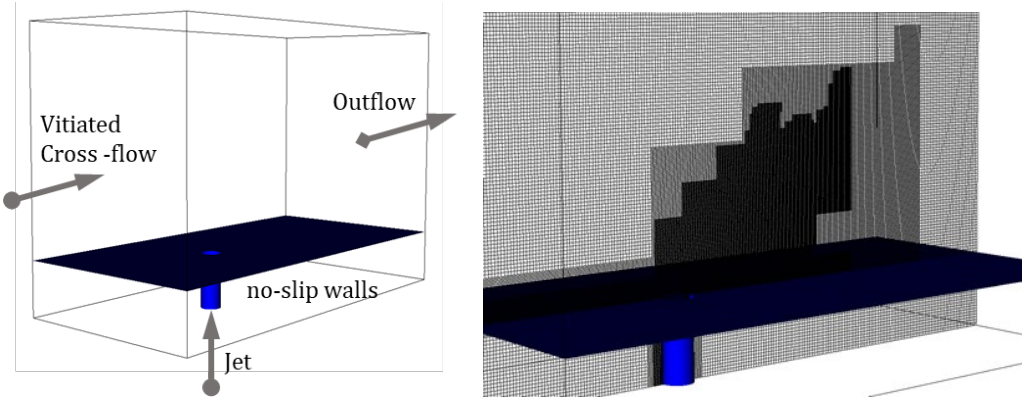

Figure 55 – Simulation boundaries (left) and grid implementation (right) for LES simulations of RJICF.

The incoming crossflow was set with experimentally determined velocity and temperature of 17.0 m/s and 1782K respectively. The composition was based off of equilibrium values for all reaction mechanism species (discussed further in Section 6.2) at the crossflow equivalence ratio of 0.6 with the exception of NO. NO levels were provided by experimental measurements of the crossflow.

Originally the walls were set as adiabatic boundary conditions, however, in the fully-lifted case the flame refused to detach from the wall. In order to more accurately reflect the heat loss through the wall, especially through the stainless steel pipe (the top of which is exposed to the flow in the experiment) an isothermal boundary was established. The isothermal boundary was a ring around the jet exit the thickness of the pipe and was set to a temperature of 1200K. This led to a total of three simulations that will be discussed in CHAPTER 7: the lee-stabilized test point with full adiabatic wall, the lee-stabilized test point with the isothermal ring, and the fully lifted test point with the isothermal ring.

6.2 Chemical Reaction Mechanism

The reaction mechanism selected for the simulation is the detailed methane oxidation mechanism including NOx as developed by Sung *et al* [68]. This reduced mechanism takes into account the Zeldovich (thermal) as well as Fenimore (prompt) NO formation pathways while using 19 species and 15 steps. Included species are NO, HCN, NH_3, H_2, H, O_2, OH, H_2O, HO_2, H_2O_2, CH_3, CH_4, CO, CO_2, CH_2O, C_2H_2, C_2H_4, C_2H_6 and N_2. An extensive mechanism analysis with regards to ignition delay, laminar flame speed, laminar flame

thickness, extinction strain rate, and species composition was performed. The results are shown in Appendix A.3, beginning with Figure 67.

CHAPTER 7. LARGE EDDY SIMULATION RESULTS

This chapter discusses the findings from the simulations conducted as part of this project, the methodology for which is outlined in CHAPTER 6.

7.1 Reacting Jet with Adiabatic Walls

Figure 56 displays an instantaneous mixture fraction field for the simulation of a reacting jet with $\phi_{jet} = 1.1$ and $J = 3.7$. Figure 56 also includes overlays of heat release rate as well as dashed white contour that corresponds to the stoichiometric mixture fraction. Both a jet center x-y plane and a x-z plane at a height of 0.8 jet diameters are included. The flame shown in Figure 56 as the highest level of heat release contour is located just outside of the stochiometric mixture fraction in the lee of the jet. The flame is seen to be firmly attached to the wall, most likely due to the adiabatic nature of the boundary in the simulation. In addition to its position in the lee of the jet, the flame can be observed to spread outwards from the lee downstream of the jet as well as to spread through the vortical structures after the pinch point of the jet to consume the reactants within them.

Figure 57 is similar to Figure 56 but plots a field of CH_4 reaction rate with overlays of heat release. Figure 57 confirms that the majority of methane consumption occurs in these high heat release regions as anticipated. Similar figures that plot the reaction rates for H_2, O_2 and CO can be found in Appendix A.4. NO reaction rates are plotted in Figure 58

with an overlay of temperature as opposed to heat release. In the wake of the jet, post flame a large region of elevated temperatures and NO production rates is observable.

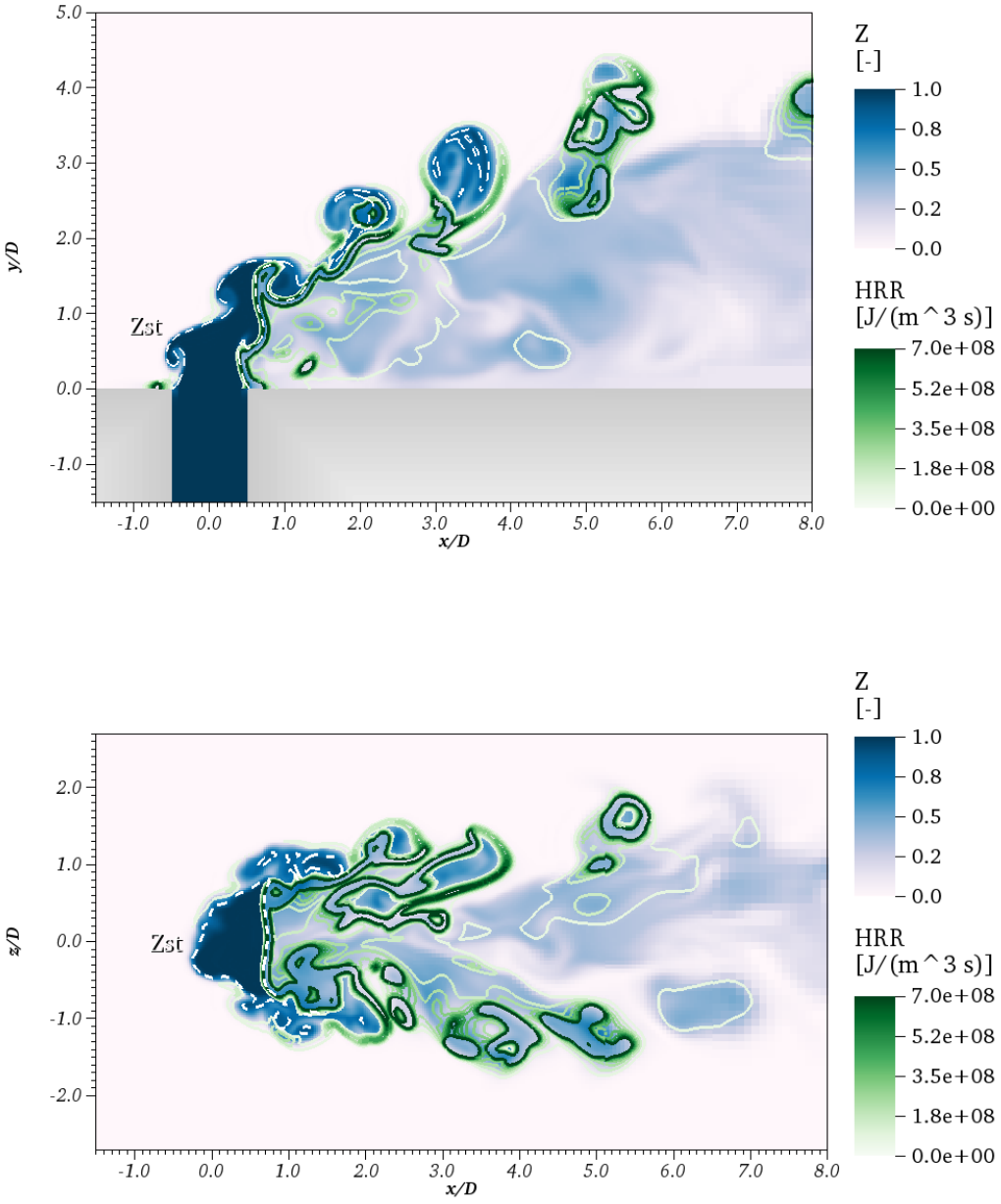

Figure 56 – Jet center-plane (top) and y/D = 0.8 x-z plane (bottom) showing mixture fraction field with overlay of heat release rate for simulation of a reacting jet in crossflow with ϕ_{jet} = 1.1 and J=3.7 and adiabatic wall boundary condition.

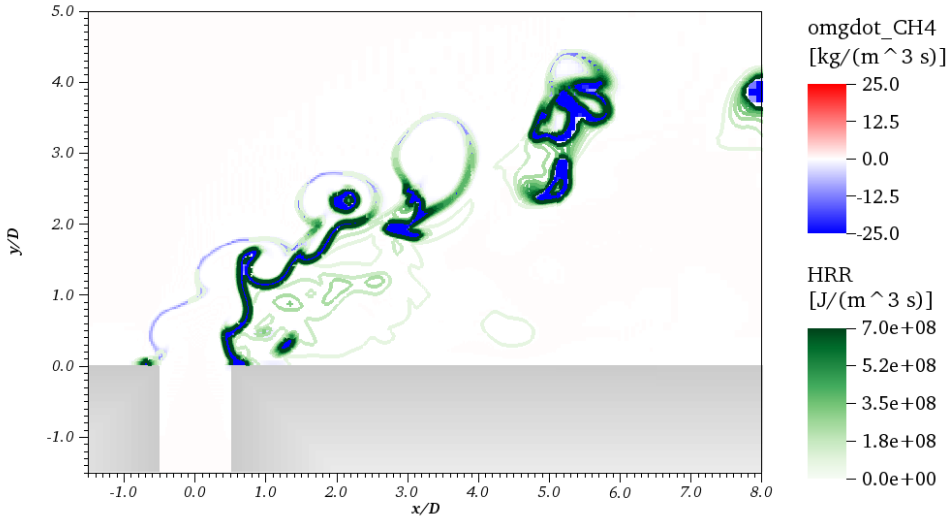

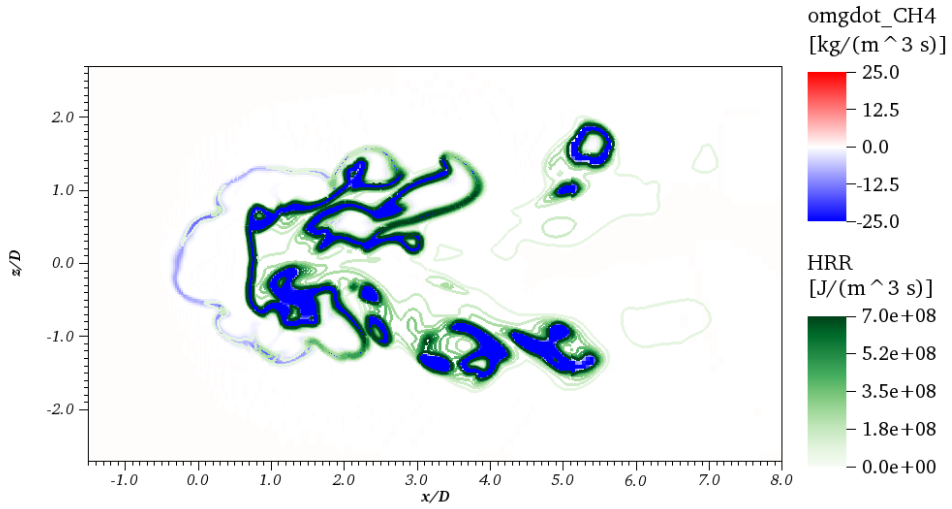

Figure 57 – Jet center-plane (top) and y/D = 0.8 x-z plane (bottom) showing CH4 reaction rate with overlay of heat release rate for simulation of a reacting jet in crossflow with ϕ_{jet} = 1.1 and J=3.7 and adiabatic wall boundary condition.

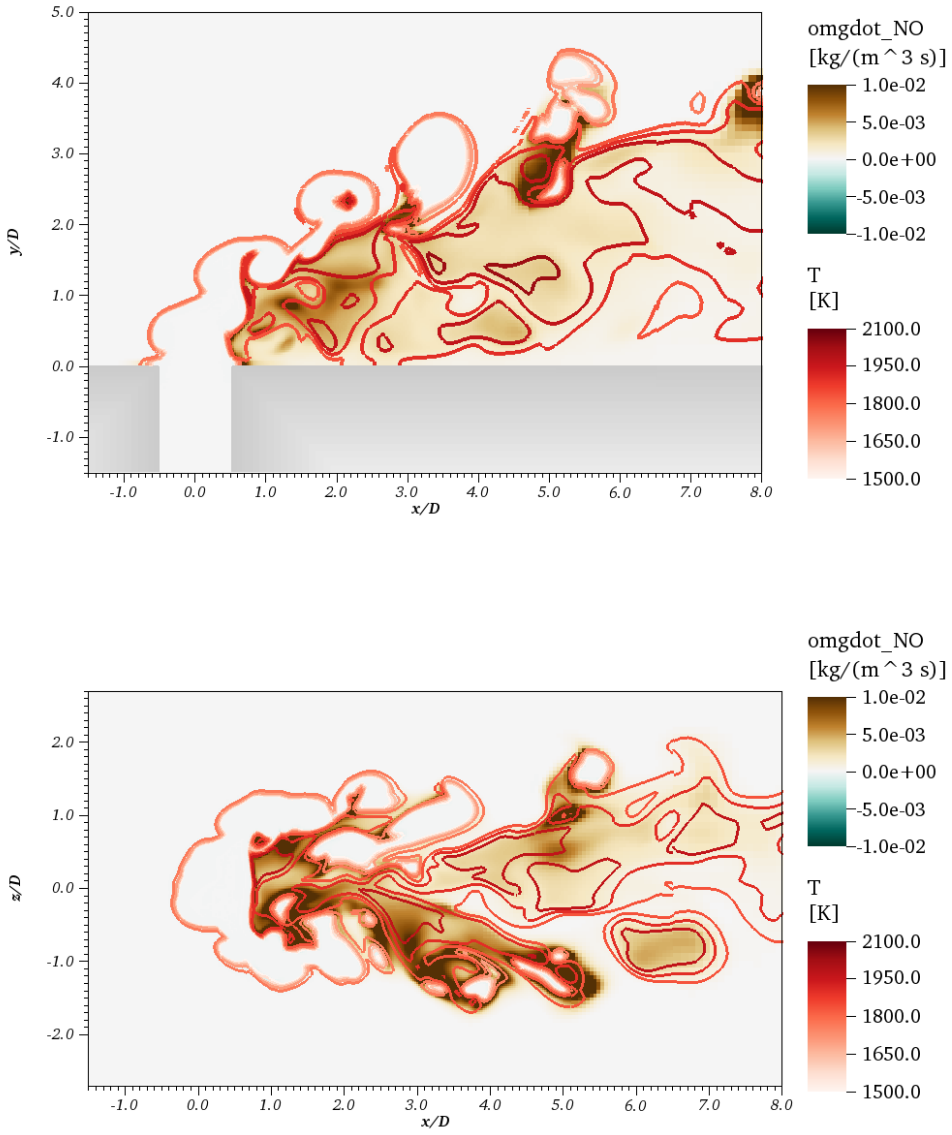

Figure 58 – Jet center-plane (top) and y/D = 0.8 x-z plane (bottom) showing NO reaction rate with overlay of temperature rate for simulation of a reacting jet in crossflow with ϕ_{jet} = 1.1 and J=3.7 and adiabatic wall boundary condition.

In the instance of the fully attached flame shown in the figures of this section, it is observable that almost all material that travels into the lee of the jet passes through the

flame front and is therefore at highly elevated temperatures. NO production is naturally high throughout this region.

7.2 Reacting Jet with Isothermal Wall in Vicinity of Jet Exit

The simulation results presented in Section 7.1 indicated a fully attached flame in the lee of the jet, which was not observed experimentally as discussed in CHAPTER 5. All jets observed experimentally were either lee-stabilized or lifted. This section presents results from a simulation that includes an isothermal ring at the base of the jet to reflect heat loss via conduction through the jet pipe. Figure 59 displays an instantaneous mixture fraction field for the simulation of a reacting jet with $\phi_{jet} = 1.1$ and $J = 3.7$. Figure 59 also includes overlays of heat release rate as well as dashed white contour that corresponds to the stoichiometric mixture fraction. Both a jet center x-y plane and a x-z plane at a height of 0.8 jet diameters are included.

Similarly to the flame discussed in Section 7.1, the flame exists just outside of the stochiometric mixture fraction and extends outwards to the sides and consumes vortical structures past the pinch point. As in Section 7.1, plots of CH_4 reaction rate (shown in Figure 60) confirm that methane consumption and high heat release rate coincide. However in departure from the behavior of the previously discussed flame, the low temperature near the jet exit forces the base of the flame to lift from the flame and stabilize in a manner similar to that observed experimentally and discussed in CHAPTER 5. The impact of this

small degree of flame lifting is observable in Figure 61 which shows the reaction rate of NO with overlays of temperature.

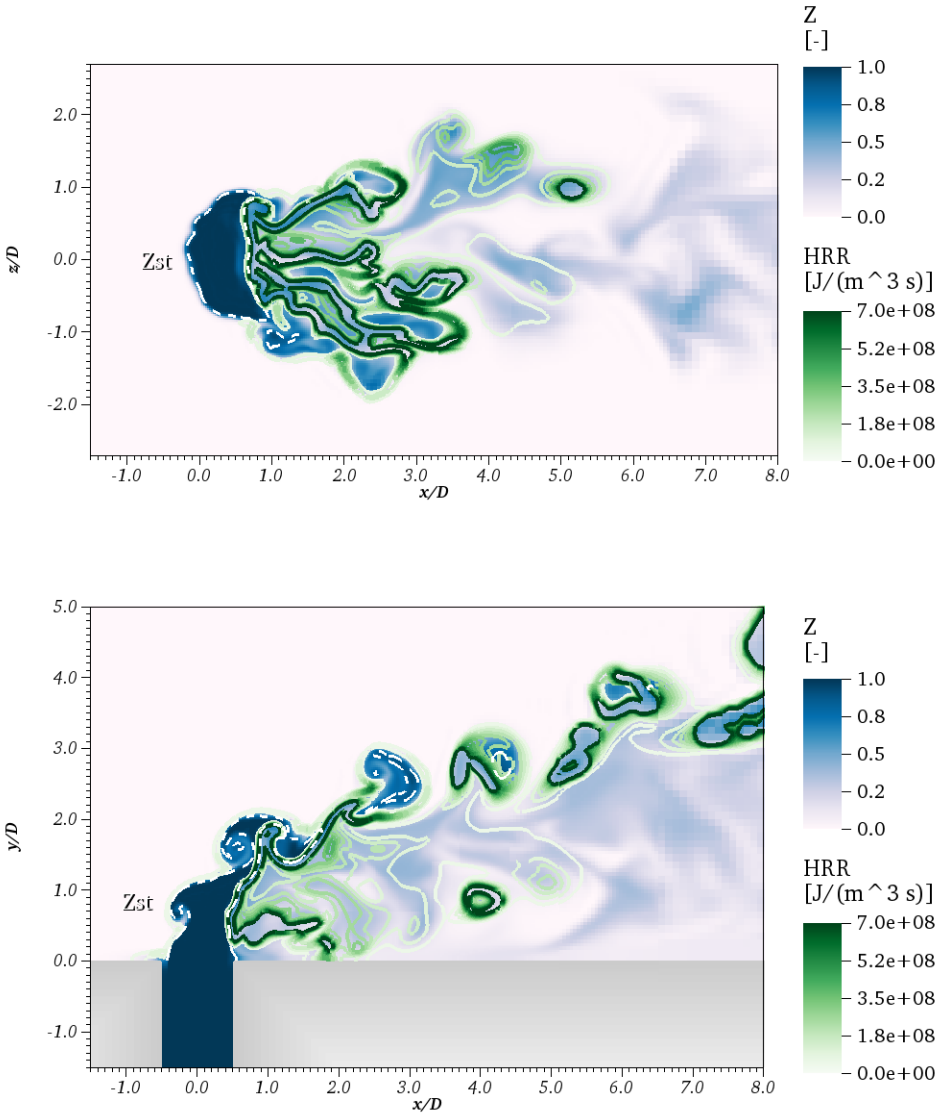

Figure 59 – Jet center-plane (top) and y/D = 0.8 x-z plane (bottom) showing mixture fraction with overlay of heat release rate for simulation of a reacting jet in crossflow with ϕ_{jet} = 1.1 and J=3.7 and isothermal wall boundary condition.

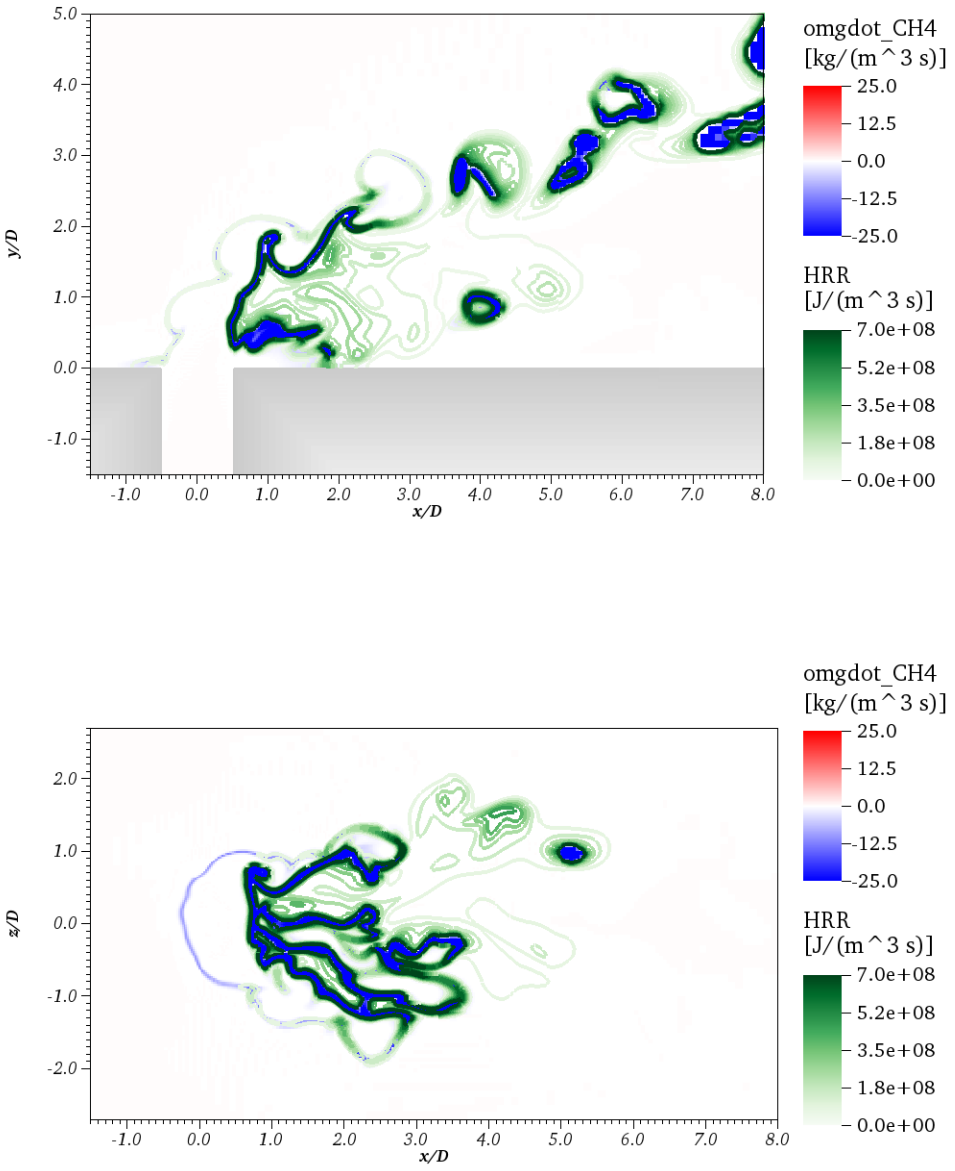

Figure 60 – Jet center-plane (top) and y/D = 0.8 x-z plane (bottom) showing CH4 reaction rate with overlay of heat release rate for simulation of a reacting jet in crossflow with ϕ_{jet} = 1.1 and J=3.7 and isothermal wall boundary condition.

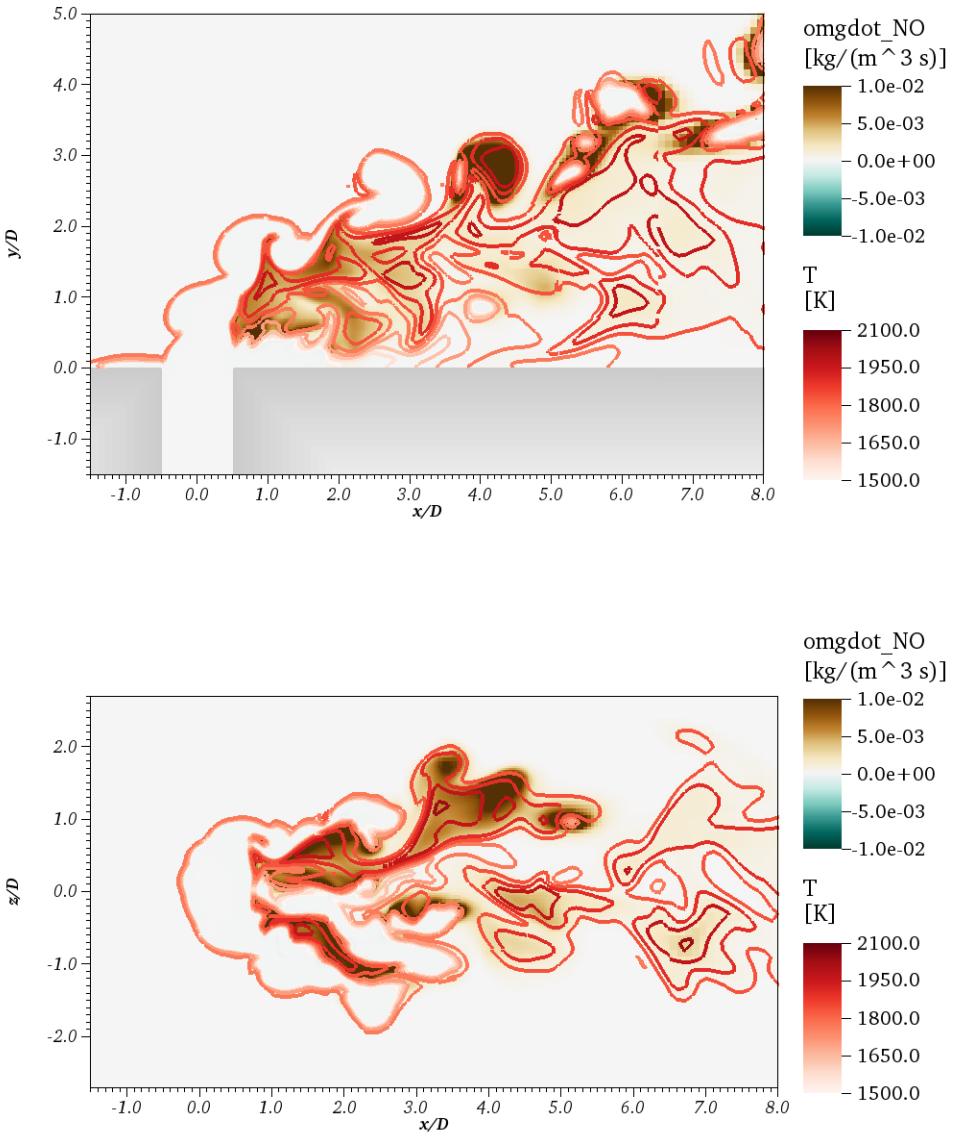

Figure 61 – Jet center-plane (top) and y/D = 0.8 x-z plane (bottom) showing NO reaction rate with overlay of temperature for simulation of a reacting jet in crossflow with ϕ_{jet} = 1.1 and J=3.7 and isothermal wall boundary condition.

Figure 61 shows that the lifting of the flame from the wall allows for penetration of cooler crossflow into the leeward region of the jet. As a result, the extent of the high

temperature wake region of products is significantly reduced which in turn reduces the region of elevated NO production. The large impact of this small degree of lifting further reinforces the importance of crossflow entrainment in reducing NOx as discussed in CHAPTER 3 as well as the importance of flame lifting in achieving this in a RJICF as discussed in CHAPTER 5.

7.3 Very Rich Reacting Jet with Isothermal Wall in Vicinity of Jet Exit

Figure 62 displays an instantaneous mixture fraction field for the simulation of a reacting jet with $\phi_{jet} = 2.2$ and $J = 1.5$. Figure 56 also includes overlays of heat release rate as well as dashed white contour that corresponds to the stoichiometric mixture fraction. Both a jet center x-y plane and a x-z plane at a height of 0.8 jet diameters are included. It is important to note that this simulation uses the same boundary conditions as that presented in Section 7.2 and discussed in detail in CHAPTER 6, which includes an isothermal ring around the jet exit with the remainder of the wall as adiabatic.

In Figure 62 the flame is shown to have lifted downstream of the jet exit and is located once again in the vicinity of the stoichiometric mixture fraction. This finding strongly supports the discussion in Section 5.2.3 regarding equivalence ratio of combustion and the lifting of rich jets to achieve a preferred value of ϕ_{Flame}. As the flame was swept downstream in the simulation, however, it appears the adiabatic boundary layer downstream of the jet exit allowed the flame to reattach to the wall. This attachment induced a similar situation as the attached flame discussed Section 7.1 with regards to NO

production. This impact can be observed in the additional data from this simulation found in Appendix A.4.

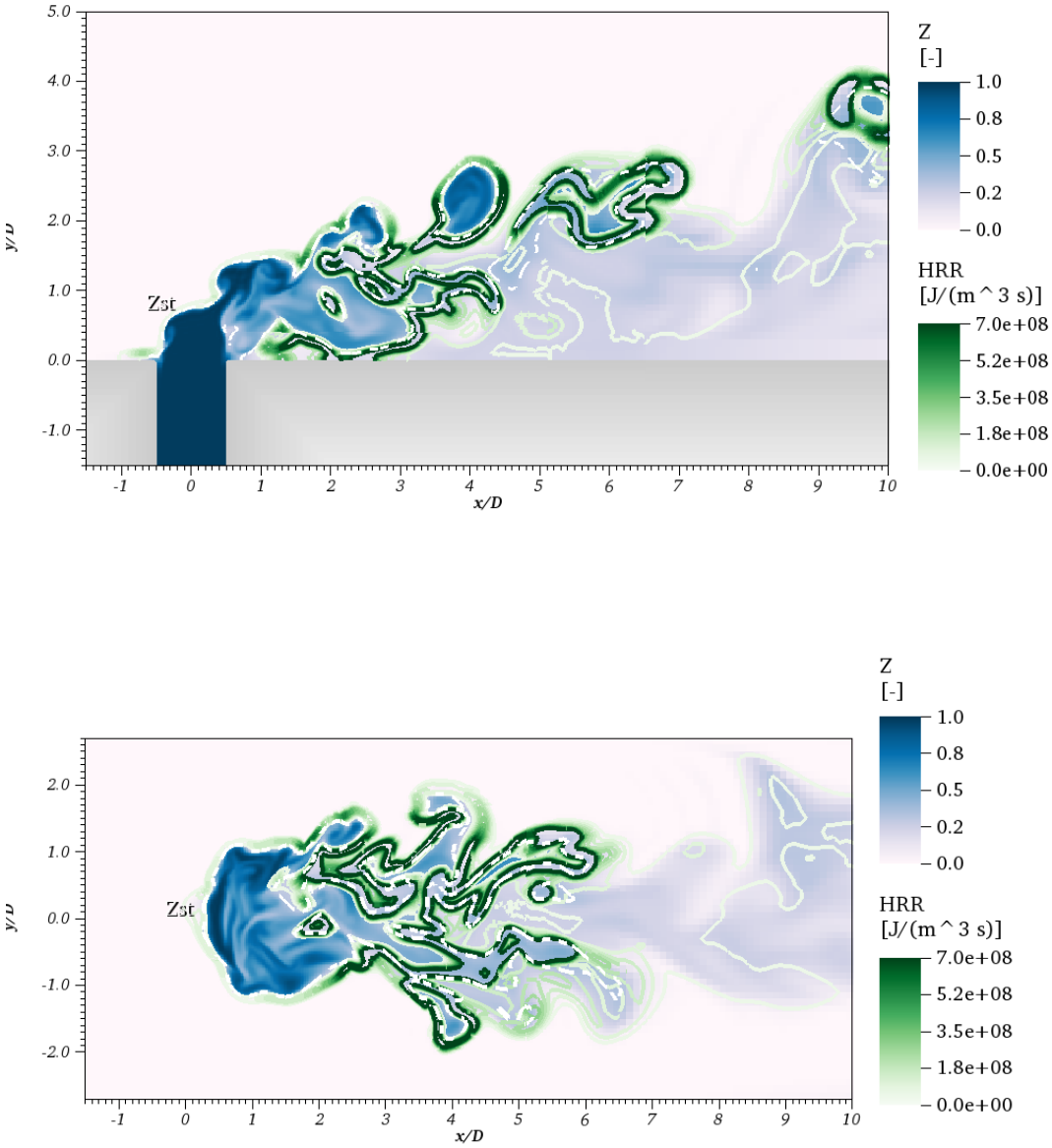

Figure 62 – Jet center-plane (top) and y/D = 0.8 x-z plane (bottom) showing mixture fraction with overlay of heat release rate for simulation of a reacting jet in crossflow with ϕ_{jet} = 2.2 and J=1.5 and isothermal wall boundary condition.

CHAPTER 8. CONCLUSIONS AND RECOMMENDATIONS

The work presented in this report was motivated by the challenge of achieving low nitrogen oxide emissions in high temperature combustion devices that are required to operate over a wide range of load conditions. Specifically, this work seeks to further the understanding of pollutant formation in the complex reacting flow field created by a reacting jet in a vitiated crossflow. The interest is driven by its potential as a means to reduce NOx at high temperature via axial staging. The primary objectives of this study were to identify the governing parameters of NOx production in the RJICF flow field and to ascertain if any of these sensitivities are as significant as those previously identified in literature, namely ΔT. In pursuit of these objectives the NOx emissions of a wide parameter space of premixed ethane/air, methane/air, and ethane/methane/air jets were experimentally characterized. In addition, high speed optical diagnostics were utilized to determine flame position and stabilization behavior as well as the time averaged pre-flame mixture fraction field. This final chapter summarizes the key contributions of the presented work, and provides recommendations for future work in RJICF emissions characterization.

8.1 Summary of Findings

8.1.1 Summary of Reactor Model Findings

The CRN model studies produced several key findings for this project. The first is that the fundamental minimum NOx emissions for an AFS combustor is on the order of 1

ppm. This finding establishes the significant potential of stage combustion for enabling future generation of high temperature gas turbine combustors.

Further studies with a CRN model created to assess the impact of finite entrainment identified key architectural concepts that are necessary to achieve NO levels near the fundamental levels. First and foremost of these necessities is the rapid entrainment of the main flow into the secondary combustion zone. Restated, it is important for the secondary combustion to be distributed across the entirety of the main flow or at the very least to rapidly dilute the secondary combustion products. If the secondary fuel is consumed in a small region of the main flow, large NO production will occur.

Studies focused on the impact of a premixed secondary fluid stream indicate that the addition of air to the fuel stream in large quantities can assist in creating the beneficial environment necessary to create reduced NO emissions through axial staging.

8.1.2 Summary of Experimental Findings

The first major contribution of the experimental work is to confirm the dominant role that ΔT has in RJICF NOx production. This sensitivity had been previously identified in literature and is strongly supported by the data reported herein. A clear correlation between ΔNOx and ΔT (or $\Delta\phi$) was observed, with NOx emissions monotonically increasing with increasing ΔT.

Expanding upon what had been previously identified in the literature, the data presented in this work also establishes that NOx production in a RJICF varies significantly at constant ΔT or similar parameter (e.g. jet fuel mass flow or $\Delta\phi$). Emissions measurements in premixed reacting jets indicated that NOx production from a RJICF varies as much as 3x at constant ΔT. This finding serves as the second major contribution of the experimental work, and validates the need for investigation into the governing parameters and coupled physical processes involved.

The third major contribution of the experimental work iss a systematic characterization of the key sensitives of NOx production over a wide parameter space of premixed reacting jets. The envelope of investigation included both rich and lean jet equivalence ratios as well as different regimes of jet stability behavior: globally or convectively unstable. Great attention was paid to isolating each potential driver of NOx production. When ϕ_{jet} and LO were interdependent, the reacting jets grouped themselves into three regions of flame stabilization and NOx emissions behavior. The central region, in terms of ϕ_{jet}, was occupied by lee-stabilized flames. Jets with equivalence ratios that were more fuel lean ("lean lifted") and that were more fuel rich ("rich lifted") than those associated with lee-stabilized flames were fully lifted. The emissions of fully lifted flames were largely invariant with ϕ_{jet} or LO, but were grouped as either producing negligible or high levels of NOx emissions. Negligible NOx production was associated with "lean lifted" flames, and high NOx production was found in the "rich lifted" cases. The lee-stabilized flames produced intermediate NOx emissions and exhibited a dependency on ϕ_{jet} that

plateaued at NOx levels similar to those of the "rich lifted" flames. When *LO* was increased at constant ϕ_{jet}, either as a consequence of data with high momentum flux ratio or via the doping of the jet fuel mixture with methane to retard ignition kinetics, NOx production was shown to decrease in every instance. Finally, the impact on shear layer growth rate/near-field mixing rates was examined via the selection of exit velocity profile. Data was acquired for a fully developed jet exit boundary layer and a top hat jet exit velocity profile. The more rapid near-field mixing associated with the top hat exit profile [19, 21] was shown to produce less NOx than the fully developed boundary layer.

The final major contribution of the experimental work is to establish the equivalence ratio of combustion, ϕ_{Flame}, as a 1st order parameter driving NOx production in RJICF. Based on the interdependencies observed between jet parameters, it was hypothesized that ϕ_{jet}, *LO*, and near-field mixing rates were functional parameters of ϕ_{Flame}, and that ϕ_{Flame} strongly correlated with NOx production in RJICF. This hypothesis was tested by calculating NO production rates based on the impact that ϕ_{Flame} would have on flame temperature and equilibrium [O]. The local combustion conditions were determined by the overlay of instantaneous flame edges onto a time averaged mixture fraction field. The mixture fraction field was experimentally determined using Mie scattering images of ceramic particles seeded into the jet fluid stream. The investigation corroborated ϕ_{Flame} as a significant factor in RJICF NOx production. However, in the region where ϕ_{Flame} indicated high NO production (and where the data showed high NOx levels), there existed a significant variation in NOx levels at near constant *d[NO]/dt*. Post-flame dilution/mixing

rates, ϕ_{Flame} intermittency, and variable reactant consumption rates along the flame are all potential causes for the observed variation in NOx.

The work indicates an avenue for NOx mitigation in the form of fully lifted reacting jets with rapid pre-flame and post-flame mixing rates, and perhaps more significantly underscores the necessity of this approach in achieving any kind of NOx benefit from the implementation of axial staging via a RJICF. The prospect of achieving the described flow field is challenging and raises additional questions that need to be investigated.

8.1.3 Summary of Simulation Findings

The major contribution of the large eddy simulations conducted as part of this project was to provide further evidence to support the hypotheses drawn from the experimental data discussed in CHAPTER 5 and Section 8.1.2. The simulations confirmed that the flame prefers to exist in a region with an equivalence ratio that corresponds to high flame temperatures and flame speeds. The simulation also demonstrated how critical the lifting of the flame is to allowing access of crossflow to the hot products in order to induce mixing and dilution.

8.2 Recommendations for Future Work

The work presented in this report provides a solid foundation for the understanding of NOx production in a premixed RJICF and also provides direction on the most advantageous approach to utilizing a RJICF for NOx mitigation. The realization of this

from an engineering perspective is very challenging as it asks combustor designers to stabilize a lean lifted flame in a high pressure and high temperature environment. Achieving such a difficult task will require even greater understanding of the governing physical processes and how they interact. To this end two separate avenues of investigation would prove very beneficial to the pursuit of this goal.

8.2.1 Investigation of Jet Parameter Impact on Post-Flame Mixing Rates

As mentioned in Section 8.1, a key finding of the work presented in this report is that post-flame dilution rates might have an impact on NOx production on the same order as ϕ_{Flame}. A central hypothesis is that the post-flame mixing is controlled by the CVP which in turn is impacted by the SLV growth rate; with the SLV growth rate a function of several parameters such as exit velocity profile, *J*, and flame position.

A follow-on investigation similar to that conducted to examine the local mixture fraction of combustion could be conducted with the aim of evaluating the impact of the varying jet parameters on the CVP strength and correlating that change with the measured NOx emissions. To be more specific, repeat the test parameter space described in Section 4.2.2 with the primary measurement being stereo-PIV of one or more transverse planes downstream of the jet exit where the CVP would be situated. Due to the CVP existing as a time averaged feature the PIV could be conducted at rates from 1 Hz up to 10 kHz based on equipment availability and still achieve the measurement objectives. Flame imaging would still remain a valuable measurement to verify similar flame position and stabilization

in reference to the emissions measurements. Such an investigation would not only provide insight into RJICF NOx formation, but also on the fundamental impact of flame position on major JICF vortical structures in premixed RJICF.

8.2.2 Investigation of Flame Stabilization Physics

The necessity to lift the flame in order to enable NOx reduction is a key finding from the work presented here. The work also identified some of the governing parameters (i.e. jet stoichiometry, near-field mixing rates, and crossflow temperature) that influenced flame lifting for the conditions and geometries that were investigated as part of the presented work. It is very clear, from those same investigations, that flame stabilization is multi-factorial and that changes in conditions such as heat flux through the test section floor, or elevated pressure could significantly alter lifting behaviour. A more comprehensive examination on the governing physics in flame stabilization of premixed reacting jets would provide valuable understanding needed to engineer the “lean lifted” flame essential for NOx mitigation.

This work could be started with the experimental facility in its current state. A much finer parameter sweep of jet parameters and crossflow conditions with the sole objective of investigating lifting behaviour could be undertaken and yield valuable results. Eventually however, modifications would have to be made to provide more control over factors such as wall heat flux, physical geometry, crossflow boundary layer thickness, and pressure. The implementation of high-speed laser diagnostics would be critical; especially

in the form of coupled PLIF and PIV measurements to investigate the role of flow strain rates in the stabilization of the flame within the JICF flow field. Comparisons between CH2O and OH PLIF could also provide valuable insight into stabilization mechanics. Considering the highly three-dimensional and asymmetric nature of the flow field tomographic measurements would also be of high value where possible.

Consideration of the significant impact that elevated pressure would have on flame lift off would have to be made. Practical axial staging systems will be operating in elevated pressure environments ranging from 15 – 25 atm with Reynolds numbers significantly higher than those associated with the presented work. Pressures of this magnitude would significantly accelerate kinetics, thereby reducing autoignition delays as well as impacting flame speeds. The change in these parameters will fundamentally alter how the flame stabilizes compared to the atmospheric condition. The increase in Reynolds number will alter crossflow/jet turbulent mixing as well, which will also impact flame stabilization location.

In light of the significance of pressure effects on flame stabilization it would be prudent to investigate the lifting behaviour of RJICF at elevated pressure. Such an approach will determine how the governing jet parameters and physical processes of flame stabilization identified in this and any follow-on work change under high pressure conditions.

In addition to examining the pressure dependence of flame stabilization, it would also be valuable to validate the use of alternate fuels as surrogates for methane at high pressure. Ethane for example has a significantly lower autoignition delay compared to methane. This property could be useful in simulating some of the effect of methane under pressure. If this approach could be validated for ethane or other highly kinetic hydrocarbons it would greatly enable the scalability of proposed atmospheric investigations to high pressure conditions.

Given the challenge represented in testing at elevated pressure and applying the level of diagnostic investigation discussed (both separately and especially in tandem), this is an area that is primed for the use of simulations. Large eddy simulations (LES) grounded in the data from the initial parameter sweep could provide greater control of relevant parameters without facility modifications, and enable investigation of the complex interacting physics without the need for extensive diagnostics.

In reality a combination of the two approaches will be required to further the understanding of this complex problem that has been proven as essential to successful implementation of NOx mitigation strategies utilizing a reacting jet in crossflow.

APPENDIX A. SUPPLEMENTAL FIGURES

This appendix provides supplemental figures for various Chapters of this report. Each chapter that requires supplemental figures has its own Section in this Appendix.

A.1 Supplemental Figures for CHAPTER 4

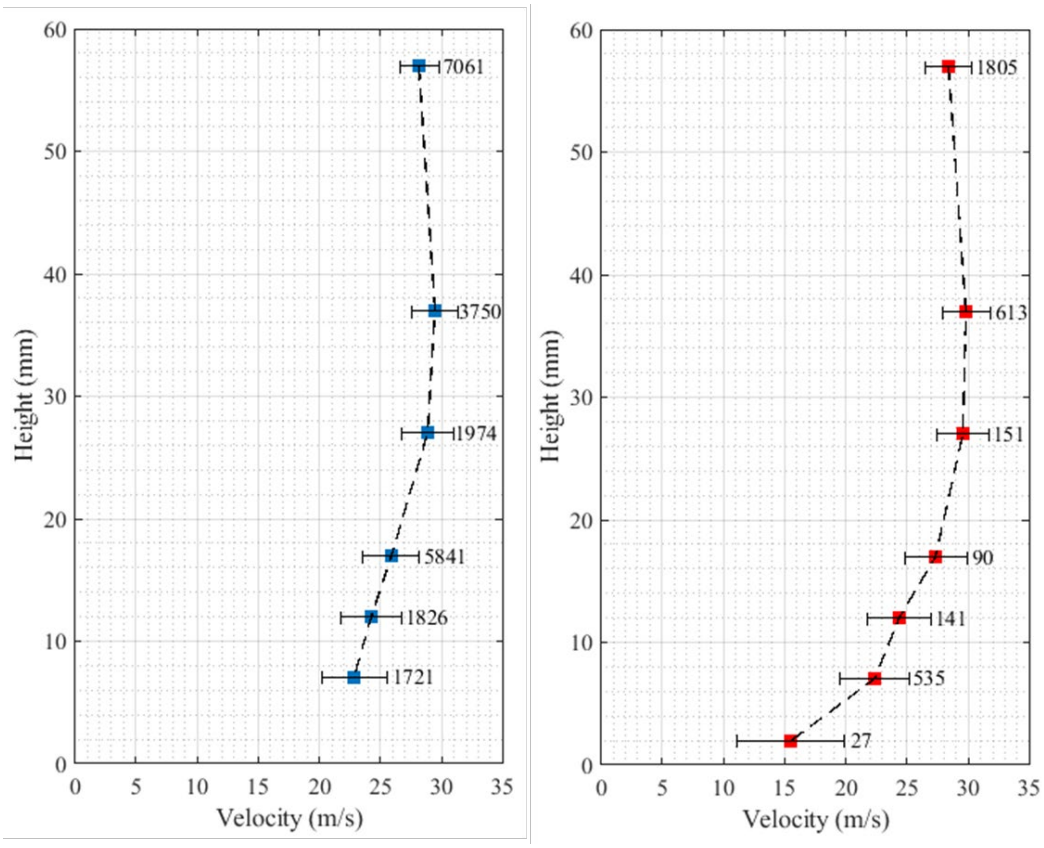

Figure 63 – Velocity profiles for vitiated crossflow with ϕ_{XF} = 0.45 (left) and ϕ_{XF} = 0.50 (right). Error bars indicate 99% confidence intervals and data counts for each point are displayed to the right of the error bars.

A.2 Supplemental Figures for CHAPTER 5

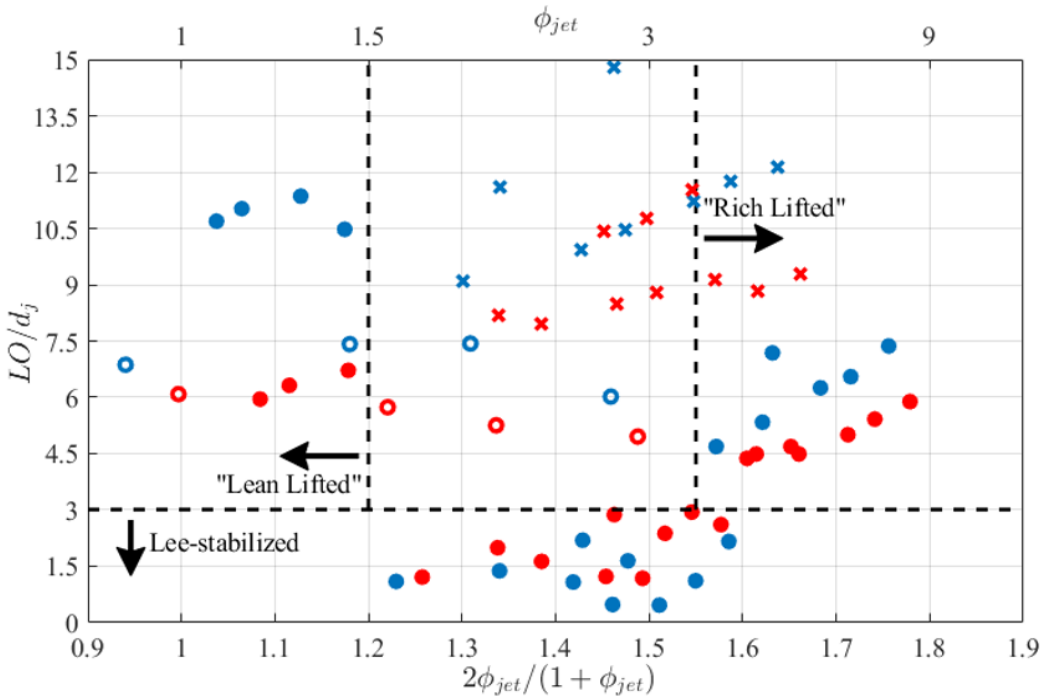

Figure 64 – Lift-off distance for all jets with pipe exit geometry (including J = 40 and methane doped) as a function of reduced equivalence ratio at constant crossflow conditions of ϕ_{XF} = 0.45 and ϕ_{XF} = 0.50.

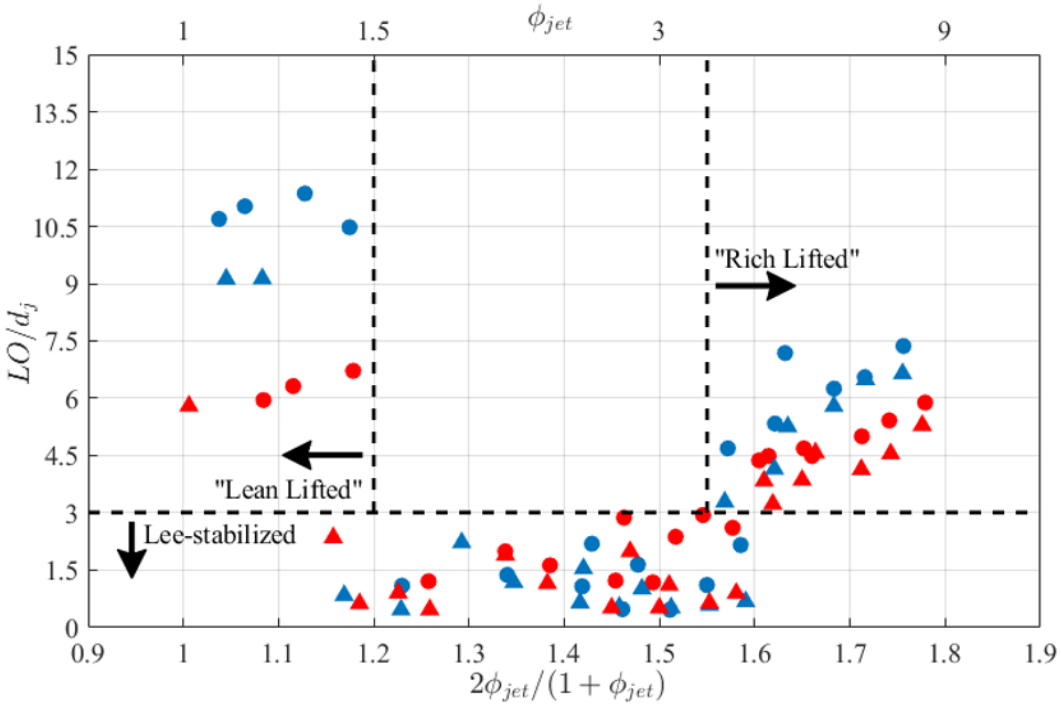

Figure 65 – Lift-off distance for jets with $J \leq 20$ as a function of reduced equivalence ratio for both pipe and nozzle jet geometries at constant crossflow conditions of ϕ_{XF} = 0.45 and ϕ_{XF} = 0.50.

A.3 Supplemental Figures for CHAPTER 6

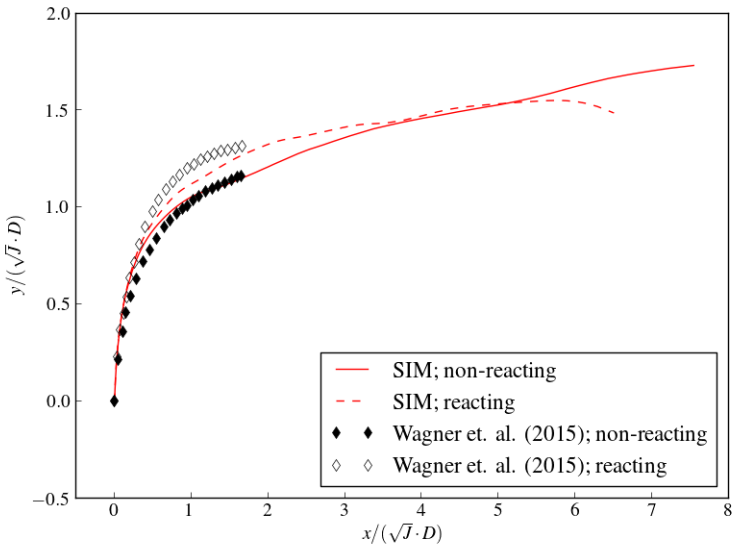

Figure 66 – Comparisons calculated jet trajectories compared to experimental data from Wagner et. al [23-25].

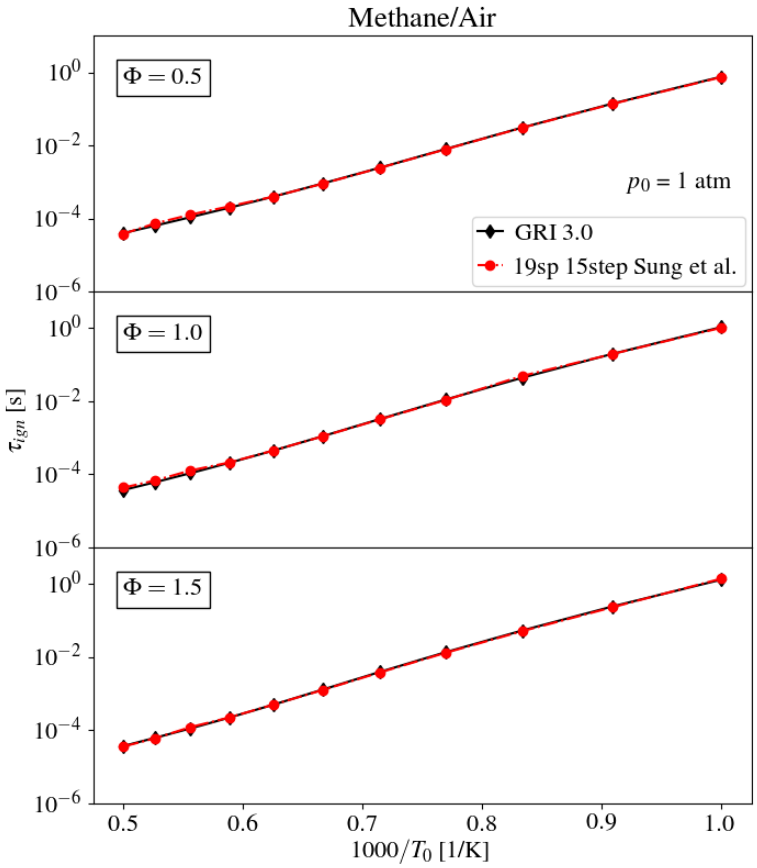

Figure 67 – Comparisons of ignition time calculated using selected chemical mechanism for simulation to those using GRI 3.0 at various equivalence ratios.

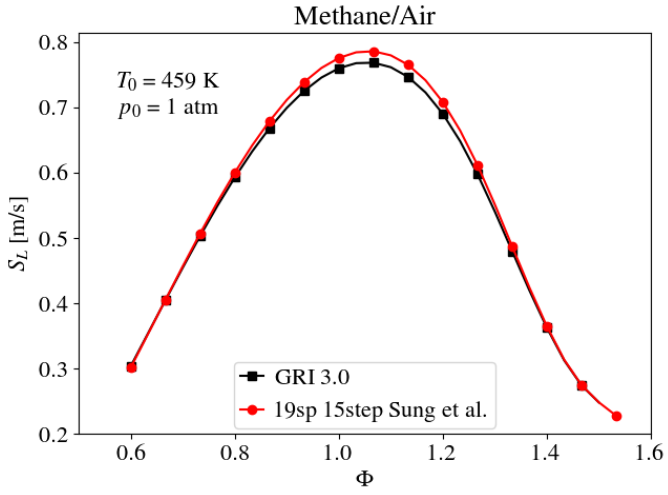

Figure 68 – Comparisons of flame speed calculated using selected chemical mechanism for simulation to those using GRI 3.0.

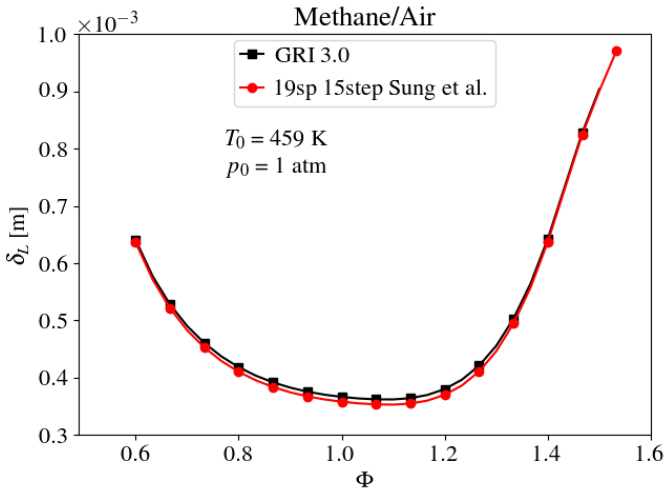

Figure 69 – Comparisons of flame thickness calculated using selected chemical mechanism for simulation to those using GRI 3.0.

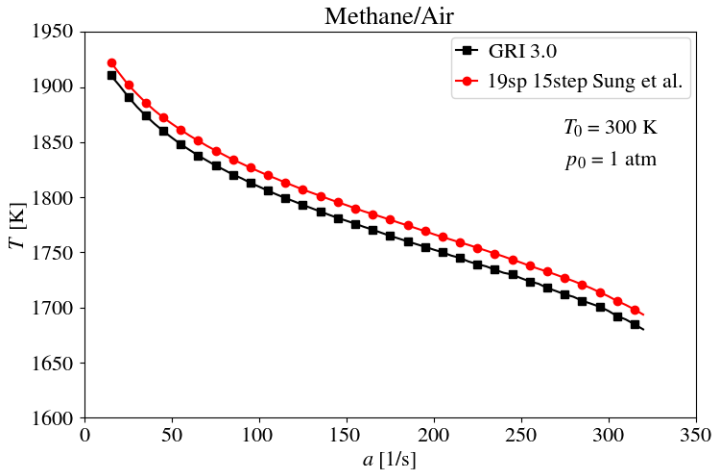

Figure 70 – Comparisons extinction strain rate calculated using selected chemical mechanism for simulation to those using GRI 3.0.

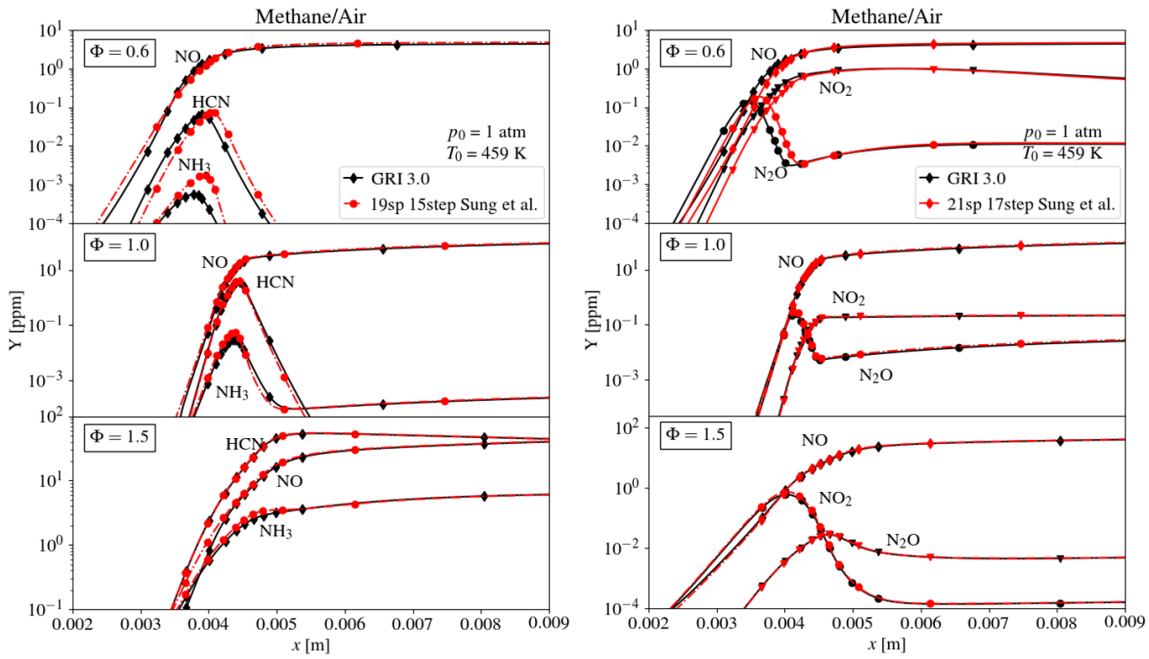

Figure 71 – Comparisons of species mass fractions calculated using selected chemical mechanism for simulation to those using GRI 3.0.

A.4 Supplemental Figures for CHAPTER 7

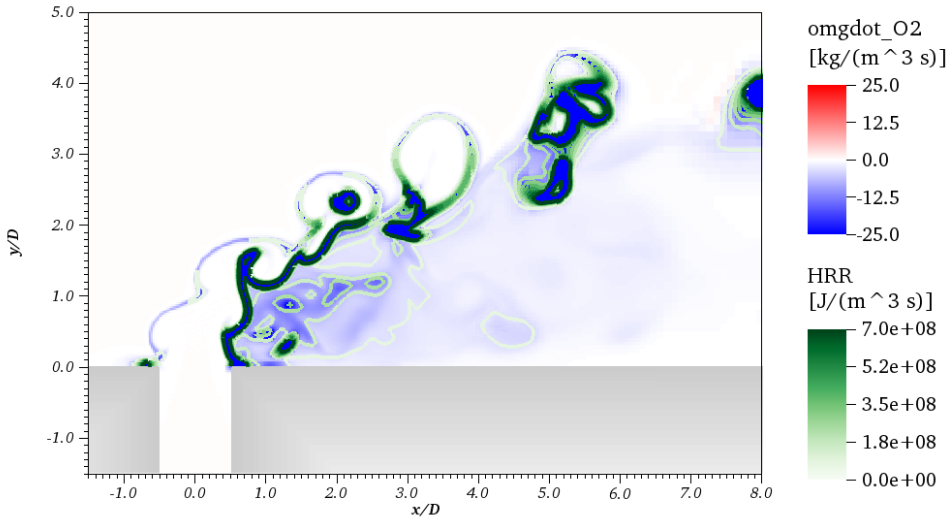

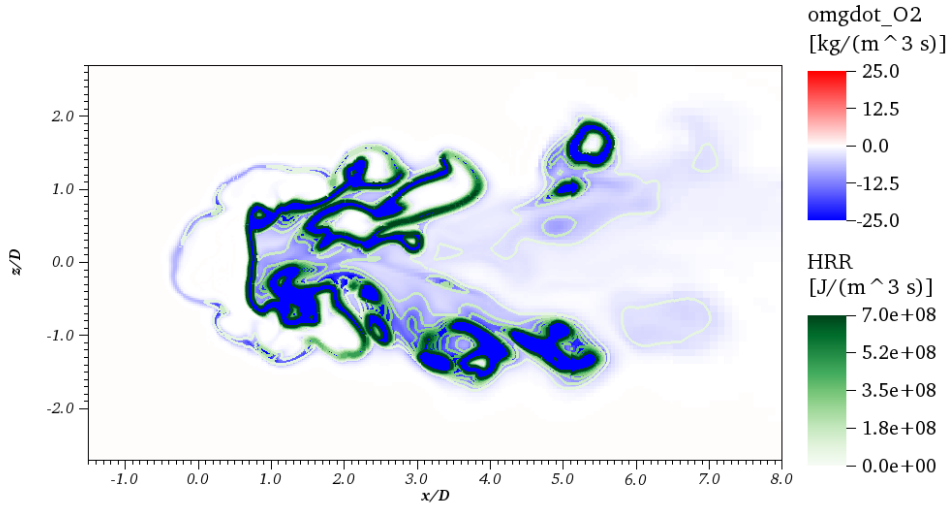

Figure 72 – Jet center-plane (top) and y/D = 0.8 x-z plane (bottom) showing O_2 reaction rate with overlay of heat release rate for simulation of a reacting jet in crossflow with ϕ_{jet} = 1.1 and J=3.7 and adiabatic wall boundary condition.

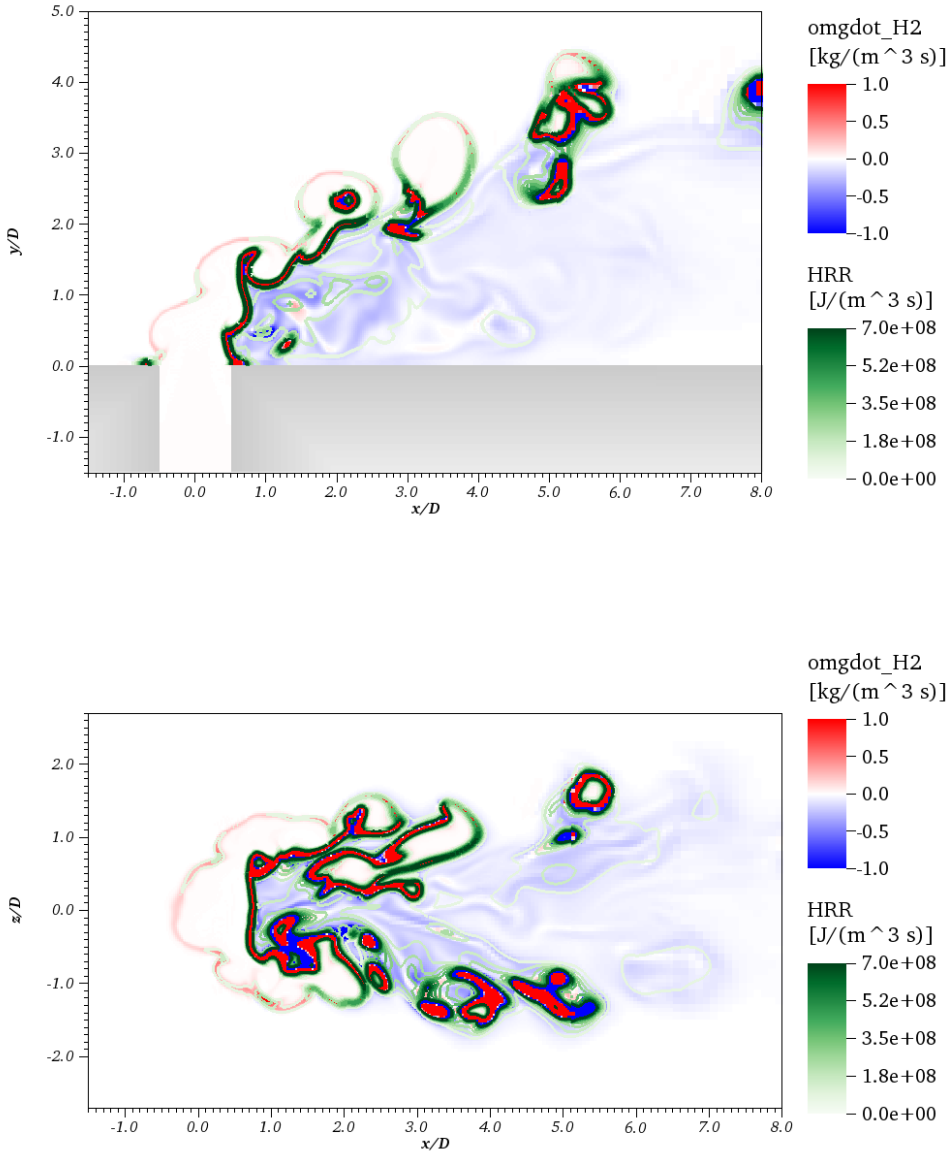

Figure 73 – Jet center-plane (top) and y/D = 0.8 x-z plane (bottom) showing H_2 reaction rate with overlay of heat release rate for simulation of a reacting jet in crossflow with ϕ_{jet} = 1.1 and J=3.7 and adiabatic wall boundary condition.

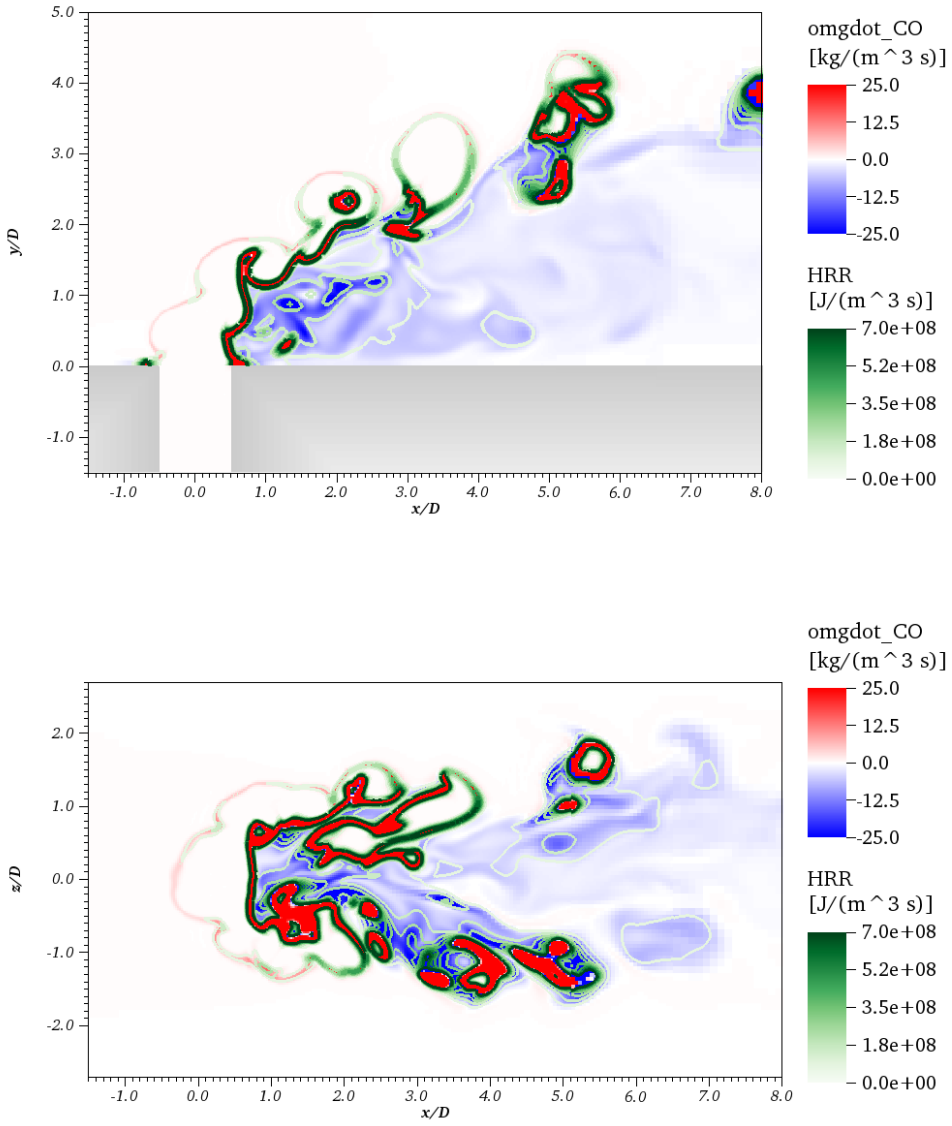

Figure 74 – Jet center-plane (top) and y/D = 0.8 x-z plane (bottom) showing CO reaction rate with overlay of heat release rate for simulation of a reacting jet in crossflow with ϕ_{jet} = 1.1 and J=3.7 and adiabatic wall boundary condition.

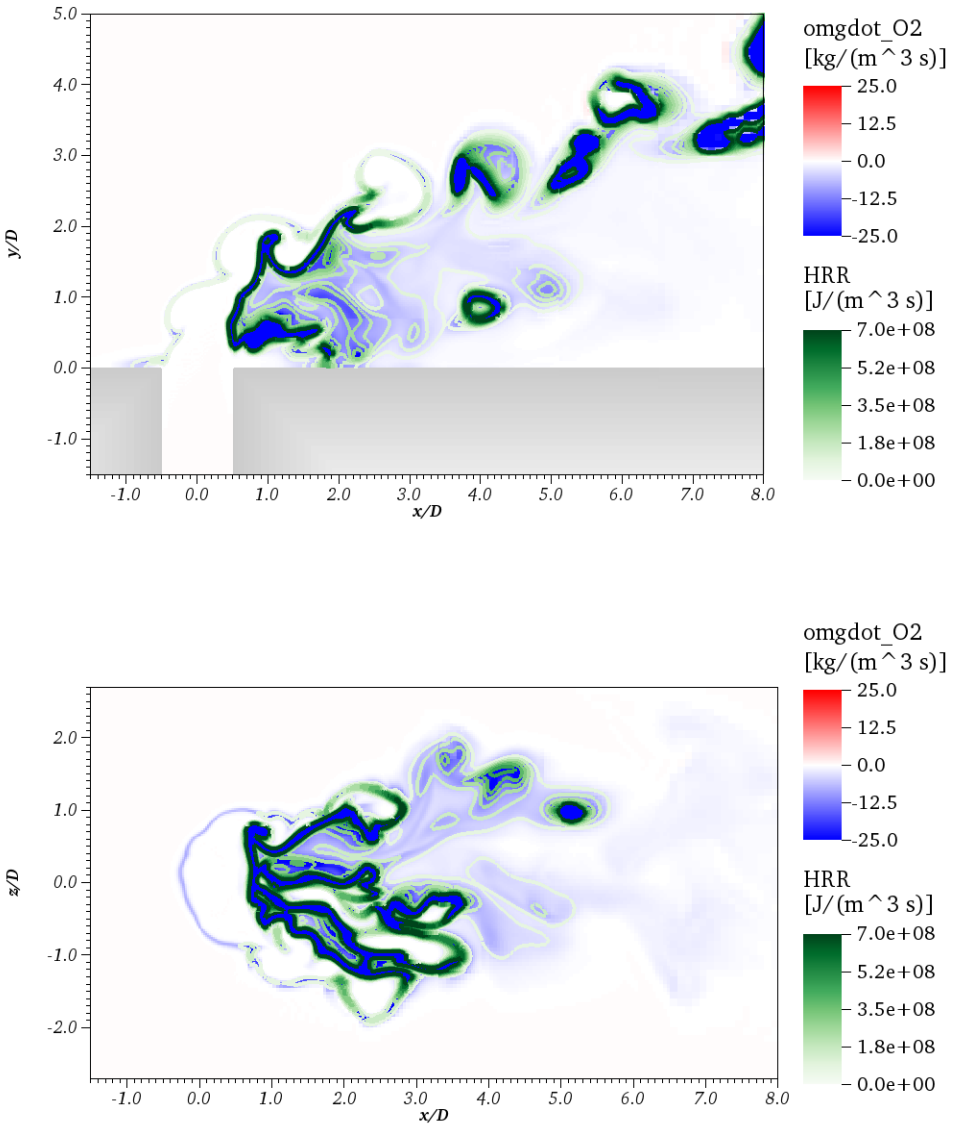

Figure 75 – Jet center-plane (top) and y/D = 0.8 x-z plane (bottom) showing O_2 reaction rate with overlay of heat release rate for simulation of a reacting jet in crossflow with ϕ_{jet} = 1.1 and J=3.7 and isothermal wall boundary condition.

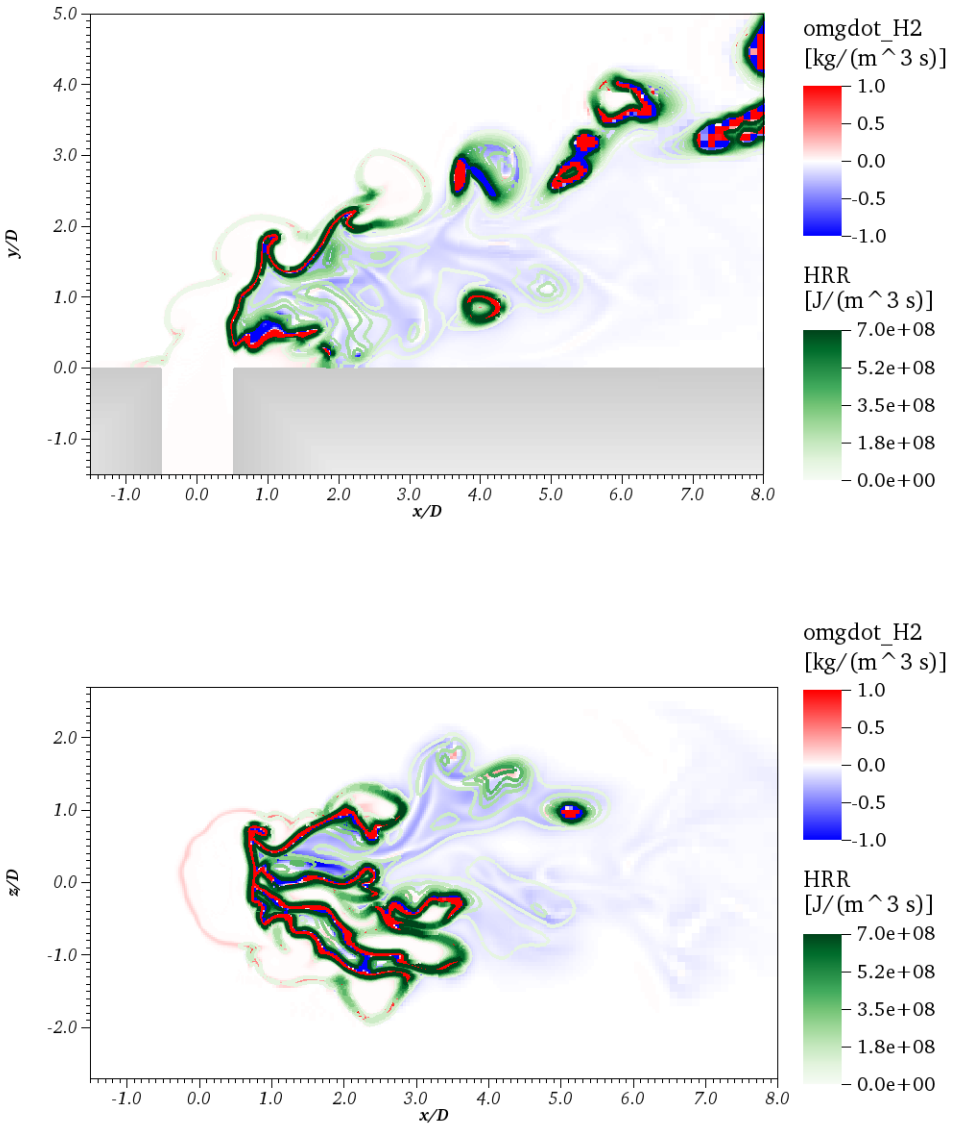

Figure 76 – Jet center-plane (top) and y/D = 0.8 x-z plane (bottom) showing H_2 reaction rate with overlay of heat release rate for simulation of a reacting jet in crossflow with ϕ_{jet} = 1.1 and J=3.7 and isothermal wall boundary condition.

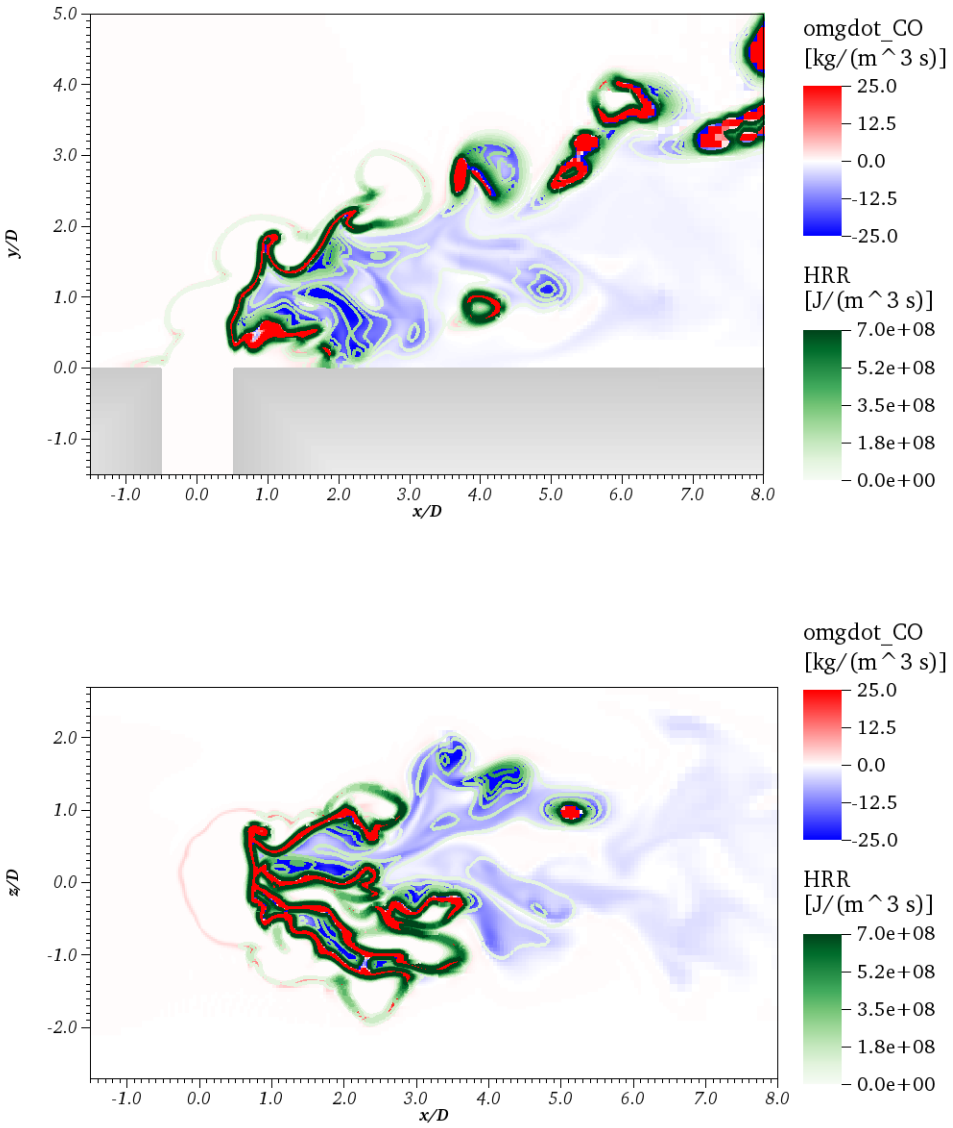

Figure 77 – Jet center-plane (top) and y/D = 0.8 x-z plane (bottom) showing CO reaction rate with overlay of heat release rate for simulation of a reacting jet in crossflow with ϕ_{jet} = 1.1 and J=3.7 and isothermal wall boundary condition.

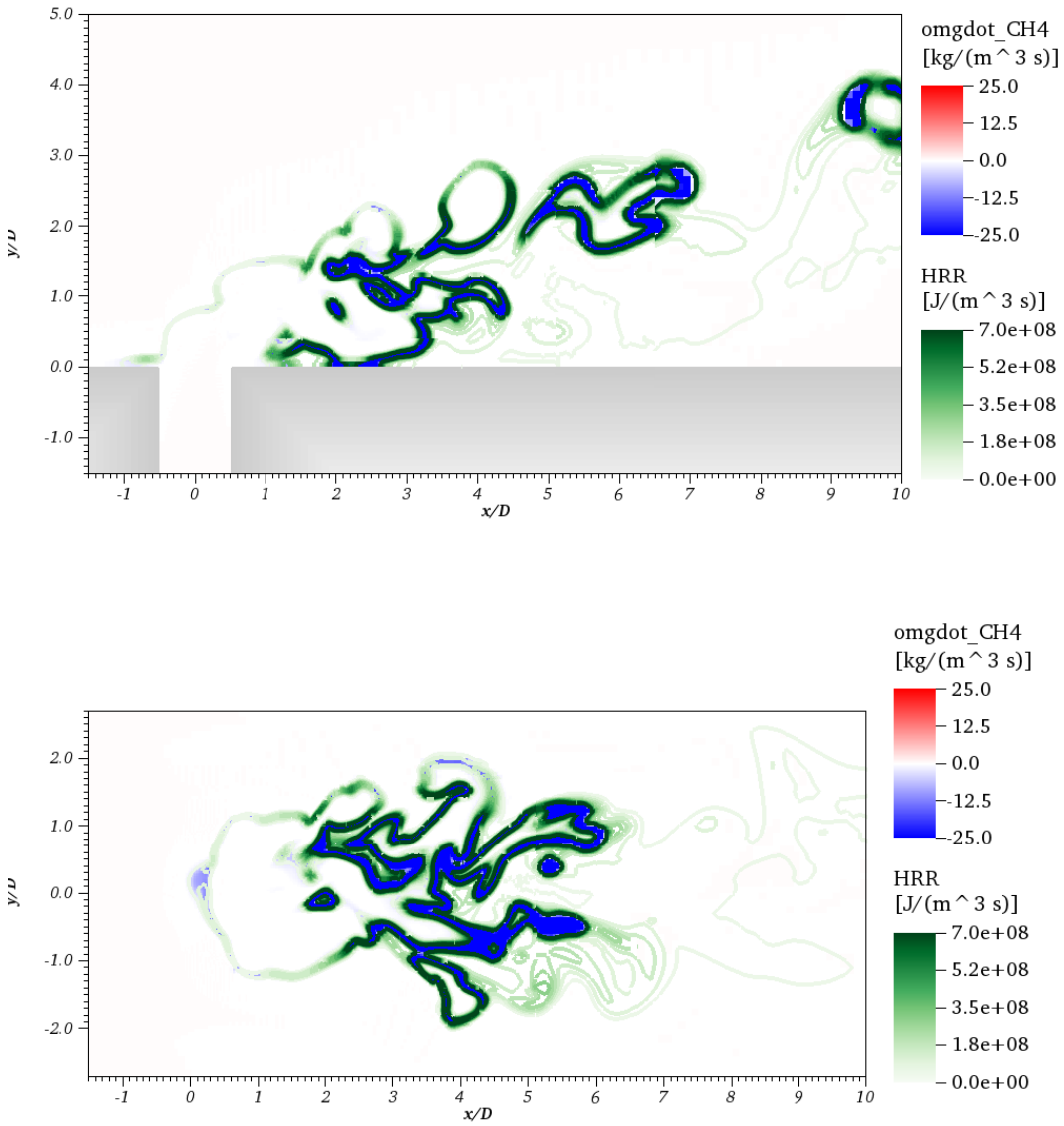

Figure 78 – Jet center-plane (top) and y/D = 0.8 x-z plane (bottom) showing CH_4 reaction rate with overlay of heat release rate for simulation of a reacting jet in crossflow with ϕ_{jet} = 2.2 and J=1.5 and isothermal wall boundary condition.

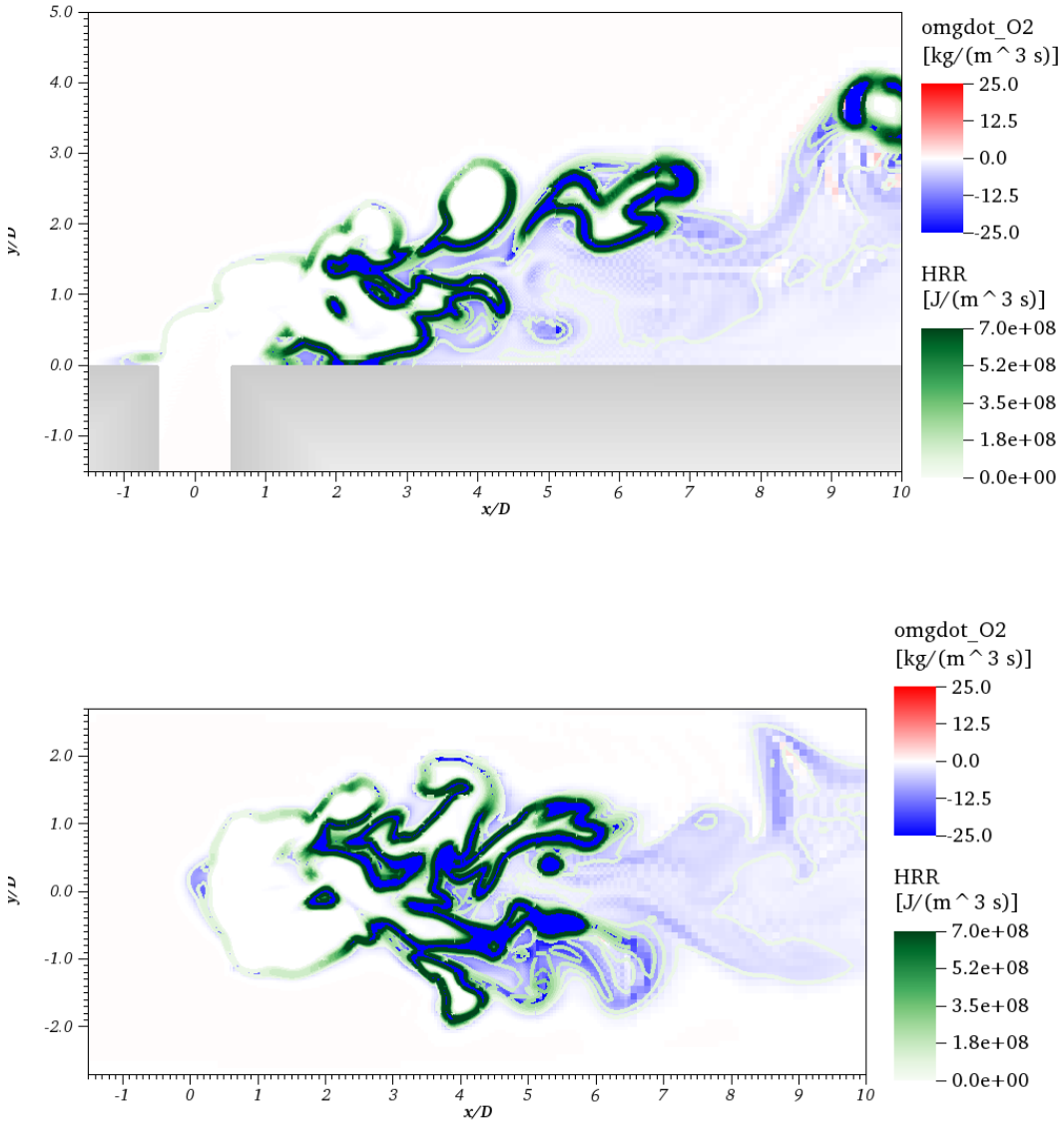

Figure 79 – Jet center-plane (top) and y/D = 0.8 x-z plane (bottom) showing O_2 reaction rate with overlay of heat release rate for simulation of a reacting jet in crossflow with ϕ_{jet} = 2.2 and J=1.5 and isothermal wall boundary condition.

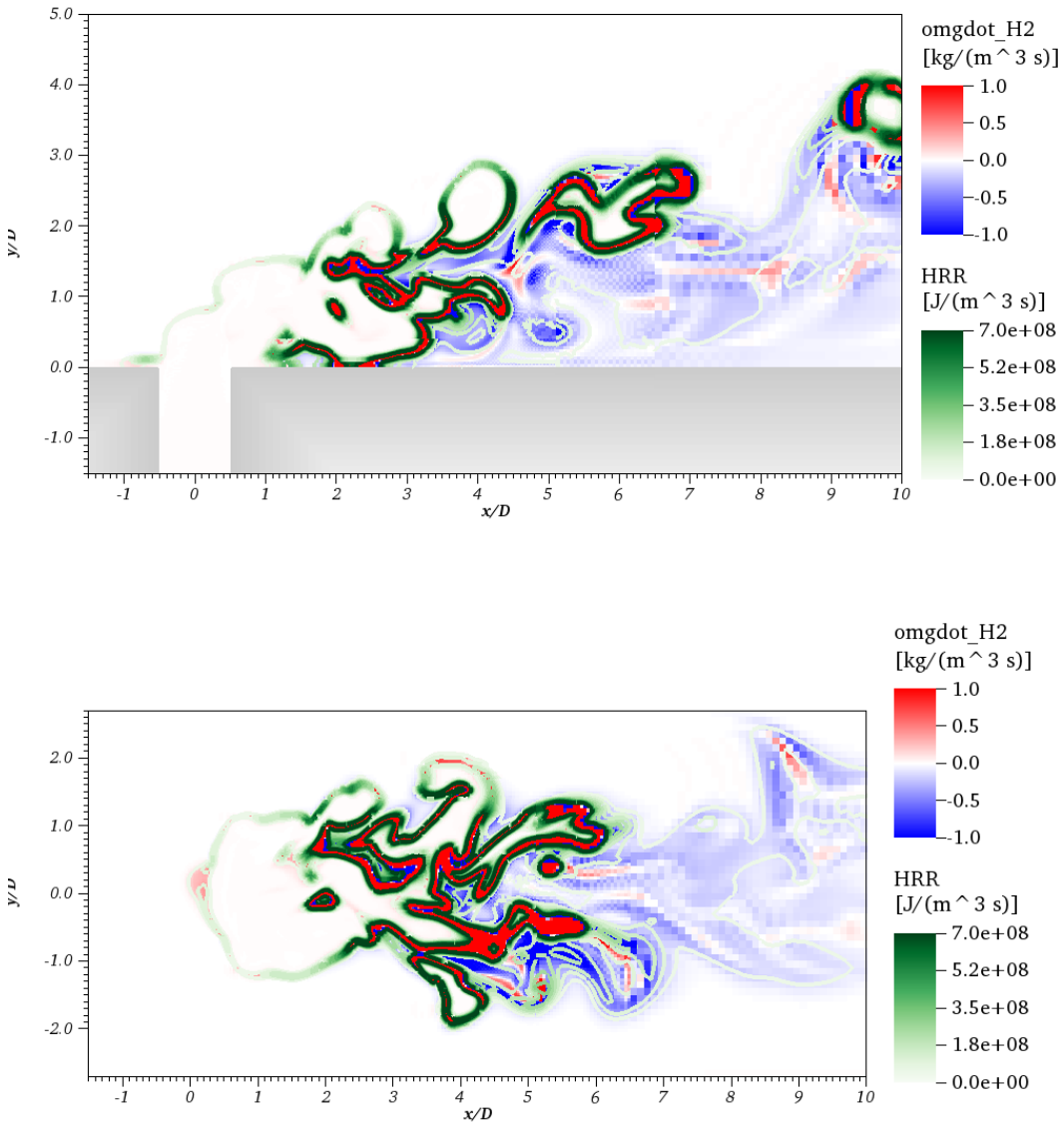

Figure 80 – Jet center-plane (top) and y/D = 0.8 x-z plane (bottom) showing H_2 reaction rate with overlay of heat release rate for simulation of a reacting jet in crossflow with ϕ_{jet} = 2.2 and J=1.5 and isothermal wall boundary condition.

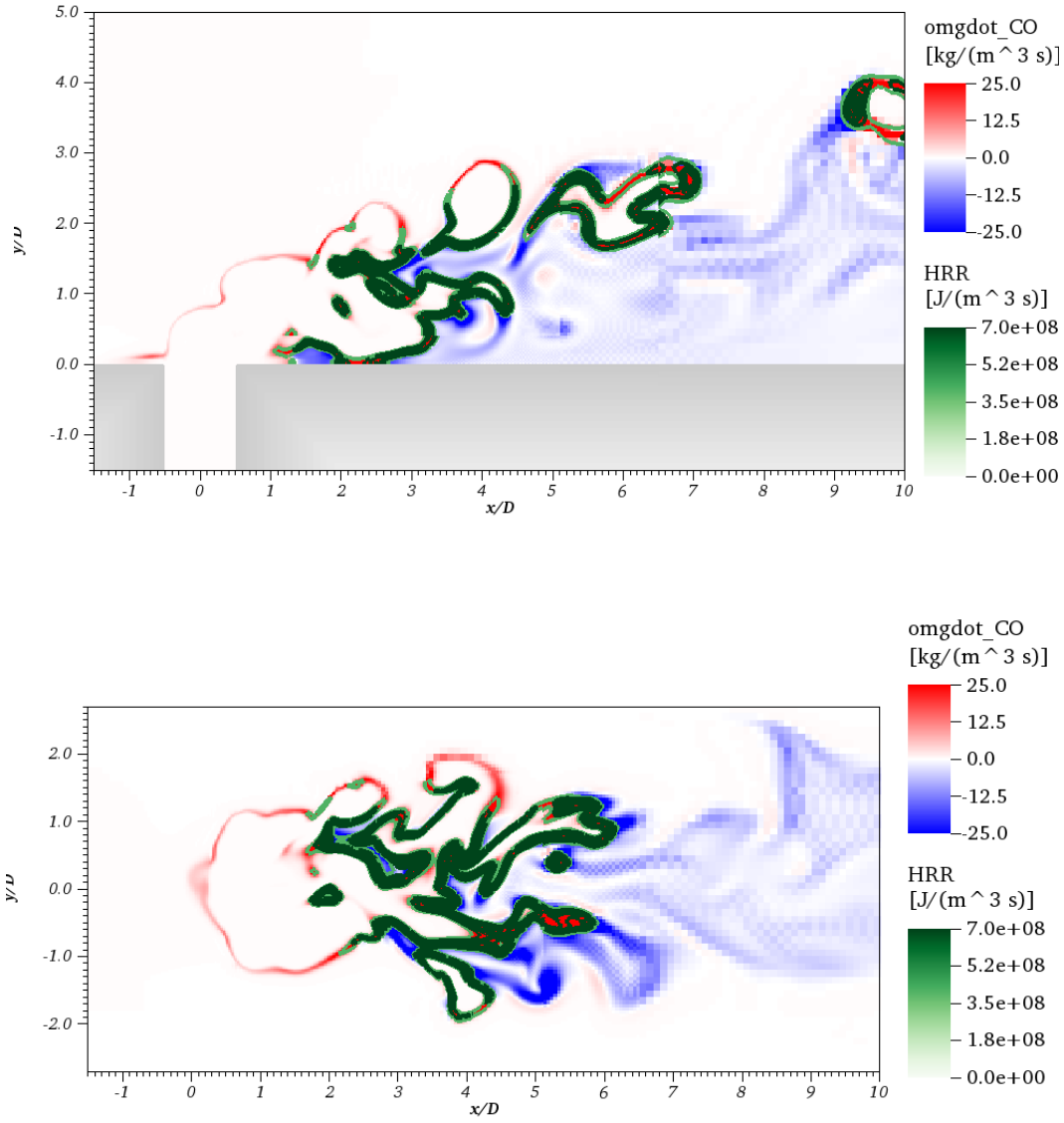

Figure 81 – Jet center-plane (top) and y/D = 0.8 x-z plane (bottom) showing CO reaction rate with overlay of heat release rate for simulation of a reacting jet in crossflow with ϕ_{jet} = 2.2 and J=1.5 and isothermal wall boundary condition.

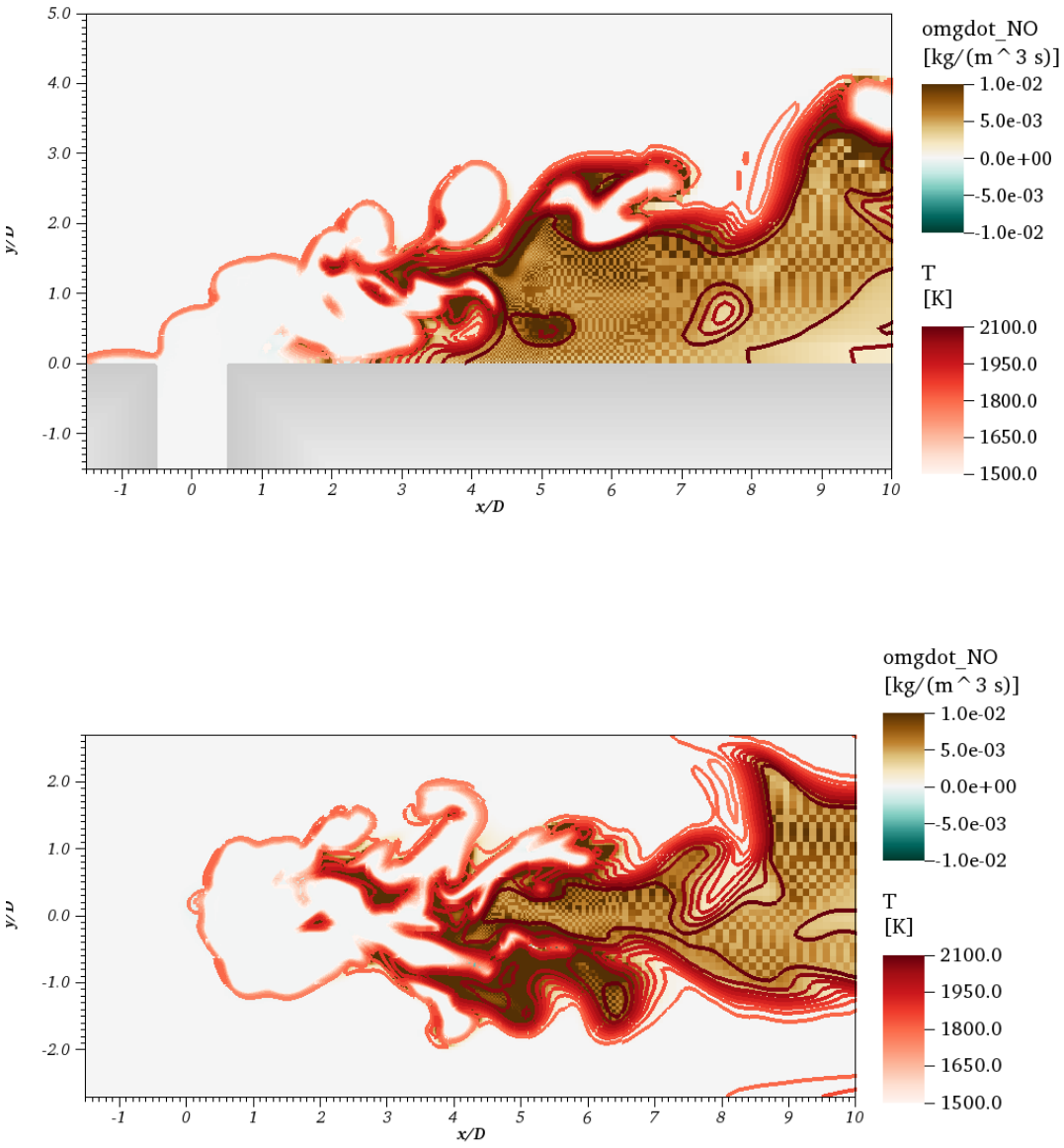

Figure 82 – Jet center-plane (top) and y/D = 0.8 x-z plane (bottom) showing NO reaction rate with overlay of temperature for simulation of a reacting jet in crossflow with ϕ_{jet} = 2.2 and J=1.5 and isothermal wall boundary condition.

REFERENCES

[1] https://www.eia.gov. *Electricity Explained: Electricity in the United States*.

[2] T. Lieuwen, M. Chang, and A. Amato, "Stationary gas turbine combustion: Technology needs and policy considerations," *Combustion and Flame,* vol. 160, no. 8, pp. 1311-1314, 2013.

[3] M. Klein, "Overview of Worldwide Ground-Based Regulatory Framework," in *Gas Turbine Emissions*, T. C. Lieuwen and V. Yang, Eds. (Cambridge Aerospace Series, Cambridge: Cambridge University Press, 2013, pp. 95-120.

[4] A. M. Dean and J. W. Bozelli, "Combustion Chemistry of Nitrogen," in *Gas-Phase Combustion Chemistry*, W. C. Gardiner, Ed. New York: Springer-Verlag, 2000, pp. 125-341.

[5] P. Gokulakrishnan and M. S. Klassen, "NOx and CO Formation and Control," in *Gas Turbine Emissions*, T. C. Lieuwen and V. Yang, Eds. Cambridge: Cambridge University Press, 2013, pp. 175 - 208.

[6] C. T. Bowman, "Control of combustion-generated nitrogen oxide emissions: technology driven by regulation," *Symposium (International) on Combustion,* vol. 24, no. 1, pp. 859-878, 1992.

[7] R. K. Hanson and S. Salimian, "Survey of Rate Constants in the N/H/O System," in *Combustion Chemistry*, W. C. Gardiner, Ed. New York, NY: Springer New York, 1984, pp. 361-421.

[8] R. M. Kelso, T. T. Lim, and A. E. Perry, "An experimental study of round jets in cross-flow," *Journal of Fluid Mechanics,* vol. 306, pp. 111-144, 1996.

[9] S. M. Martin, W. R. Laster, and J. E. P. Bilbao, "Axial stage combustion system with exhaust gas recirculation," 2017.

[10] P. J. Stuttaford, P. Economo, S. Jorgensen, D. Gauthier, and T. Hui, "Axially staged gas turbine combustor with interstage premixer," 2017.

[11] A. Amato, J. Seitzman, and T. Lieuwen, "Emissions from oxyfueled or high-exhaust gas recirculation turbines," in *Gas Turbine Emissions*, T. C. Lieuwen and V. Yang, Eds. Cambridge: Cambridge University Press, 2013, pp. 209-234.

[12] D. Ahrens, M. Kolb, C. Hirsch, and T. Sattelmayer, "NOx Formation in a Reacting Premixed Jet in Hot Cross Flow," in *Turbo Expo*, Düsseldorf, Germany, 2014, no. 45691, p. 26139, Volume 4B: Combustion, Fuels and Emissions: ASME.

[13] E. Goh, M. Sirignano, V. Nair, B. Emerson, T. Lieuwen, and J. Seitzman, "Modeling of Minimum NOx in Staged-Combustion Architectures at Elevated Temperatures," in *Turbo Expo*, Charlotte, NC, USA, 2017, no. 50848, p. 63787, Volume 4A: Combustion, Fuels and Emissions: ASME.

[14] R. G. McKinney and J. B. Hoke, "Aero Gas Turbine Combustion: Metrics, Constraints, and Systems Interactions," in *Gas Turbine Emissions*, T. C. Lieuwen and V. Yang, Eds. (Cambridge Aerospace Series, Cambridge: Cambridge University Press, 2013, pp. 3-23.

[15] A. R. Karagozian, "Transverse jets and their control," *Progress in Energy and Combustion Science,* vol. 36, no. 5, pp. 531-553, 2010.

[16] T. F. Fric and A. Roshko, "Vortical structure in the wake of a transverse jet," *Journal of Fluid Mechanics,* vol. 279, pp. 1-47, 1994.

[17] T. H. New, T. T. Lim, and S. C. Luo, "Elliptic jets in cross-flow," *Journal of Fluid Mechanics,* vol. 494, pp. 119-140, 2003.

[18] S. H. Smith and M. G. Mungal, "Mixing, structure and scaling of the jet in crossflow," *Journal of Fluid Mechanics,* vol. 357, pp. 83-122, 1998.

[19] L. Gevorkyan, T. Shoji, D. R. Getsinger, O. I. Smith, and A. R. Karagozian, "Transverse jet mixing characteristics," *Journal of Fluid Mechanics,* vol. 790, pp. 237-274, 2016.

[20] L. K. Su and M. G. Mungal, "Simultaneous measurements of scalar and velocity field evolution in turbulent crossflowing jets," *Journal of Fluid Mechanics,* vol. 513, pp. 1-45, 2004.

[21] T. H. New, T. T. Lim, and S. C. Luo, "Effects of jet velocity profiles on a round jet in cross-flow," *Experiments in Fluids,* journal article vol. 40, no. 6, pp. 859-875, June 01 2006.

[22] A. M. Steinberg, R. Sadanandan, C. Dem, P. Kutne, and W. Meier, "Structure and stabilization of hydrogen jet flames in cross-flows," presented at the Proceedings of the Combustion Institute, 2013.

[23] J. A. Wagner, S. W. Grib, J. W. Dayton, M. W. Renfro, and B. M. Cetegen, "Flame stabilization analysis of a premixed reacting jet in vitiated crossflow," *Proceedings of the Combustion Institute,* vol. 36, no. 3, pp. 3763-3771, 2017/01/01/ 2017.

[24] J. A. Wagner, S. W. Grib, M. W. Renfro, and B. M. Cetegen, "Flowfield measurements and flame stabilization of a premixed reacting jet in vitiated crossflow," *Combustion and Flame,* vol. 162, no. 10, pp. 3711-3727, 2015.

[25] J. A. Wagner, M. W. Renfro, and B. M. Cetegen, "Premixed jet flame behavior in a hot vitiated crossflow of lean combustion products," *Combustion and Flame,* vol. 176, pp. 521-533, 2017.

[26] D. Schmitt, M. Kolb, J. Weinzierl, C. Hirsch, and T. Sattelmayer, "Ignition and Flame Stabilization of a Premixed Jet in Hot Cross Flow," in *Turbo Expo*, San Antonio, Texas, USA, 2013, no. 55102, p. 94763, Volume 1A: Combustion, Fuels and Emissions: ASME.

[27] E. F. Hasselbrink and M. G. Mungal, "Transverse jets and jet flames. Part 2. Velocity and OH field imaging," *Journal of Fluid Mechanics,* vol. 443, pp. 27-68, 2001.

[28] D. Han and M. G. Mungal, "Simultaneous measurements of velocity and CH distribution. Part II: deflected jet flames," *Combustion and Flame,* vol. 133, no. 1, pp. 1-17, 2003/04/01/ 2003.

[29] O. Schulz and N. Noiray, "Large Eddy Simulation of a Premixed Flame in Hot Vitiated Crossflow With Analytically Reduced Chemistry," *Journal of Engineering for Gas Turbines and Power,* vol. 141, no. 3, pp. 1-7, 2018.

[30] R. Sullivan, B. Wilde, D. R. Noble, J. M. Seitzman, and T. C. Lieuwen, "Time-averaged characteristics of a reacting fuel jet in vitiated cross-flow," *Combustion and Flame,* vol. 161, no. 7, pp. 1792-1803, 2014.

[31] T. Gautam, "Lift-off Heights and Visible Lengths of Vertical Turbulent Jet Diffusion Flames in Still Air," *Combustion Science and Technology,* vol. 41, no. 1-2, pp. 17-29, 1984/09/20 1984.

[32] M. Kolb, D. Ahrens, C. Hirsch, and T. Sattelmayer, "A Model for Predicting the Lift-Off Height of Premixed Jets in Vitiated Cross Flow," *Journal of Engineering for Gas Turbines and Power,* vol. 138, no. 8, pp. 1-9, 2016.

[33] V. Nair, B. Wilde, B. Emerson, and T. Lieuwen, "Shear Layer Dynamics in a Reacting Jet in Crossflow," *Proceedings of the Combustion Institute,* vol. 37, no. 4, pp. 5173-5180, 2019/01/01/ 2019.

[34] V. Nair *et al.*, "Counter rotating vortex pair structure in a reacting jet in crossflow," *Proceedings of the Combustion Institute,* vol. 37, no. 2, pp. 1489-1496, 2019/01/01/ 2019.

[35] R. V. Bandaru and S. R. Turns, "Turbulent jet flames in a crossflow: effects of some jet, crossflow, and pilot-flame parameters on emissions," *Combustion and Flame,* vol. 121, no. 1, pp. 137-151, 2000/04/01/ 2000.

[36] K. H. Lyle, L. K. Tseng, J. P. Gore, and N. M. Laurendeau, "A study of pollutant emission characteristics of partially premixed turbulent jet flames," *Combustion and Flame,* vol. 116, no. 4, pp. 627-639, 1999/03/01/ 1999.

[37] C. Prathap *et al.*, "Analysis of NOX Formation in an Axially Staged Combustion System at Elevated Pressure Conditions," *Journal of Engineering for Gas Turbines and Power,* vol. 134, no. 3, pp. 1-8, 2012.

[38] M. Roa, W. G. Lamont, S. E. Meyer, P. Szedlacsek, and R. P. Lucht, "Emission Measurements and OH-PLIF of Reacting Hydrogen Jets in Vitiated Crossflow for Stationary Gas Turbines," in *Turbo Expo*, Copenhagen, Denmark, 2012, no. 44687, p. 68711, Volume 2: Combustion, Fuels and Emissions, Parts A and B: ASME.

[39] D. Ahrens, M. Kolb, C. Hirsch, and T. Sattelmayer, "Influence of Preflame and Postflame Mixing on NOx Formation in a Reacting Premixed Jet in Hot Cross Flow," *Journal of Engineering for Gas Turbines and Power,* vol. 138, no. 8, pp. 1-10, 2016.

[40] S. Yousefian, G. Bourque, and R. F. Monaghan, "Review of hybrid emissions prediction tools and uncertainty quantification methods for gas turbine combustion systems," in *ASME Turbo Expo 2017: Turbomachinery Technical Conference and Exposition*, 2017: American Society of Mechanical Engineers Digital Collection.

[41] A. Andreini and B. Facchini, "Gas turbines design and off-design performance analysis with emissions evaluation," *Journal of engineering for gas turbines and power,* vol. 126, no. 1, pp. 83-91, 2004.

[42] M. Charest, J. Gauthier, and X. Huang, "Design of a lean premixed prevaporized can combustor," in *ASME Turbo Expo 2006: Power for Land, Sea, and Air*, 2006, pp. 781-791: American Society of Mechanical Engineers Digital Collection.

[43] A. D. Siegel, "A computational approach for preliminary combustor design and gaseous emissions evaluations using a method for sparse kinetics," Georgia Institute of Technology, 2016.

[44] R. Denney, J. Tai, and D. Mavris, "Emissions prediction for aircraft conceptual design," in *48th AIAA/ASME/SAE/ASEE Joint Propulsion Conference & Exhibit*, 2012, p. 4273.

[45] H. Karim *et al.*, "Staged Combustion System for Improved Emissions Operability and Flexibility for 7HA Class Heavy Duty Gas Turbine Engine," no. 50848, p. V04AT04A062, 2017.

[46] R. J. Kee, J. F. Grcar, M. D. Smooke, J. A. Miller, and E. Meeks, "PREMIX: a Fortran program for modeling steady laminar one-dimensional premixed flames," *Sandia National Laboratories Report,* no. SAND85-8249, 1985.

[47] T. Sattelmayer, A. Eroglu, M. Koenig, W. Krebs, and G. Myers, "Industrial Combustors," in *Gas Turbine Emissions*, T. C. Lieuwen and V. Yang, Eds. Cambridge: Cambridge University Press, 2013.

[48] A. S. AlAdawy, J. G. Lee, and B. Abdelnabi, "Effect of turbulence on NOx emission in a lean perfectly-premixed combustor," *Fuel,* vol. 208, pp. 160-167, 2017.

[49] T. Sattelmayer, W. Polifke, D. Winkler, and K. Döbbeling, "NOx-abatement potential of lean-premixed GT-combustors," in *ASME 1996 Turbo Asia conference*, 1996, pp. V001T02A003-V001T02A003: American Society of Mechanical Engineers.

[50] G. P. Smith *et al.*, "GRI-Mech 3.0, 1999," *URL http://www. me. berkeley. edu/gri_mech,* 2011.

[51] J. Santner, S. F. Ahmed, T. Farouk, and F. L. Dryer, "Computational Study of NO x Formation at Conditions Relevant to Gas Turbine Operation: Part 1," *Energy & Fuels,* vol. 30, no. 8, pp. 6745-6755, 2016.

[52] A. A. Konnov, "Implementation of the NCN pathway of prompt-NO formation in the detailed reaction mechanism," *Combustion and Flame,* vol. 156, no. 11, pp. 2093-2105, 2009.

[53] *Chemical-Kinetic Mechanisms for Combustion Applications*. Available: http://combustion.ucsd.edu

[54] B. R. Wilde, "Dynamics of Variable Density Ratio Reacting Jets in Unsteady, Vitiated Crossflow," School of Aerospace Engineering, Georgia Institute of Technology, 2014.

[55] Y. A. C. Cengel, John M., *Fluid Mechanics Fundamentals and Applications*. New York: McGrawHill, 2006.

[56] R. T. M'Closkey, J. M. King, L. Cortelezzi, and A. R. Karagozian, "The actively controlled jet in crossflow," *Journal of Fluid Mechanics,* vol. 452, pp. 325-335, 2002.

[57] S. Megerian, J. Davitian, L. S. De B. Alves, and A. R. Karagozian, "Transverse-jet shear-layer instabilities. Part 1. Experimental studies," *Journal of Fluid Mechanics,* vol. 593, pp. 93-129, 2007.

[58] S. R. Shapiro, J. King, R. T. M'Closkey, and A. R. Karagozian, "Optimization of Controlled Jets in Crossflow," *AIAA Journal,* vol. 44, no. 6, pp. 1292-1298, 2006/06/01 2006.

[59] J. Davitian, "Exploration and Controlled Excitation of Transverse Jet Shear Layer Instabilities," Aerospace Engineering, University of California, Los Angeles, 2008.

[60] K. He, J. Sun, and X. Tang, "Guided image filtering," *IEEE transactions on pattern analysis and machine intelligence,* vol. 35, no. 6, pp. 1397-1409, 2013.

[61] N. Otsu, "A threshold selection method from gray-level histograms," *IEEE transactions on systems, man, and cybernetics,* vol. 9, no. 1, pp. 62-66, 1979.

[62] M. Pernpeintner, M. Lauer, C. Hirsch, and T. Sattelmayer, "A Method to Obtain Planar Mixture Fraction Statistics in Turbulent Flows Seeded With Tracer Particles," no. 54624, pp. 1341-1350, 2011.

[63] J. C. Sautet and D. Stepowski, "Single-shot laser Mie scattering measurements of the scalar profiles in the near field of turbulent jets with variable densities," *Experiments in Fluids,* journal article vol. 16, no. 6, pp. 353-367, May 01 1994.

[64] M. Raffel, C. Willert, S. Wereley, and J. Kompenhans, *Particle Image Velicometry: A Practical Guide*. New York: Springer, 2007.

[65] B. J. McKeon *et al.*, "Velocity, Vorticity, and Mach Number: Particle Based Techniques," in *Handbook of Experimental Fluid Mechanics*, C. Tropea, A. Yarin, and J. F. Foss, Eds. Berlin: Springer, 2007.

[66] B. Muralidharan and S. Menon, "Large Eddy Simulation of Turbulent Reacting Jet in Cross Flow with Adaptive Mesh Refinement," in *52nd Aerospace Sciences Meeting*, 2014, p. 0825.

[67] W. W. Kim and S. Menon, "An unsteady incompressible Navier–Stokes solver for large eddy simulation of turbulent flows," *International Journal for Numerical Methods in Fluids,* vol. 31, no. 6, pp. 983-1017, 1999.

[68] C. Sung, C. K. Law, and J.-Y. Chen, "Augmented reduced mechanisms for NO emission in methane oxidation," *Combustion and Flame,* vol. 125, no. 1-2, pp. 906-919, 2001.